

(NASA-RP-1218) AIRFOIL SELF-NOISE AND
PREDICTION (NASA. Langley Research Center)
145 P CSCL 20A

889-25673

Unclass

81/71 0127747

NASA
Reference
Publication
1218

1989

Airfoil Self-Noise and Prediction

Thomas F. Brooks
Langley Research Center
Hampton, Virginia

D. Stuart Pope
PRC Kentron, Inc.
Aerospace Technologies Division
Hampton, Virginia

Michael A. Marcolini
Langley Research Center
Hampton, Virginia



National Aeronautics and
Space Administration
Office of Management
Scientific and Technical
Information Division

Contents

Summary	1
1. Introduction	2
1.1. Noise Sources and Background	2
1.1.1. Turbulent-Boundary-Layer-Trailing-Edge (TBL-TE) Noise	2
1.1.2. Separation-Stall Noise	3
1.1.3. Laminar-Boundary-Layer-Vortex-Shedding (LBL-VS) Noise	3
1.1.4. Tip Vortex Formation Noise	4
1.1.5. Trailing-Edge-Bluntness-Vortex-Shedding Noise	4
1.2. Overview of Report	4
2. Description of Experiments	5
2.1. Models and Facility	5
2.2. Instrumentation	5
2.3. Test Conditions	5
2.4. Wind Tunnel Corrections	5
3. Boundary-Layer Parameters at the Trailing Edge	9
3.1. Scaled Data	9
3.2. Calculation Procedures	9
4. Acoustic Measurements	15
4.1. Source Identification	15
4.2. Correlation Editing and Spectral Determination	15
4.3. Self-Noise Spectra	17
5. Spectral Scaling	51
5.1. Turbulent-Boundary-Layer-Trailing-Edge Noise and Separated Flow Noise	51
5.1.1. Scaled Data	51
Zero angle of attack	51
Nonzero angle of attack	54
5.1.2. Calculation Procedures	59
5.1.3. Comparison With Data	62
5.2. Laminar-Boundary-Layer-Vortex-Shedding Noise	62
5.2.1. Scaled Data	63
5.2.2. Calculation Procedures	66
5.2.3. Comparison With Data	71
5.3. Tip Vortex Formation Noise	71
5.3.1. Calculation Procedures	71
5.3.2. Comparison With Data	73
5.4. Trailing-Edge-Bluntness-Vortex-Shedding Noise	73
5.4.1. Experiment	73

5.4.2. Scaled Data	74
5.4.3. Calculation Procedures	78
5.4.4. Comparison With Data	81
6. Comparison of Predictions With Published Results	83
6.1. Study of Schlinker and Amiet	83
6.1.1. Boundary-Layer Definition	83
6.1.2. Trailing-Edge Noise Measurements and Predictions	83
6.2. Study of Schlinker	88
6.3. Study of Fink, Schlinker, and Amiet	88
7. Conclusions	99
Appendix A—Data Processing and Spectral Determination	100
Appendix B—Noise Directivity	105
Appendix C—Application of Predictions to a Rotor Broadband Noise Test	108
Appendix D—Prediction Code	112
References	133
Tables	134

Symbols			
A	spectral shape function for TBL-TE noise, eqs. (35) and (36)	\mathcal{L}	turbulence correlation scale, m
a, a_0	parameters of shape function A , eqs. (37) and (38)	l	spanwise extent of tip vortex at TE, m
B	spectral shape function for separation noise, eqs. (41) and (42)	M	Mach number, U/c_0
b, b_0	parameters of shape function B , eqs. (43) and (44)	M_{\max}	maximum Mach number in tip vortex formation region
c	chord length, m	R_c	Reynolds number based on chord length, cU/ν
c_0	medium speed of sound, m/s	$R_{ij}(\tau)$	cross-correlation between microphones M_i and M_j , Pa^2
\bar{D}_h	directivity function for TE noise (high-frequency limit), eq. (B1)	r	distance from source to observer, m
\bar{D}_l	directivity function for translating dipole (low-frequency limit), eq. (B2)	$S(f)$	spectrum of self-noise, Pa^2/Hz
$F(\text{St})$	universal spectral shape function, eq. (18)	$\text{St}, \text{St}_1, \bar{\text{St}}_1, \text{St}_2$	Strouhal numbers defined for TBL-TE and separation noise scaling, section 5.1.
f	frequency, Hz	St', St'_1	Strouhal numbers defined for LBL-VS noise scaling, section 5.2.
G_1	spectral shape function for LBL-VS noise, eq. (57)	St''	Strouhal number defined for tip vortex formation noise, section 5.3.
G_2	R_c -dependence for LBL-VS noise peak amplitude, eq. (58)	St'''	Strouhal number defined for TE-bluntness-vortex-shedding noise, section 5.4.
G_3	angle dependence for G_2 function, eq. (60)	t	time, s
G_4	peak level function for G_5 , eq. (74)	U	free-stream velocity, m/s
G_5	spectral shape function for TE bluntness noise, eqs. (75)–(82)	U_c	convection velocity, m/s
$G_{ij}(f)$	cross-spectrum between microphone M_i and M_j , Pa^2/Hz	x	streamwise axis, see fig. B3, m
H	tunnel height, m	y	lateral axis, m
h	TE thickness (degree of bluntness), m	z	vertical axis, m
$K, K_1, \Delta K_1, K_2$	constants, defined by eqs. (18), (47), (48), and (49)	α_{TIP}	angle of attack of airfoil tip to oncoming flow, deg
L	span, m	α'_{TIP}	corrected angle of attack of airfoil tip, eq. (66), deg
L'	sectional lift of blade, lift per unit span	α_t	airfoil angle of attack referenced to tunnel streamwise axis, deg
		α_e	effective aerodynamic angle of attack, corrected for open wind tunnel effects, deg
		δ	boundary-layer thickness, m
		δ^*	boundary-layer displacement thickness, m

Γ	tip vortex strength, m^2/s
Θ	angle from source streamwise axis x to observer, see fig. B3, deg
θ	boundary-layer momentum thickness, m
ν	kinematic viscosity of medium, m^2/s
τ	time delay, s
Φ	angle from source lateral axis y to observer, see fig. B3, deg
ϕ	cross-spectral phase angle, deg
Ψ	angle parameter related to surface slope at TE, section 5.4, deg

Subscripts:

avg	average
e	retarded coordinate
p	pressure side of airfoil
s	suction side of airfoil
TIP	tip of blade
TOT	total
α	angle dependent

0	for δ_0 , δ_0^* , and θ_0 is for airfoil at zero angle of attack, reference value
1/3	1/3-octave spectral presentation

Abbreviations:

BL	boundary layer
LBL	laminar boundary layer
LE	leading edge of airfoil blade
LHS	left-hand side
Mi	microphone number i for $i = 1$ through 9, see fig. 4
OASPL	overall sound pressure level, dB
RHS	right-hand side
SPL	sound pressure level, spectrum, dB (re 2×10^{-5} Pa)
TBL	turbulent boundary layer
TE	trailing edge of airfoil blade
UTRC	United Technologies Research Center
VS	vortex shedding
2D	two-dimensional
3D	three-dimensional

Summary

An overall prediction method has been developed for the self-generated noise of an airfoil blade encountering smooth flow. Prediction methods for individual self-noise mechanisms are semiempirical and are based on previous theoretical studies and the most comprehensive self-noise data set available. The specially processed data set, most of which is newly presented in this report, is from a series of aerodynamic and acoustic tests of two- and three-dimensional airfoil blade sections conducted in an anechoic wind tunnel. Five self-noise mechanisms due to specific boundary-layer phenomena have been identified and modeled: boundary-layer turbulence passing the trailing edge, separated-boundary-layer and stalled-airfoil flow, vortex shedding due to laminar-boundary-layer instabilities, vortex shedding from blunt trailing edges, and the turbulent vortex flow existing near the tips of lifting blades. The data base, with which the predictions are matched, is from seven NACA 0012 airfoil blade sections of different sizes (chord lengths from 2.5 to 61 cm) tested at wind tunnel speeds up to Mach 0.21 (Reynolds number based on chord up to 3×10^6) and at angles of attack from 0° to 25.2° . The predictions are compared successfully with published data from three self-noise studies of different airfoil shapes, which were tested up to Mach and Reynolds numbers of 0.5 and 4.6×10^6 , respectively. An application of the prediction method is reported for a large-scale-model helicopter rotor and the predictions compared well with data from a broadband noise test of the rotor, conducted in a large anechoic wind tunnel. A computer code of the methods is given for the predictions of 1/3-octave formatted spectra.

1. Introduction

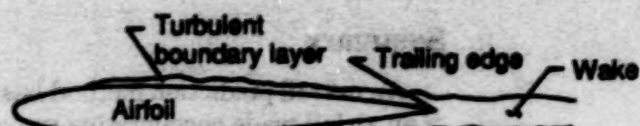
Airfoil self-noise is due to the interaction between an airfoil blade and the turbulence produced in its own boundary layer and near wake. It is the total noise produced when an airfoil encounters smooth nonturbulent inflow. Over the last decade, research has been conducted at and supported by NASA Langley Research Center to develop fundamental understanding, as well as prediction capability, of the various self-noise mechanisms. The interest has been motivated by its importance to broadband helicopter rotor, wind turbine, and airframe noises. The present paper is the cumulative result of a series of aerodynamic and acoustic wind tunnel tests of airfoil sections, which has produced a comprehensive data base. A correspondingly extensive semi-empirical scaling effort has produced predictive capability for five self-noise mechanisms.

1.1. Noise Sources and Background

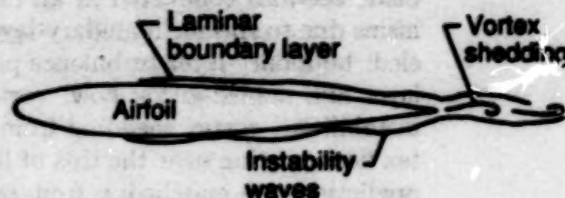
Previous research efforts (prior to 1983) for the broadband noise mechanisms are reviewed in some detail by Brooks and Schlinker (ref. 1). In figure 1, the subsonic flow conditions for five self-noise mechanisms of concern here are illustrated. At high Reynolds number R_c (based on chord length), turbulent boundary layers (TBL) develop over most of the airfoil. Noise is produced as this turbulence passes over the trailing edge (TE). At low R_c , largely laminar boundary layers (LBL) develop, whose instabilities result in vortex shedding (VS) and associated noise from the TE. For nonzero angles of attack, the flow can separate near the TE on the suction side of the airfoil to produce TE noise due to the shed turbulent vorticity. At very high angles of attack, the separated flow near the TE gives way to large-scale separation (deep stall) causing the airfoil to radiate low-frequency noise similar to that of a bluff body in flow. Another noise source is vortex shedding occurring in the small separated flow region aft of a blunt TE. The remaining source considered here is due to the formation of the tip vortex, containing highly turbulent flow, occurring near the tips of lifting blades or wings.

1.1.1. Turbulent-Boundary-Layer-Trailing-Edge (TBL-TE) Noise

Using measured surface pressures, Brooks and Hodgson (ref. 2) demonstrated that if sufficient information is known about the TBL convecting surface pressure field passing the TE, then TBL-TE noise can be accurately predicted. Schlinker and Amiet (ref. 3) employed a generalized empirical description of surface pressure to predict measured noise. However, the lack of agreement for many cases indicated



Turbulent-boundary-layer-trailing-edge noise



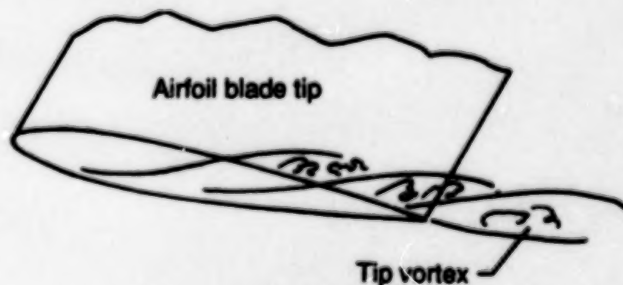
Laminar-boundary-layer-vortex-shedding noise



Separation-stall noise



Trailing-edge-bluntness-vortex-shedding noise



Tip vortex formation noise

Figure 1. Flow conditions producing airfoil blade self-noise.

a need for a more accurate pressure description than was available. Langley supported a research effort (ref. 4) to model the turbulence within boundary layers as a sum of discrete "hairpin" vortex elements. In a parallel and follow-up effort, the present authors matched measured and calculated mean boundary-layer characteristics to prescribed distributions of the discrete vortex elements so that associated surface pressure could be determined. The use of the model to predict TBL-TE noise proved disappointing because of its inability to show correct trends with angle of attack or velocity. The results showed that to successfully describe the surface pressure, the history of the turbulence must be accounted for in addition to the mean TBL characteristics. This level of turbulence modeling has not been attempted to date.

A simpler approach to the TBL-TE noise problem is based on the Ffowcs Williams and Hall (ref. 5) edge-scatter formulation. In reference 3, the noise data were normalized by employing the edge-scatter model with the mean TBL thickness δ used as a required length scale. When δ was unknown, simple flat plate theory was used to estimate δ . Spectral data initially differing by 40 dB collapsed to within 7 dB, consistent with the results of the approach discussed above using surface pressure models. The extent of agreement between data sets was largely due to the correct scaling of the velocity dependence, which is the most sensitive parameter in the scaling approach. The dependence of the overall sound pressure level on velocity to the fifth power had been verified in a number of studies. The extent to which the normalized data deviation was due to uncertainty in δ was addressed by Brooks and Marcolini (ref. 6) in a forerunner to the present report. For large Re and small angles of attack, which matched the conditions of reference 3, the use of measured TBL thicknesses δ , displacement thicknesses δ^* , or momentum thicknesses θ in the normalization produced the same degree of deviation within the TBL-TE noise data. Subsequently, normalizations based on boundary-layer maximum shear stress measurements and, alternately, profile shape factors were also examined. Of particular concern in reference 6 was that when an array of model sizes, rather than just large models, was tested at various angles of attack, the normalized spectrum deviations increased to 10 or even 20 dB. These large deviations indicate a lack of fidelity of the spectrum normalization and any subsequent prediction methods based on curve fits. They also reinforce the conclusion from the aforementioned surface pressure modeling effort that knowledge of the mean TBL characteristics alone is insufficient to define the turbulence structure. The conditions under which the turbulence evolves were

found to be important. The normalized data appeared to be directly influenced by factors such as Reynolds number and angle of attack, which in previous analyses were assumed to be of pertinence only through their effect on TBL thickness δ (refs. 3 and 7).

Several prediction schemes for TBL-TE noise have been used previously for helicopter rotor noise (refs. 3 and 8) and for wind turbines (refs. 9 and 10). These schemes have all evolved from scaling law equations which were fitted to the normalized data of reference 3 and, thus, are limited by the same concerns of generality discussed above.

1.1.2. Separation-Stall Noise

Assessments of the separated flow noise mechanism for airfoils at moderate to high angles of attack have been very limited (ref. 1). The relative importance of airfoil stall noise was illustrated in the data of Fink and Bailey (ref. 11) in an airframe noise study. At stall, noise increased by more than 10 dB relative to TBL-TE noise, emitted at low angles of attack. Paterson et al. (ref. 12) found evidence through surface to far field cross-correlations that for mildly separated flow the dominant noise is emitted from the TE, whereas for deep stall the noise radiated from the chord as a whole. This finding is consistent with the conclusions of reference 11.

No predictive methods are known to have been developed. A successful method would have to account for the gradual introduction of separated flow noise as airfoil angle of attack is increased. Beyond limiting angles, deep stall noise would be the only major contributing source.

1.1.3. Laminar-Boundary-Layer-Vortex-Shedding (LBL-VS) Noise

When a LBL exists over most of at least one side of an airfoil, vortex shedding noise can occur. The vortex shedding is apparently coupled to acoustically excited aerodynamic feedback loops (refs. 13, 14, and 15). In references 14 and 15, the feedback loop is taken between the airfoil TE and an upstream "source" point on the surface, where Tollmien-Schlichting instability waves originate in the LBL. The resulting noise spectrum is composed of quasi-tones related to the shedding rates at the TE. The gross trend of the frequency dependence was found by Paterson et al. (ref. 16) by scaling on a Strouhal number basis with the LBL thickness at the TE being the relevant length scale. Simple flat plate LBL theory was used to determine the boundary-layer thicknesses δ in the frequency comparisons. The use of measured values of δ in reference 6 verified the general Strouhal dependence. Additionally,

for zero angle of attack, Brooks and Marcolini (ref. 6) found that overall levels of LBL-VS noise could be normalized so that the transition from LBL-VS noise to TBL-TE noise is a unique function of R_c .

There have been no LBL-VS noise prediction methods proposed, because most studies have emphasized the examination of the rather erratic frequency dependence of the individual quasi-tones in attempts to explain the basic mechanism. However, the scaling successes described above in references 6 and 16 can offer initial scaling guidance for the development of predictions in spite of the general complexity of the mechanism.

1.1.4. Tip Vortex Formation Noise

The tip noise source has been identified with the turbulence in the local separated flow associated with formation of the tip vortex (ref. 17). The flow over the blade tip consists of a vortex with a thick viscous turbulent core. The mechanism for noise production is taken to be TE noise due to the passage of the turbulence over the TE of the tip region. George and Chou (ref. 8) proposed a prediction model based on spectral data from delta wing studies (assumed to approximate the tip vortex flow of intercat), mean flow studies of several tip shapes, and TE noise analysis.

Brooks and Marcolini (ref. 18) conducted an experimental study to isolate tip noise in a quantitative manner. The data were obtained by comparing sets of two- and three-dimensional test results for different model sizes, angles of attack, and tunnel flow velocities. From data scaling, a quantitative prediction method was proposed which had basic consistency with the method of reference 8.

1.1.5. Trailing-Edge-Bluntness-Vortex-Shedding Noise

Noise due to vortex shedding from blunt trailing edges was established by Brooks and Hodgson (ref. 2) to be an important airfoil self-noise source. Other studies of bluntness effects, as reviewed by Blake (ref. 19) and Brooks and Schlinker (ref. 1), were only aerodynamic in scope and dealt with TE thicknesses that were large compared with the boundary-layer

displacement thicknesses. For rotor blade and wing designs, the bluntness is likely to be small compared with boundary-layer thicknesses.

Grosveld (ref. 9) used the data of reference 2 to obtain a scaling law for TE bluntness noise. He found that the scaling model could explain the spectral behavior of high-frequency broadband noise of wind turbines. Chou and George (ref. 20) followed suit with an alternative scaling of the data of reference 2 to model the noise. For both modeling techniques neither the functional dependence of the noise on boundary-layer thickness (as compared with the TE bluntness) nor the specifics of the blunted TE shape were incorporated. A more general model is needed.

1.2. Overview of Report

The purpose of this report is to document the development of a self-noise prediction method and to verify its accuracy for a range of applications. The tests producing the data base for the scaling effort are described in section 2. In section 3, the measured boundary-layer thickness and integral parameter data, used to normalize airfoil noise data, are documented. The acoustic measurements are reported in section 4, where a special correlation editing procedure is used to extract clean self-noise spectra from data containing extraneous test rig noise. In section 5, the scaling laws are developed for the five self-noise mechanisms. For each, the data are first normalized by fundamental techniques and then examined for dependences on parameters such as Reynolds number, Mach number, and geometry. The resulting prediction methods are delineated with specific calculation procedures and results are compared with the original data base. The predictions are compared in section 6 with self-noise data from three studies reported in the literature. In appendix A, the data processing technique is detailed; in appendix B, the noise directivity functions are defined; and in appendix C, an application of the prediction methods is reported for a helicopter rotor broadband noise study. In appendix D, a computer code of the prediction method is given.

2. Description of Experiments

The details of the measurements and test facility have been reported in reference 6 for the sharp TE two-dimensional (2D) airfoil model tests, in reference 18 for corresponding three-dimensional (3D) tests, and in reference 2 for the blunt TE 2D airfoil model test. Specific information applicable to this report is presented here.

2.1. Models and Facility

The models were tested in the low-turbulence potential core of a free jet located in an anechoic chamber. The jet was provided by a vertically mounted nozzle with a rectangular exit with dimensions of 30.48×45.72 cm. The 2D sharp TE models are shown in figure 2. The models, all of 45.72-cm span, were NACA 0012 airfoils with chord lengths of 2.54, 5.08, 10.16, 15.24, 22.86, and 30.48 cm. The models were made with very sharp TE, less than 0.05 mm thick, without beveling the edge. The slope of the surface near the uncurved TE corresponded to the required 7° off the chord line. The sharp TE 3D models, shown in figure 3, all had spans of 30.48 cm and chord lengths that were the same as the five largest 2D models. The 3D models had rounded tips, defined by rotating the NACA 0012 shape about the chord line at 30.48-cm span. An NACA 0012 model of pertinence to the present paper, which is not shown here, is the blunt-TE airfoil of reference 2, with a chord length of 60.96 cm. Details of the blunt TE of this large model are given in section 5.

The cylindrical hubs, shown attached to the models, provided support and flush-mounting on the side plates of the test rig. At a geometric tunnel angle of attack α_t of 0° , the TE of all models was located 61.0 cm above the nozzle exit. The tunnel angle α_t is referenced to the undisturbed tunnel streamline direction. In figure 4, an acoustic test configuration for a 3D model is shown. A 3D setup is shown so that the model can be seen fitted to the side plate. The side plates ($152.4 \times 30.0 \times 1$ cm) were reinforced and flush mounted on the nozzle lips. For the 2D configurations, an additional side plate was used.

2.2. Instrumentation

For all of the acoustic testing, eight 1.27-cm-diameter (1/2-in.) free-field-response microphones were mounted in the plane perpendicular to the 2D model midspan. One microphone was offset from this midspan plane. In figure 4, seven of these are shown with the identification numbers indicated. Microphones M1 and M2 were perpendicular to the chord line at the TE for $\alpha_t = 0^\circ$. The other microphones shown were at radii of 122 cm from the TE, as with M1 and M2, but were positioned

30° forward (M4 and M7) and 30° aft (M5 and M8). The data acquisition and processing approaches are described in appendix A.

For the aerodynamic tests the microphones to the right in figure 4 were removed and replaced by a large three-axis computer-controlled traverse rig used to position hot-wire probes. The miniature probes included both cross-wire and single-wire configurations. In figure 5, a cross-wire probe is shown mounted on the variable-angle arm of the traverse rig. Again, for clarity, a 3D airfoil model is shown. The probes were used to survey the flow fields about the models, especially in the boundary-layer and near-wake region just downstream of the trailing edge.

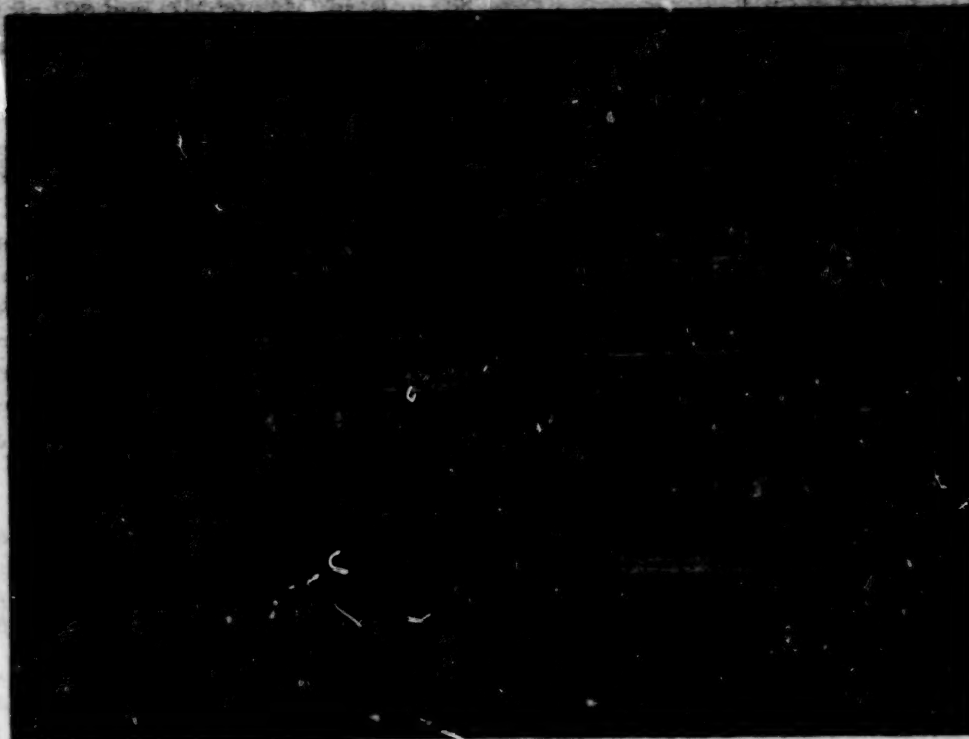
2.3. Test Conditions

The models were tested at free-stream velocities U up to 71.3 m/s, corresponding to Mach numbers up to 0.208 and Reynolds numbers, based on a 30.48-cm-chord model, up to 1.5×10^6 . The tunnel angles of attack α_t were 0° , 5.4° , 10.8° , 14.4° , 19.8° , and 25.2° . The larger angles were not attempted for the larger models to avoid large uncorrectable tunnel flow deflections. For the 22.86-cm- and 30.48-cm-chord models, α_t was limited to 19.8° and 14.4° , respectively.

For the untripped BL cases (natural BL development), the surfaces were smooth and clean. For the tripped BL cases, BL transition was achieved by a random distribution of grit in strips from the leading edge (LE) to 20 percent chord. This tripping is considered heavy because the chordwise extent of the strip produced thicker than normal BL thicknesses. It was used to establish a well-developed TBL even for the smaller models and at the same time retain geometric similarity. The commercial grit number was No. 60 (nominal particle diameter of 0.29 mm) with an application density of about 380 particles/cm². An exception was the 2.54-cm-chord airfoil which had a strip at 30 percent chord of No. 100 grit with a density of about 690 particles/cm².

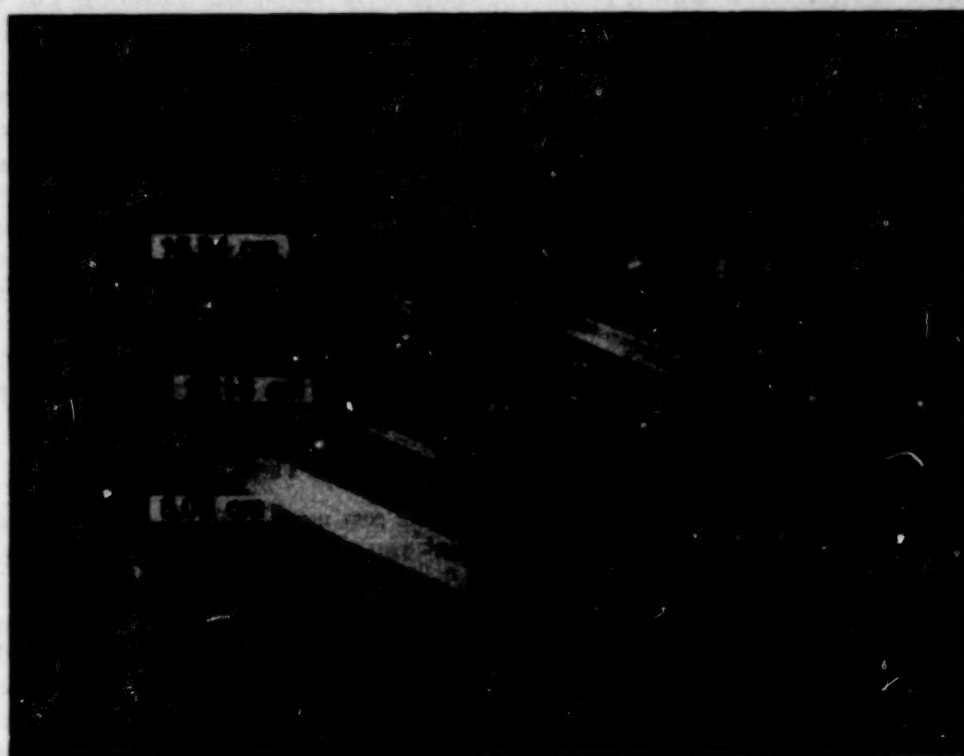
2.4. Wind Tunnel Corrections

The testing of airfoil models in a finite-size open wind tunnel causes flow curvature and downwash deflection of the incident flow that do not occur in free air. This effectively reduces the angle of attack, more so for the larger models. Brooks, Marcolini, and Pope (ref. 21) used lifting surface theory to develop the 2D open wind tunnel corrections to angle of attack and camber. Of interest here is a corrected angle of attack α_∞ representing the angle in free air required to give the same lift as α_t would give in the tunnel. One has from reference 21, upon ignoring



L-82-4573

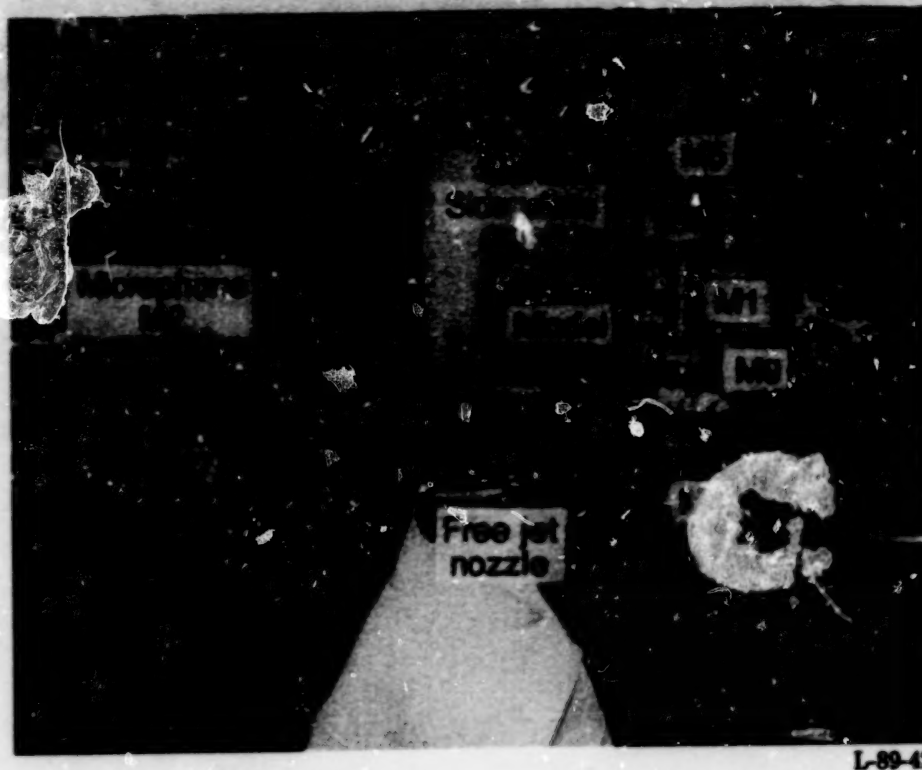
Figure 2. Two-dimensional NACA 0012 airfoil blade models.



L-82-4570

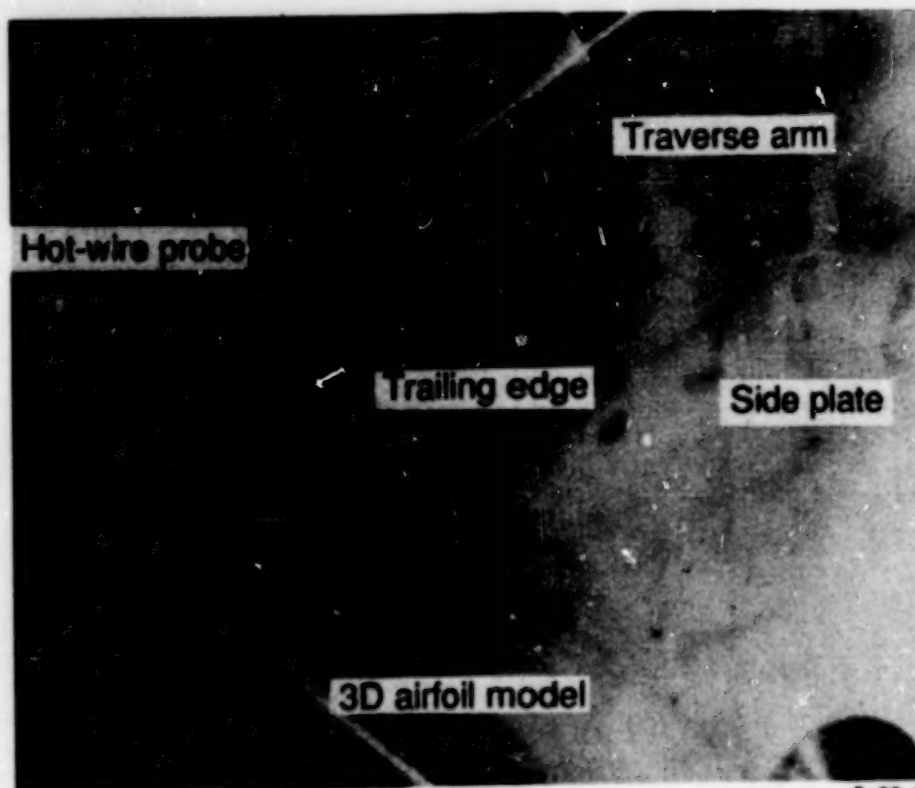
Figure 3. Three-dimensional NACA 0012 airfoil blade models.

ORIGINAL PAGE
BLACK AND WHITE PHOTOGRAPH



L-89-42

Figure 4. Test setup for acoustic tests of a 3D model airfoil.



L-89-43

Figure 5. Tip survey using hot-wire probe.

small camber effects,

$$\alpha_e = \alpha_i / \zeta \quad (1)$$

where

$$\zeta = (1 + 2\sigma)^2 + \sqrt{12\sigma}$$

and

$$\sigma = (\pi^2/48)(c/H)^2$$

The term c is the airfoil chord and H is the tunnel height or vertical open jet dimension for a horizontally aligned airfoil. For the present 2D configurations, α_e/α_i equals 0.88, 0.78, 0.62, 0.50, 0.37, and 0.28 for the models with chord lengths of 2.54, 5.08, 10.16, 15.24, 22.86, and 30.48 cm, respectively.

3. Boundary-Layer Parameters at the Trailing Edge

The purpose of this section is to present measured boundary-layer thicknesses from reference 21 and to document corresponding curve fit scaling equations to be employed in the normalization of the airfoil self-noise data.

The data presented are the result of hot-wire probe measurements made in the boundary-layer/near-wake region of the sharp TE of the 2D airfoil models. The probes were traversed perpendicular to the model chord lines downstream of the TE. These measurements were made at 0.64 mm from the TE for the 2.54-cm-chord airfoil and at 1.3 mm for the other airfoils. The integral BL parameters—displacement thickness δ^* and momentum thickness θ —were calculated from mean velocity profiles with the BL/near-wake thickness δ specified. The thickness δ is that distance from the airfoil surface where the mean velocity reaches 99 percent of the potential flow stream velocity. The values of δ were chosen by carefully examining the respective turbulent velocity and Reynolds stress distributions as well as the mean profiles. For all cases, the estimated accuracy of δ is within ± 5 percent for the turbulent-boundary-layer (TBL) flow and ± 10 percent for the laminar and transitional flows, whereas the error range for the integral thicknesses δ^* and θ is less (ref. 21).

3.1. Scaled Data

The thicknesses δ and integral properties δ^* and θ at the TE of the sharp TE 2D airfoil models at $\alpha_i = 0^\circ$ are given in figure 6 for both the artificially tripped and the untripped boundary-layer conditions. The subscript 0 for the thicknesses indicates that the airfoil is at zero angle of attack. The parameters are normalized by the chord length c and are given

3.2. Calculation Procedures

The boundary-layer thickness parameters at the TE of a symmetric NACA 0012 airfoil at zero angle of attack are approximated by the curve fits to the data of figure 6. The expressions for the curve fits for boundary-layer thickness δ , displacement thickness δ^* , and momentum thickness θ are, for the *heavily tripped boundary layer*,

$$\delta_0/c = 10^{[1.892 - 0.9045 \log R_c + 0.0596(\log R_c)^2]} \quad (2)$$

$$\delta_0^*/c = \begin{cases} 0.0601 R_c^{-0.114} & (R_c \leq 0.3 \times 10^6) \\ 10^{[3.411 - 1.5397 \log R_c + 0.1059(\log R_c)^2]} & (R_c > 0.3 \times 10^6) \end{cases} \quad (3)$$

$$\theta_0/c = \begin{cases} 0.0723 R_c^{-0.1765} & (R_c \leq 0.3 \times 10^6) \\ 10^{[0.5578 - 0.7079 \log R_c + 0.0404(\log R_c)^2]} & (R_c > 0.3 \times 10^6) \end{cases} \quad (4)$$

as a function of Reynolds number based on the chord R_c . As R_c increases, the thicknesses decrease for both the tripped and the untripped boundary layers. The tripped boundary layers are almost uniformly thicker than the corresponding untripped boundary layers. One should refer to reference 21 for details of the boundary-layer character for the cases of figure 6. In general, however, one can say that the tripped boundary layers are fully turbulent for even the lowest R_c . The untripped boundary layers are laminar or transitional at low R_c and become fully turbulent for high R_c . In figure 6, the boundary-layer thickness data are approximated by curve fits whose equations are specified in the following section.

Angle-of-attack effects on the thickness parameters are given at free-stream velocities of 71.3 and 39.6 m/s for the untripped and tripped BL airfoils in figures 7 and 8. The parameters are normalized by those measured for the corresponding cases at zero angle of attack, given in figure 6. The data are plotted against the corrected angle α_s of equation (1). The collapse of the data is much improved over that when α_i is used (ref. 21). In general, the data show that for increasing α_s (or α_i) the thicknesses increase on the suction side because of the increasing severity of the adverse pressure gradient. The converse is true for the pressure side, where the pressure gradient becomes increasingly favorable. Also included in figures 7 and 8 are curve fits to the data. For the pressure side of the airfoils, the curves are the same for the tripped and untripped cases. The suction side curves differ, reflecting differences in the angle dependence of where the TE boundary layer separates and finally stalls the airfoil.

In reference 21, the data are discussed and compared with flat plate experimental results and results from boundary-layer prediction codes.

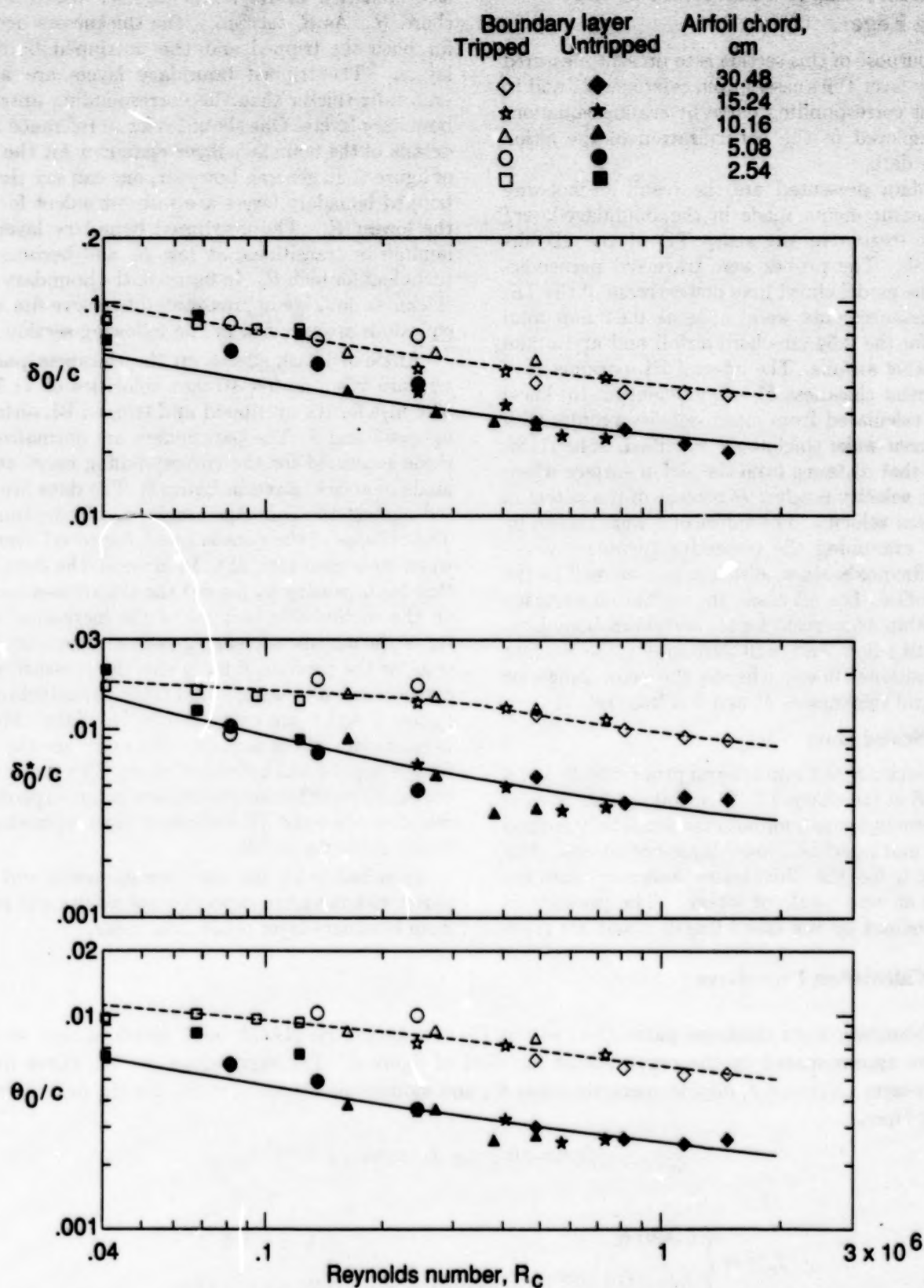
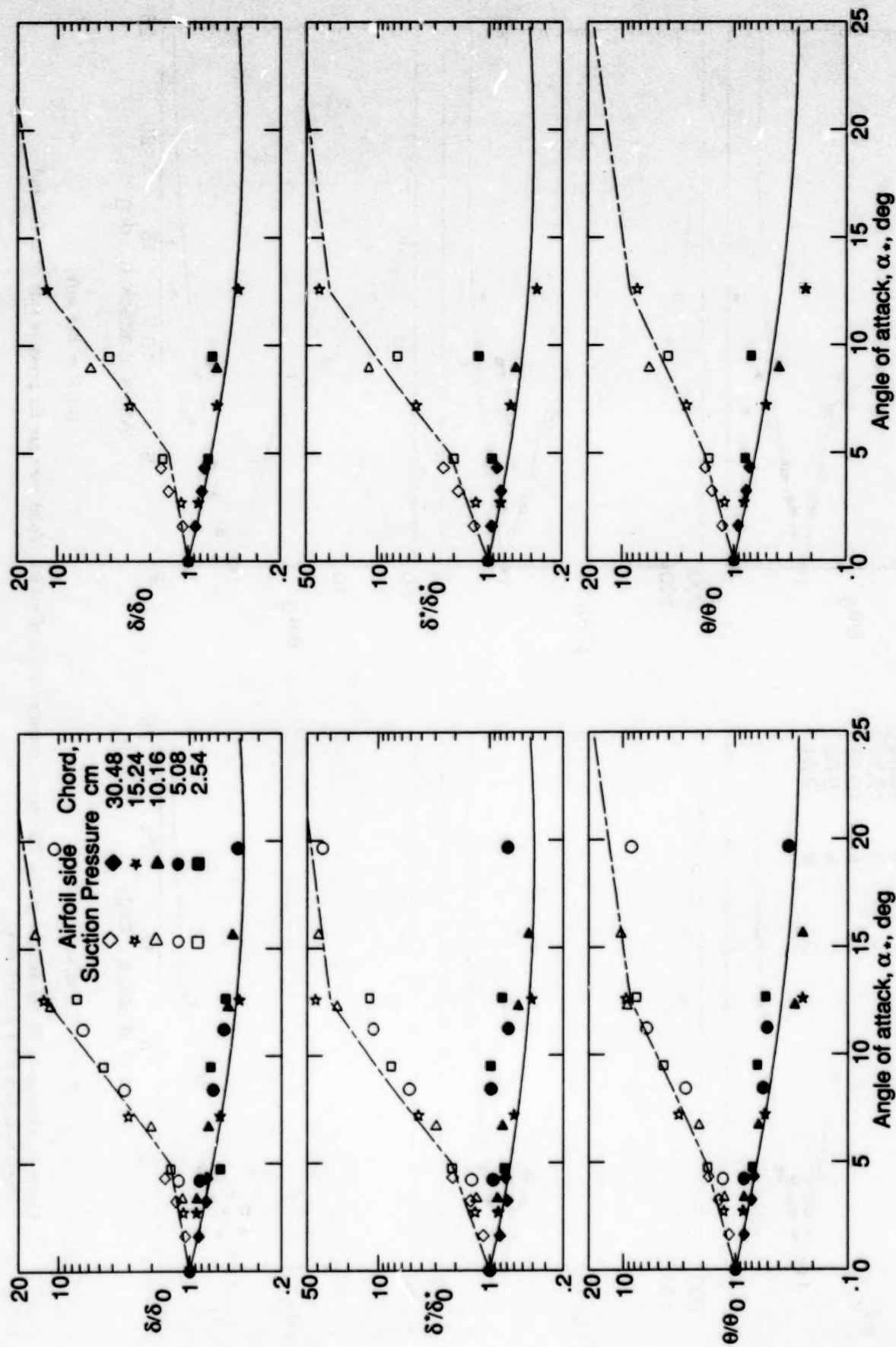


Figure 6. Boundary-layer thicknesses at the trailing edge of 2D airfoil models at angle of attack of zero. Solid lines are for untripped BL and broken lines are for tripped BL.



(a) $U = 71.3$ m/s.

(b) $U = 39.6$ m/s.

Figure 7. Tripped BL thicknesses at the TE versus corrected angle of attack. Solid lines are for pressure side of airfoil and broken lines are for suction side.

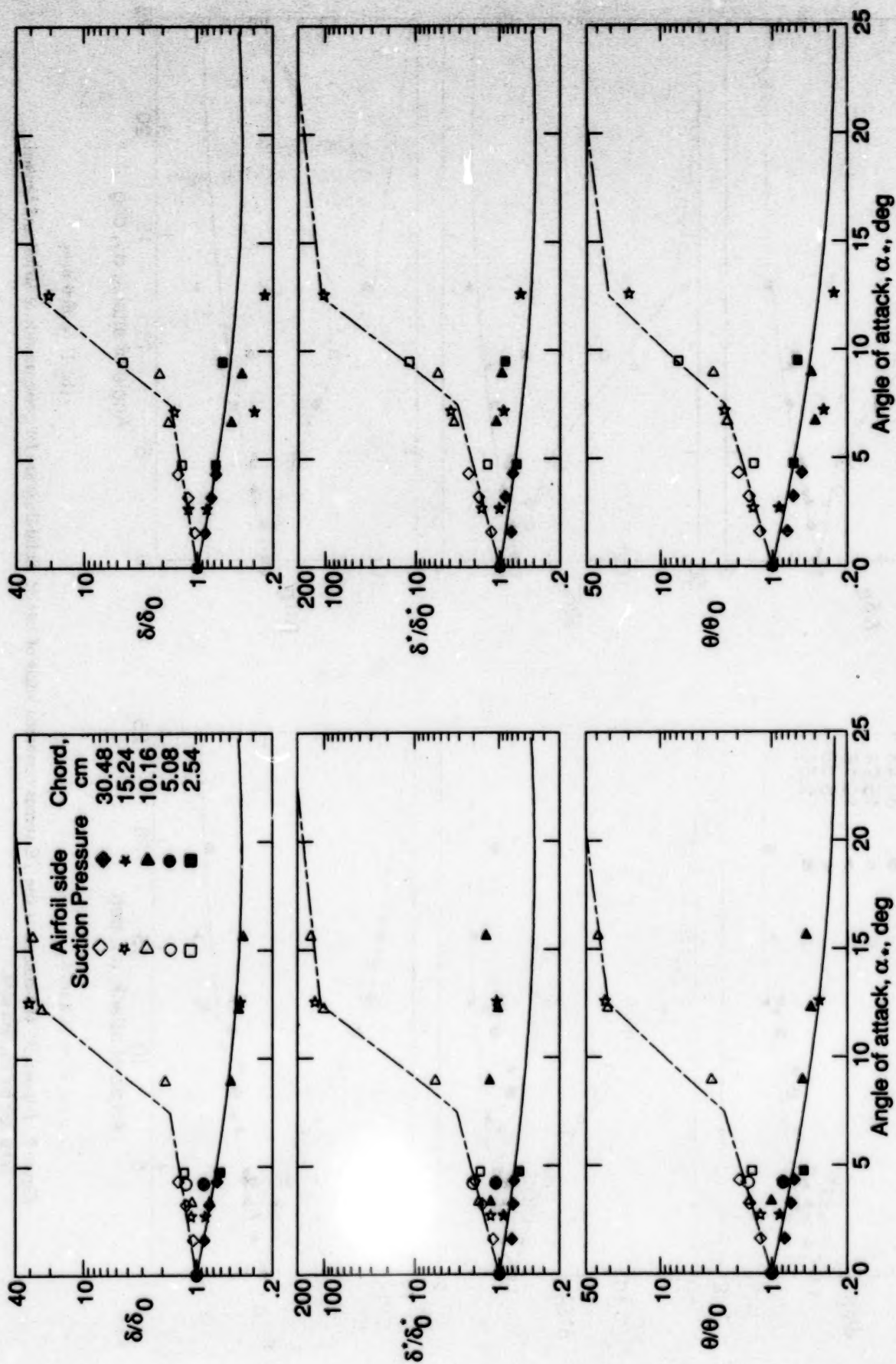
(a) $U = 71.3$ m/s.(b) $U = 39.6$ m/s.

Figure 8. Untripped BL thicknesses at the TE versus corrected angle of attack. Solid lines are for pressure side of airfoil and broken lines are for suction side.

where the zero subscripts indicate zero angle of attack, zero lift on these symmetric airfoils. For the *untripped* (natural transition) *boundary layers*,

$$\delta_0/c = 10^{[1.6589 - 0.9045 \log R_c + 0.0596(\log R_c)^2]} \quad (5)$$

$$\delta_0^*/c = 10^{[3.0187 - 1.5397 \log R_c + 0.1059(\log R_c)^2]} \quad (6)$$

$$\theta_0/c = 10^{[0.2021 - 0.7079 \log R_c + 0.0404(\log R_c)^2]} \quad (7)$$

The boundary-layer thicknesses for the airfoils at nonzero angle of attack, in terms of the zero-angle-of-attack thicknesses and the corrected angles α_* , are given in figures 7 and 8. The expressions for the curve fits for the *pressure side*, for both the *tripped* and the *untripped boundary layers*, are

$$\frac{\delta_p}{\delta_0} = 10^{[-0.04175\alpha_* + 0.00106\alpha_*^2]} \quad (8)$$

$$\frac{\delta_p^*}{\delta_0^*} = 10^{[-0.0432\alpha_* + 0.00113\alpha_*^2]} \quad (9)$$

$$\frac{\theta_p}{\theta_0} = 10^{[-0.04508\alpha_* + 0.000873\alpha_*^2]} \quad (10)$$

For the suction side, the parametric behavior of the thicknesses depends on whether the boundary layers are attached, separated near the trailing edge, or separated a sufficient distance upstream to produce stall. For the *suction side for the tripped boundary layers* (fig. 7),

$$\frac{\delta_s}{\delta_0} = \begin{cases} 10^{0.0311\alpha_*} & (0^\circ \leq \alpha_* \leq 5^\circ) \\ 0.3468(10^{0.1231\alpha_*}) & (5^\circ < \alpha_* \leq 12.5^\circ) \\ 5.718(10^{0.0258\alpha_*}) & (12.5^\circ < \alpha_* \leq 25^\circ) \end{cases} \quad (11)$$

$$\frac{\delta_s^*}{\delta_0^*} = \begin{cases} 10^{0.0679\alpha_*} & (0^\circ \leq \alpha_* \leq 5^\circ) \\ 0.381(10^{0.1516\alpha_*}) & (5^\circ < \alpha_* \leq 12.5^\circ) \\ 14.296(10^{0.0258\alpha_*}) & (12.5^\circ < \alpha_* \leq 25^\circ) \end{cases} \quad (12)$$

$$\frac{\theta_s}{\theta_0} = \begin{cases} 10^{0.0559\alpha_*} & (0^\circ \leq \alpha_* \leq 5^\circ) \\ 0.6984(10^{0.0869\alpha_*}) & (5^\circ < \alpha_* \leq 12.5^\circ) \\ 4.0846(10^{0.0258\alpha_*}) & (12.5^\circ < \alpha_* \leq 25^\circ) \end{cases} \quad (13)$$

For the suction side for the untripped boundary layers (fig. 8),

$$\frac{\delta_r}{\delta_0} = \begin{cases} 10^{0.03114\alpha_s} & (0^\circ \leq \alpha_s \leq 7.5^\circ) \\ 0.0303(10^{0.2336\alpha_s}) & (7.5^\circ < \alpha_s \leq 12.5^\circ) \\ 12(10^{0.0258\alpha_s}) & (12.5^\circ < \alpha_s \leq 25^\circ) \end{cases} \quad (14)$$

$$\frac{\delta_s^*}{\delta_0^*} = \begin{cases} 10^{0.0679\alpha_s} & (0^\circ \leq \alpha_s \leq 7.5^\circ) \\ 0.0162(10^{0.3066\alpha_s}) & (7.5^\circ < \alpha_s \leq 12.5^\circ) \\ 52.42(10^{0.0258\alpha_s}) & (12.5^\circ < \alpha_s \leq 25^\circ) \end{cases} \quad (15)$$

$$\frac{\theta_s}{\theta_0} = \begin{cases} 10^{0.0559\alpha_s} & (0^\circ \leq \alpha_s \leq 7.5^\circ) \\ 0.0633(10^{0.2157\alpha_s}) & (7.5^\circ < \alpha_s \leq 12.5^\circ) \\ 14.977(10^{0.0258\alpha_s}) & (12.5^\circ < \alpha_s \leq 25^\circ) \end{cases} \quad (16)$$

4. Acoustic Measurements

The aim of the acoustic measurements was to determine spectra for self-noise from airfoils encountering smooth airflow. This task is complicated by the unavoidable presence of extraneous tunnel test rig noise. In this section, cross-correlations between microphones are examined to identify the self-noise emitted from the TE in the presence of other sources. Then, the spectra of self-noise are determined by performing Fourier transforms of cross-correlation data which have been processed and edited to eliminate the extraneous contributions. The results are presented as 1/3-octave spectra, which then form the data base from which the self-noise scaling prediction equations are developed.

4.1. Source Identification

The upper curves in figure 9 are the cross-correlations, $R_{12}(\tau) = \langle p_1(t)p_2(t+\tau) \rangle$, between the sound pressure signals p_1 and p_2 of microphones M1 and M2 identified in figure 4. Presented are cross-correlations both with and without the tripped 30.48-cm-chord airfoil mounted in the test rig. Because the microphones were on opposite sides of, and at equal distance from, the airfoil, a negative correlation peak occurs at a signal delay time τ of 0. This correlation is consistent with a broadband noise source of dipole character, whose phase is reversed on opposing sides. When the airfoil is removed, the strong negative peak disappears leaving the contribution from the test rig alone. The most coherent parts of this noise are from the lips of the nozzle and are, as with the airfoil noise, of a dipole character. The microphone time delays predicted for these sources are indicated by arrows. The predictions account for the effect of refraction of sound by the free-jet shear layer (refs. 22 and 23), as well as the geometric relationship between the microphones and the hardware and the speed of sound.

The lower curves in figure 9 are the cross-correlations, $R_{45}(\tau)$, between microphones M4 and M5. The predicted delay times again appear to correctly identify the correlation peaks associated with the noise emission locations. The peaks are positive for $R_{45}(\tau)$ because both microphones are on the same side of the dipoles' directional lobes. The noise field is dominated by TE noise. Any contribution to the noise field from the LE would appear where indicated in the figure. As is subsequently shown, there are contributions in many cases. For such cases the negative correlation peak for $R_{12}(\tau)$ would be the sum of the TE and LE correlation peaks brought together at $\tau = 0$ and inverted in sign.

In figure 10, the cross-correlations $R_{45}(\tau)$ are shown for tripped BL airfoils of various sizes. The TE noise correlation peaks are at $\tau_{TE} = -0.11$ ms

for all cases because at $\alpha_i = 0^\circ$, the TE location of all models is the same. The LE location changes with chord size, as is indicated by the change in the predicted LE noise correlation peak delay times.

For the larger airfoils in figure 10, the TE contribution dominates the noise field. As the chord length decreases, the LE noise peaks increase to become readily identifiable in the correlation. For the smallest chord the LE contribution is even somewhat more than that of the TE. Note the extraneous, but inconsequential, source of discrete low-frequency noise contributing to the 22.86-cm-chord correlation, which can be readily edited in a spectral format.

It is shown in reference 6 that the LE and TE sources are uncorrelated. The origin of LE noise appears to be inflow turbulence to the LE from the TBL of the test rig side plates. This should be the case even though the spanwise extent of this TBL is small compared with the portion of the models that encounter uniform low-turbulence flow from the nozzle. Inflow turbulence can be a very efficient noise mechanism (ref. 24); however its full efficiency can be obtained only when the LE of the model is relatively sharp compared with the scale of the turbulence. The LE noise contributions diminish for the large chord because of the proportional increase in LE radius with chord. When this radius increases to a size that is large compared with the turbulent scale in the side plate TBL, then the sectional lift fluctuations associated with inflow turbulence noise are not developed.

4.2. Correlation Editing and Spectral Determination

The cross-spectrum between microphones M1 and M2, denoted $G_{12}(f)$, is the Fourier transform of $R_{12}(\tau)$. If the contributions from the LE, nozzle lips, and any other coherent extraneous source locations were removed, $G_{12}(f)$ would equal the autospectrum of the airfoil TE self-noise, $S(f)$. Actually the relationship would be $G_{12}(f) = S(f) \exp[i(2\pi f \tau_{TE} \pm \pi)]$, where $i = \sqrt{-1}$ and τ_{TE} is the delay time of the TE correlation peak. This approach is formalized in reference 2.

In reference 6, the spectra were found from $G_{12}(f)$ determined with the models of the test rig after a point-by-point vectorial subtraction of $G_{12}(f)$ determined with the airfoil removed. This was equivalent to subtracting corresponding $R_{12}(\tau)$ results, such as those of figure 9, and then taking the Fourier transform. This resulted in "corrected" spectra which were devoid of at least a portion of the background test rig noise, primarily emitted from the nozzle lips. The spectra still were contaminated by the LE noise due to the inflow turbulence.

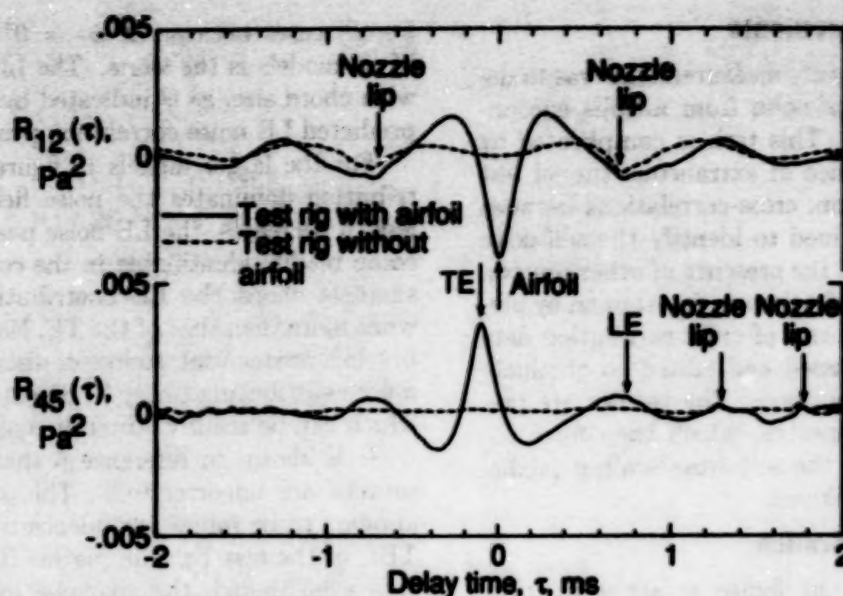


Figure 9. Cross-correlations for two microphone pairs with and without airfoil mounted in test rig. $c = 30.48$ cm; BL tripped; $\alpha_i = 0^\circ$; $U = 71.3$ m/s. Arrows indicate predicted values of τ . (From ref. 6.)

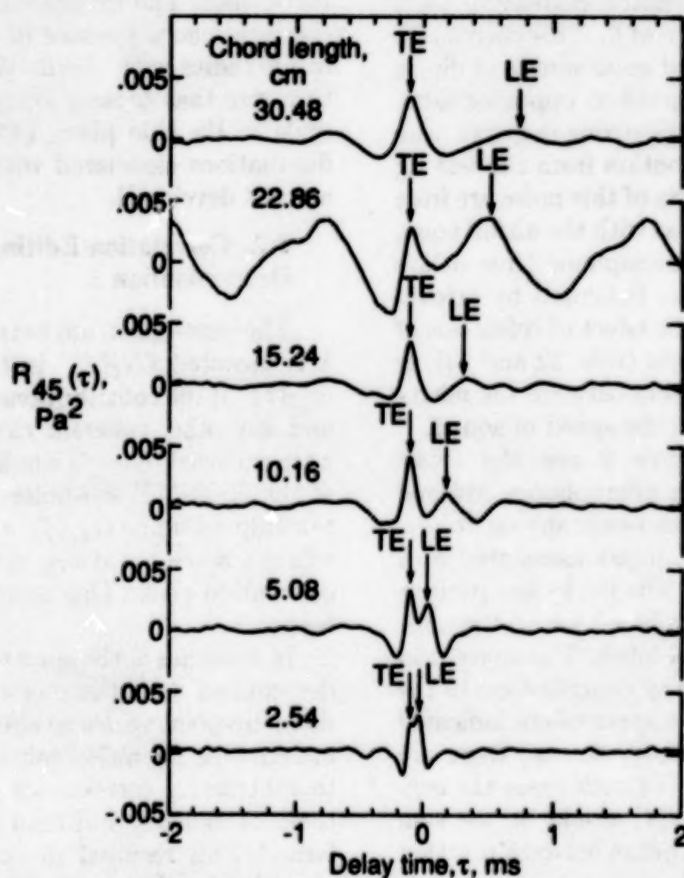


Figure 10. Cross-correlations between microphones M4 and M5 for tripped BL airfoils of various chord sizes. $U = 71.3$ m/s. Arrows indicate predicted values of τ . (From ref. 6.)

In the present paper, most spectra presented were obtained by taking the Fourier transform of microphone-pair cross-correlations which had been edited to eliminate LE noise (see details in appendix A). The microphone pairs used included M4 and M5, M4 and M8, and M4 and M2. These pairs produced correlations where the TE and LE noise peaks were generally separated and readily identifiable. Referring to figure 10 for $R_{45}(\tau)$, the approach was to employ only the left-hand side (LHS) of the TE noise peak. The LHS was "folded" about τ at the peak (τ_{TE}) to produce a nearly symmetrical correlation. Care was taken in the processing to maintain the actual shapes near the very peak, to avoid to the extent possible the artificial introduction of high-frequency noise in the resulting spectra. Cross-spectra were then determined which were equated to the spectra of TE self-noise.

The data processing was straightforward for the larger chord airfoils because the LE and TE peaks were sufficiently separated from one another that the influence of the LE did not significantly impact the TE noise correlation shapes. For many of the smaller airfoils, such as those with chord lengths of 2.54, 5.08, and 10.16 cm shown in figure 10, the closeness of the LE contribution distorted the TE noise correlation. A processing procedure was developed to effectively "separate" the TE and LE peaks to a sufficient distance from one another, within the correlation presentation, so that the correlation folding of the LHS about τ_{TE} produced a more accurate presentation of the TE noise correlation shape. The separation processing employed symmetry assumptions for the TE and LE noise correlations to allow manipulation of the correlation records. This processing represented a contamination removal method used for about one-

quarter of the spectra presented for the three smallest airfoil chord lengths. Each case was treated individually to determine whether correlation folding alone, folding after the separation processing, or not folding at all produced spectra containing the least apparent error. In appendix A, details of the editing and Fourier transform procedures, as well as the separation processing, are given.

4.3. Self-Noise Spectra

The self-noise spectra for the 2D NACA 0012 airfoil models with sharp TE are presented in a 1/3-octave format in figures 11 to 74. Figures 11 to 43 are for airfoils where the boundary layers have been tripped and figures 44 to 74 are for smooth surface airfoils where the boundary layers are untripped (natural transition). Each figure contains spectra for a model at a specific angle of attack for various tunnel speeds. Note that the spectra are truncated at upper and lower frequencies. This editing of the spectra was done because, as described in appendix A, a review of the narrow-band amplitude and phase for all cases revealed regions where extraneous noise affected the spectra in a significant way (2 dB or more). These regions were removed from the 1/3-octave presentations.

The spectra levels have been corrected for shear layer diffraction and TE noise directivity effects, as detailed in appendix B. The noise should be that for an observer positioned perpendicular to, and 1.22 m from, the TE and the model midspan. In terms of the directivity definitions of appendix B, $r_e = 1.22$ m, $\Theta_e = 90^\circ$, and $\Phi_e = 90^\circ$. In section 5 (beginning on p. 51), the character and parametric behavior of the self-noise, as well as the predictions which are compared with the data, are discussed.

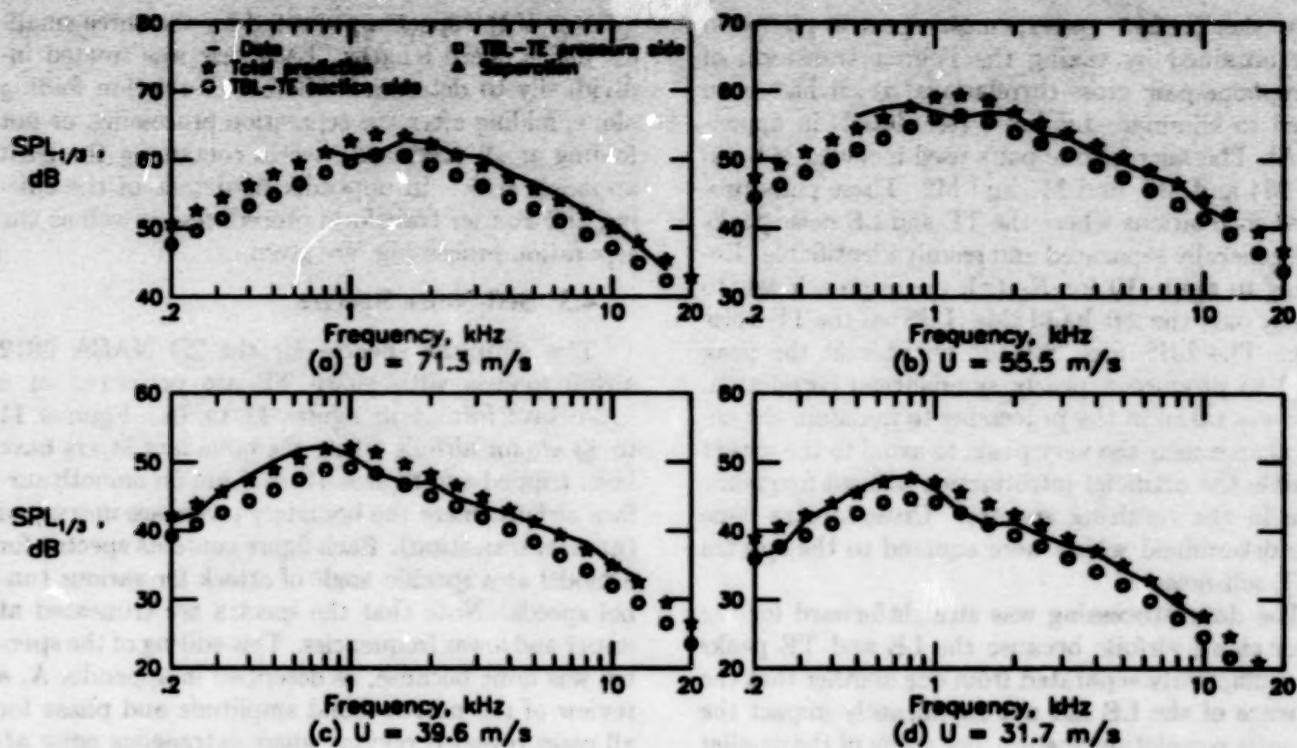


Figure 11. Self-noise spectra for 30.48-cm-chord airfoil with tripped BL at $\alpha_t = 0^\circ$ ($\alpha_\infty = 0^\circ$).

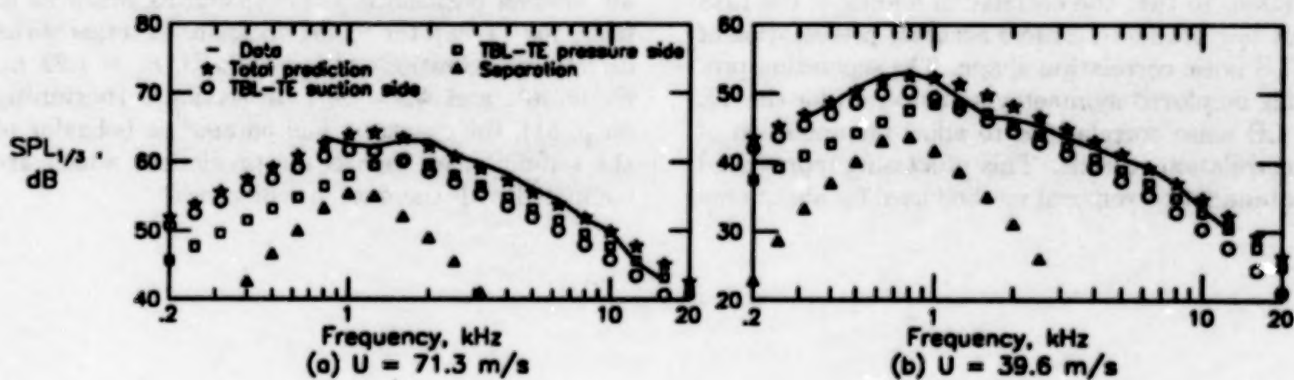


Figure 12. Self-noise spectra for 30.48-cm-chord airfoil with tripped BL at $\alpha_t = 5.4^\circ$ ($\alpha_\infty = 1.5^\circ$).

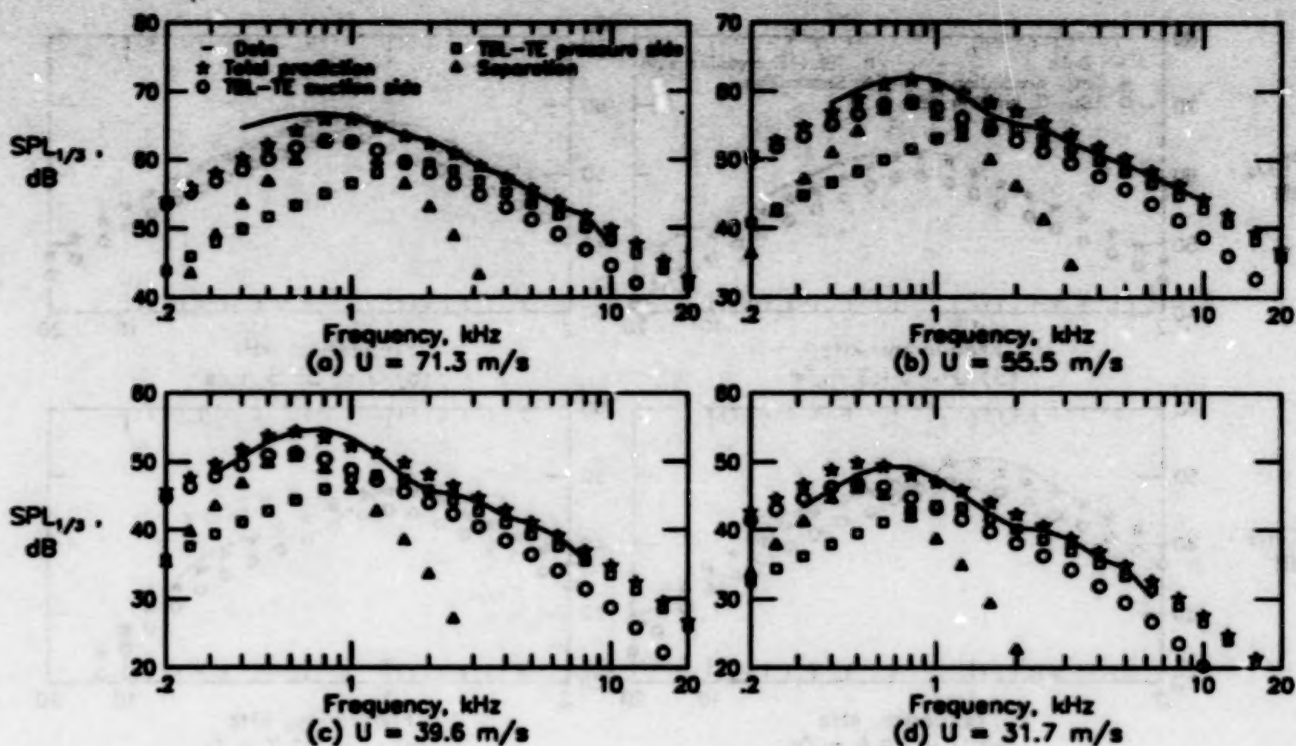


Figure 13. Self-noise spectra for 30.48-cm-chord airfoil with tripped BL at $\alpha_t = 10.6^\circ$ ($\alpha_o = 3.0^\circ$).

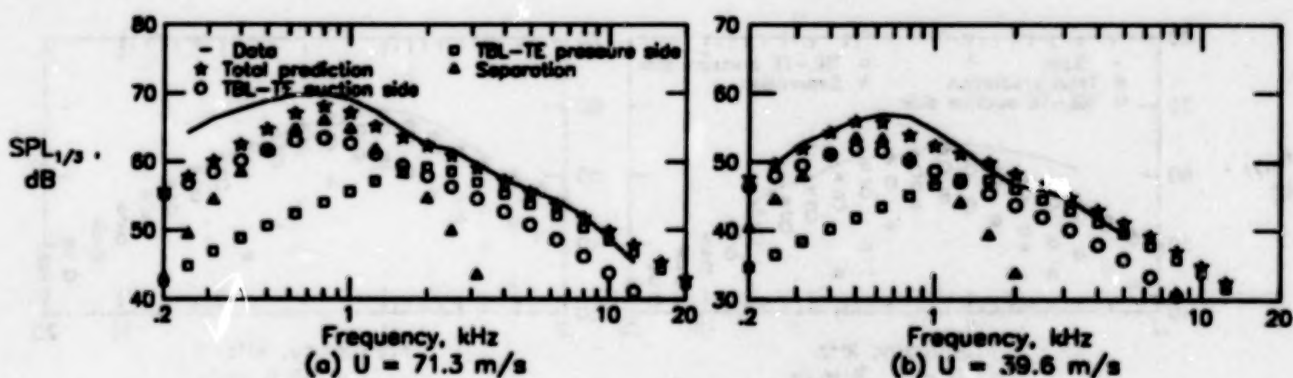


Figure 14. Self-noise spectra for 30.48-cm-chord airfoil with tripped BL at $\alpha_t = 14.4^\circ$ ($\alpha_o = 4.0^\circ$).

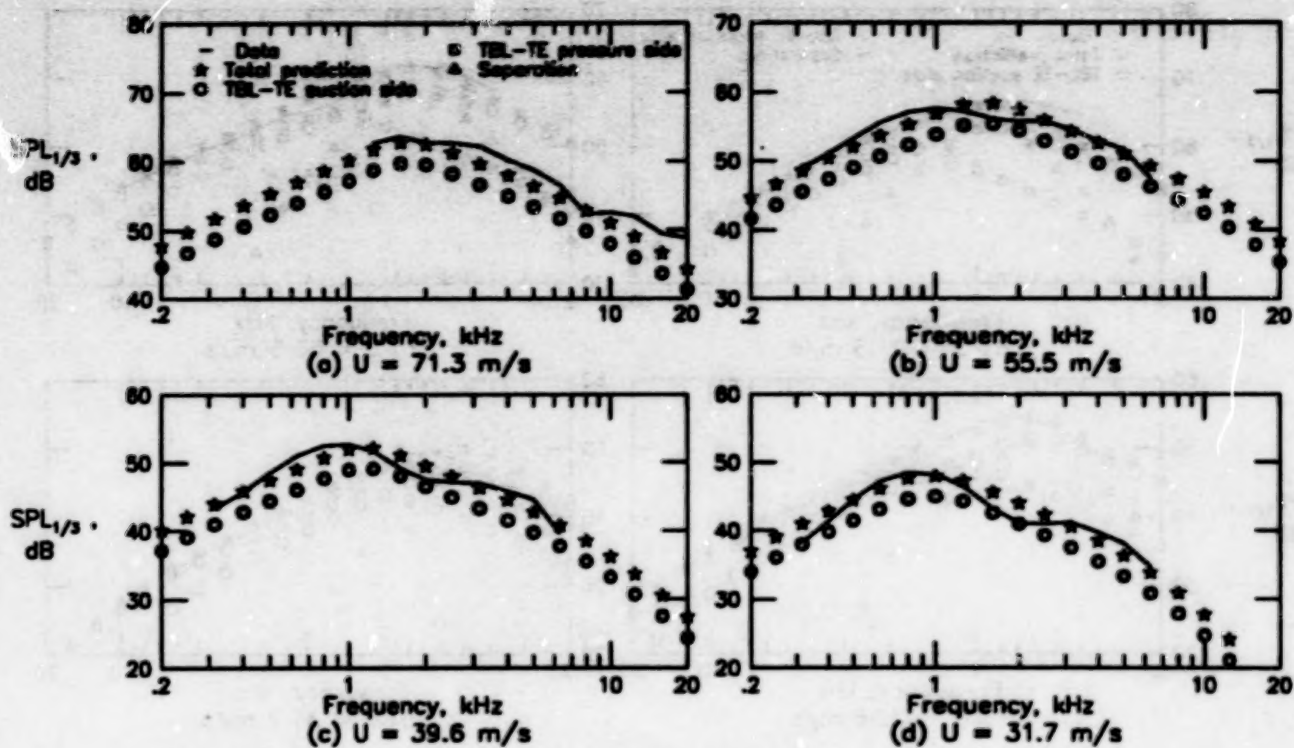


Figure 15. Self-noise spectra for 22.86-cm-chord airfoil with tripped BL at $\alpha_t = 0^\circ$ ($\alpha_s = 0^\circ$).

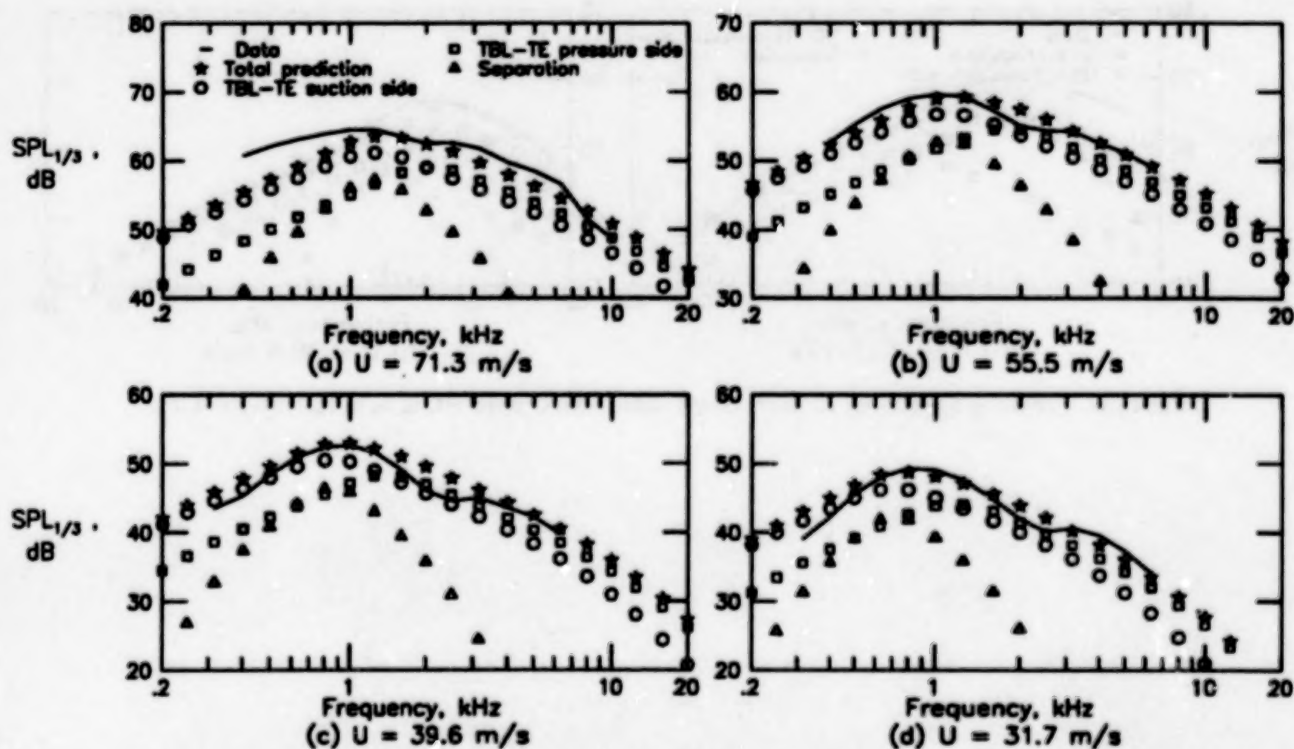


Figure 16. Self-noise spectra for 22.86-cm-chord airfoil with tripped BL at $\alpha_t = 5.4^\circ$ ($\alpha_s = 2.0^\circ$).

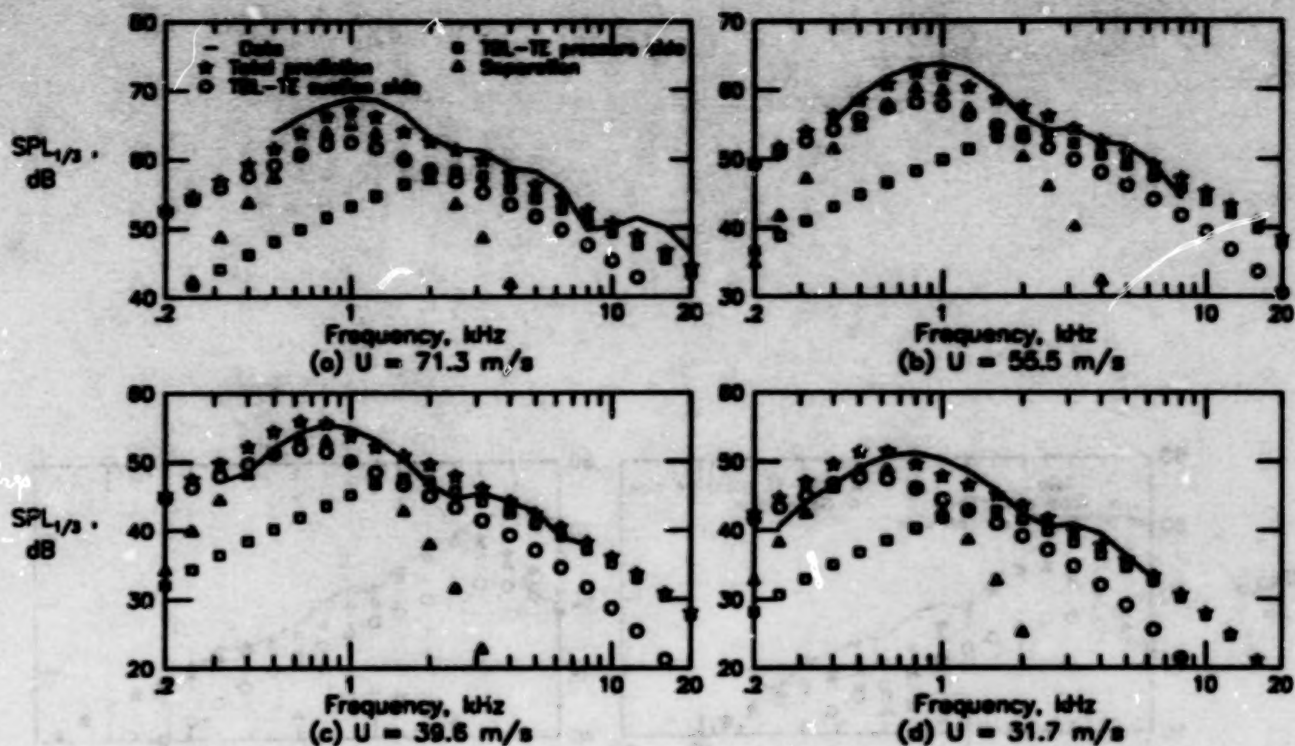


Figure 17. Self-noise spectra for 22.86-cm-chord airfoil with tripped BL at $\alpha_i = 10.8^\circ$ ($\alpha = 4.0^\circ$).

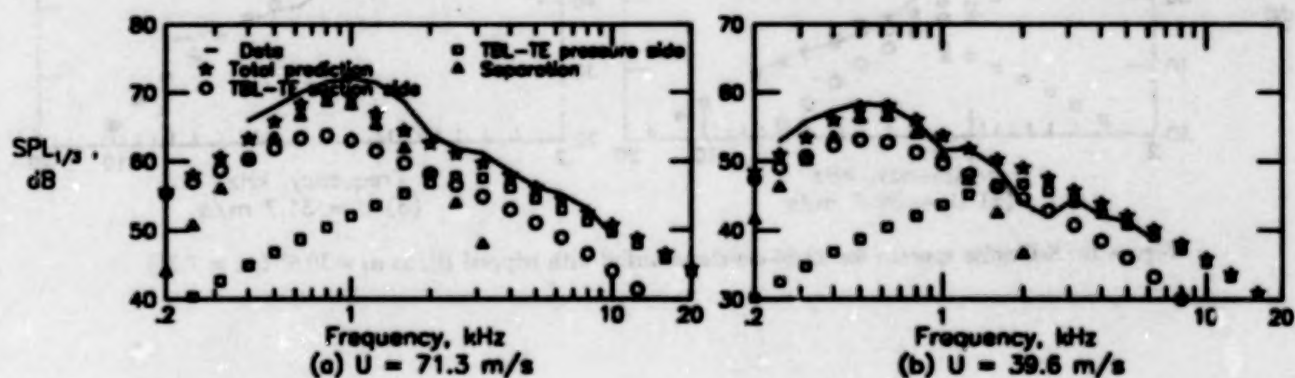


Figure 18. Self-noise spectra for 22.86-cm-chord airfoil with tripped BL at $\alpha_i = 14.4^\circ$ ($\alpha = 5.3^\circ$).

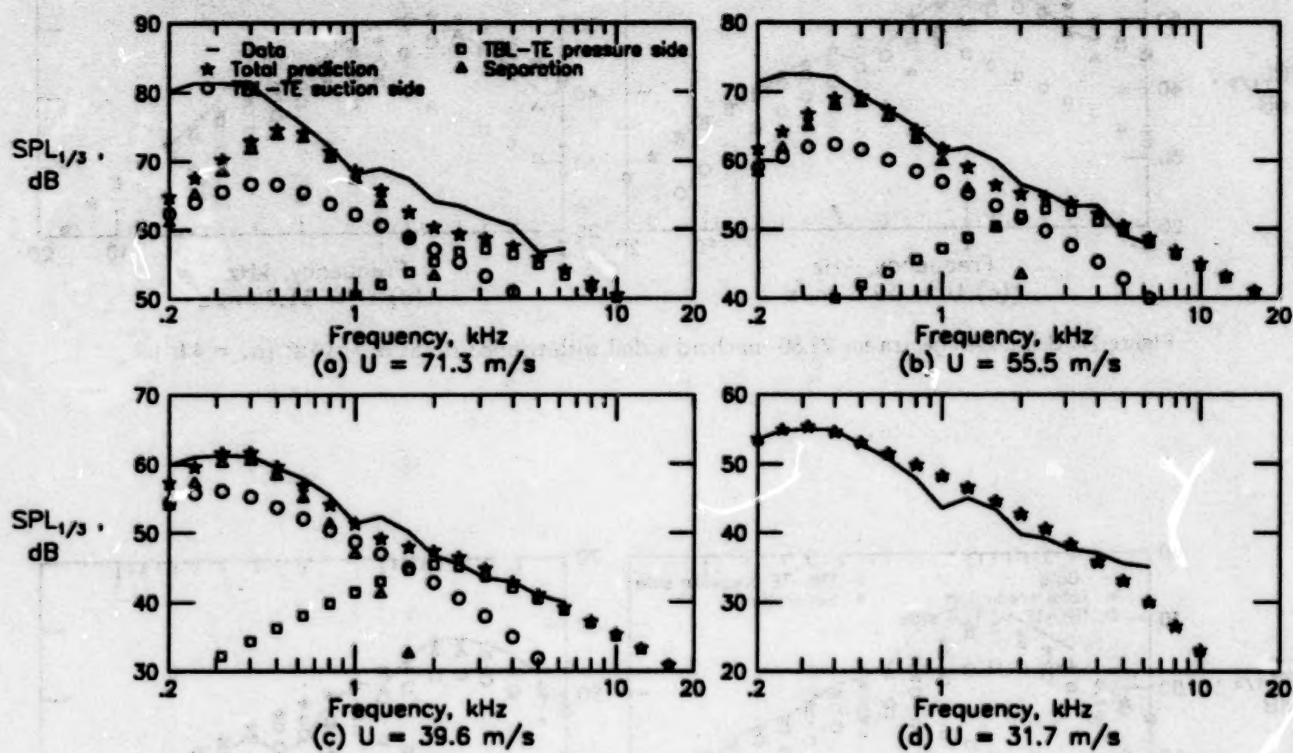


Figure 19. Self-noise spectra for 22.86-cm-chord airfoil with tripped BL at $\alpha_t = 19.8^\circ$ ($\alpha_s = 7.3^\circ$).

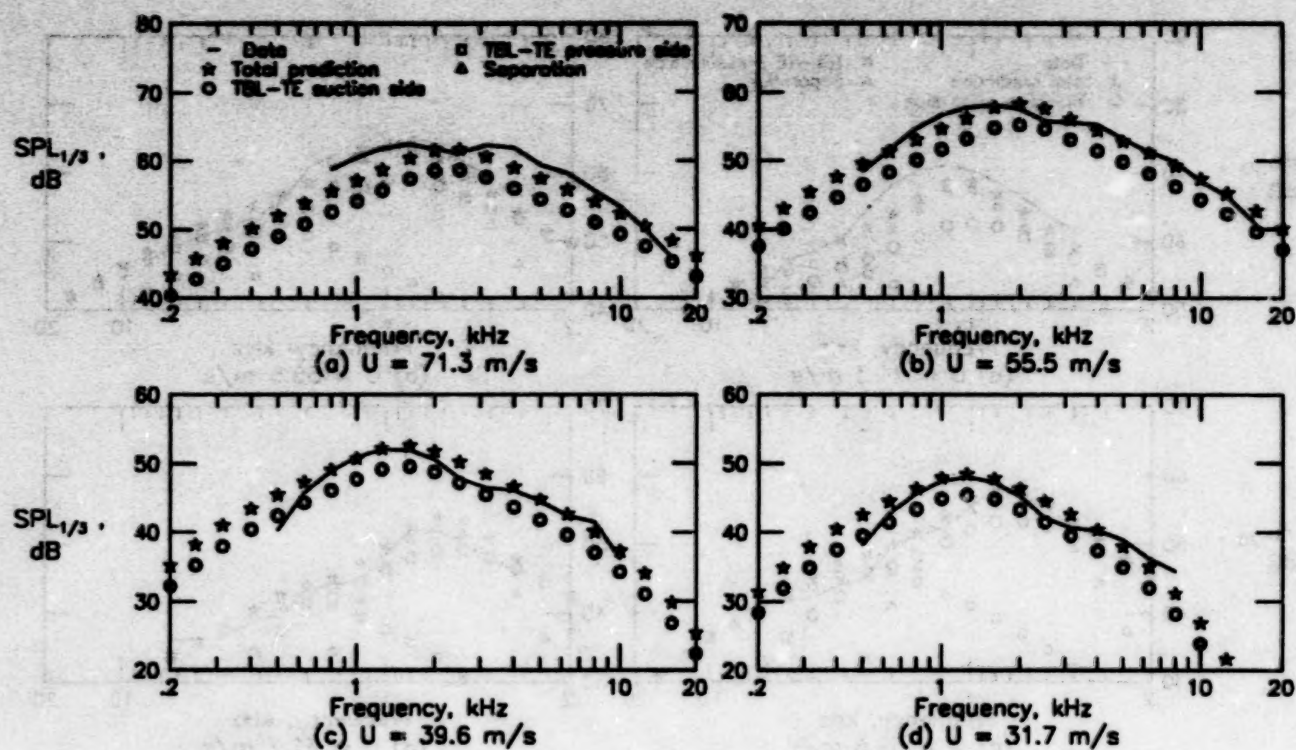


Figure 20. Self-noise spectra for 15.24-cm-chord airfoil with tripped BL at $\alpha_t = 0^\circ$ ($\alpha_s = 0^\circ$).

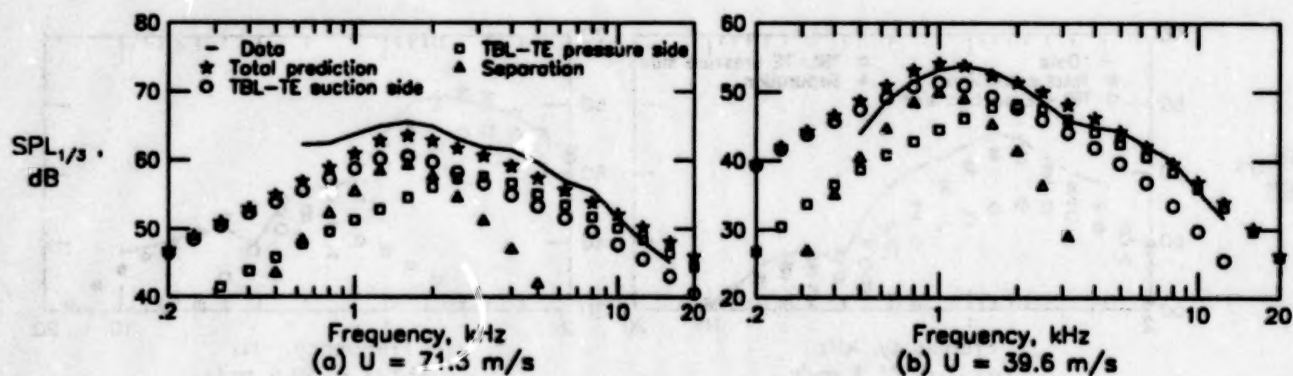


Figure 21. Self-noise spectra for 15.24-cm-chord airfoil with tripped BL at $\alpha_t = 5.4^\circ$ ($\alpha_s = 2.7^\circ$).

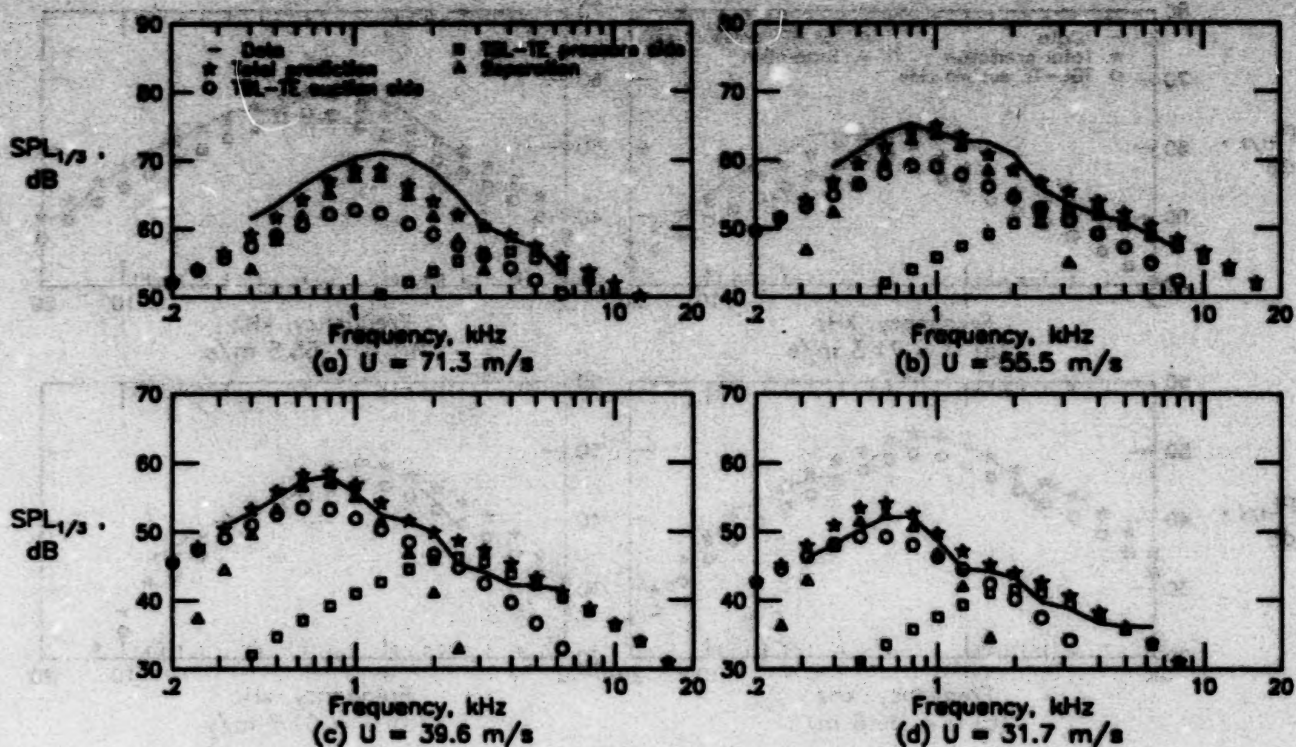


Figure 22. Self-noise spectra for 15.24-cm-chord airfoil with tripped BL at $\alpha_i = 10.8^\circ$ ($\alpha_o = 5.4^\circ$).

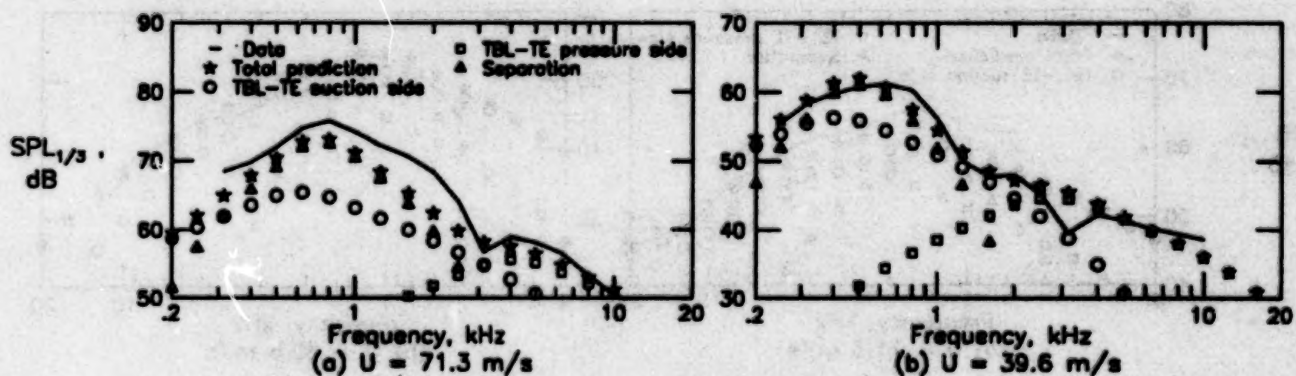


Figure 23. Self-noise spectra for 15.24-cm-chord airfoil with tripped BL at $\alpha_i = 14.4^\circ$ ($\alpha_o = 7.2^\circ$).

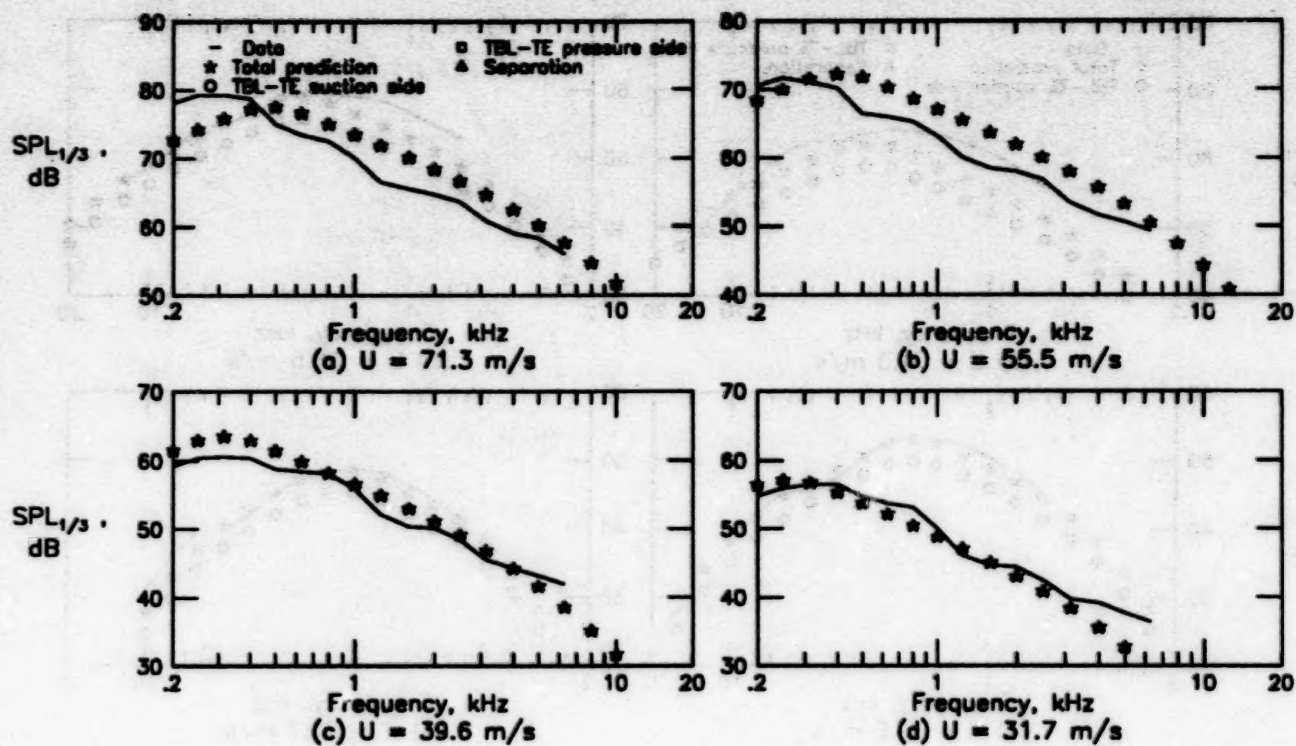


Figure 24. Self-noise spectra for 15.24-cm-chord airfoil with tripped BL at $\alpha_t = 19.8^\circ$ ($\alpha_s = 9.9^\circ$).

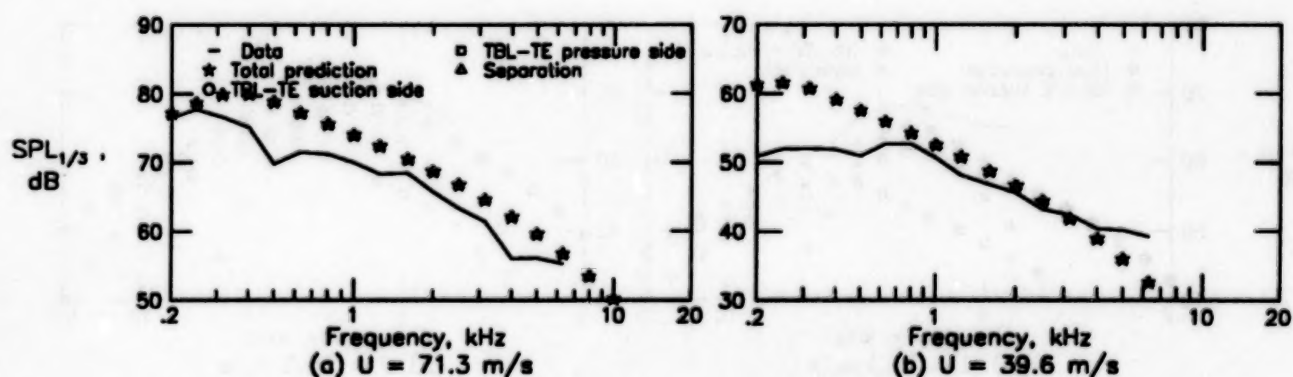


Figure 25. Self-noise spectra for 15.24-cm-chord airfoil with tripped BL at $\alpha_t = 25.2^\circ$ ($\alpha_s = 12.6^\circ$).

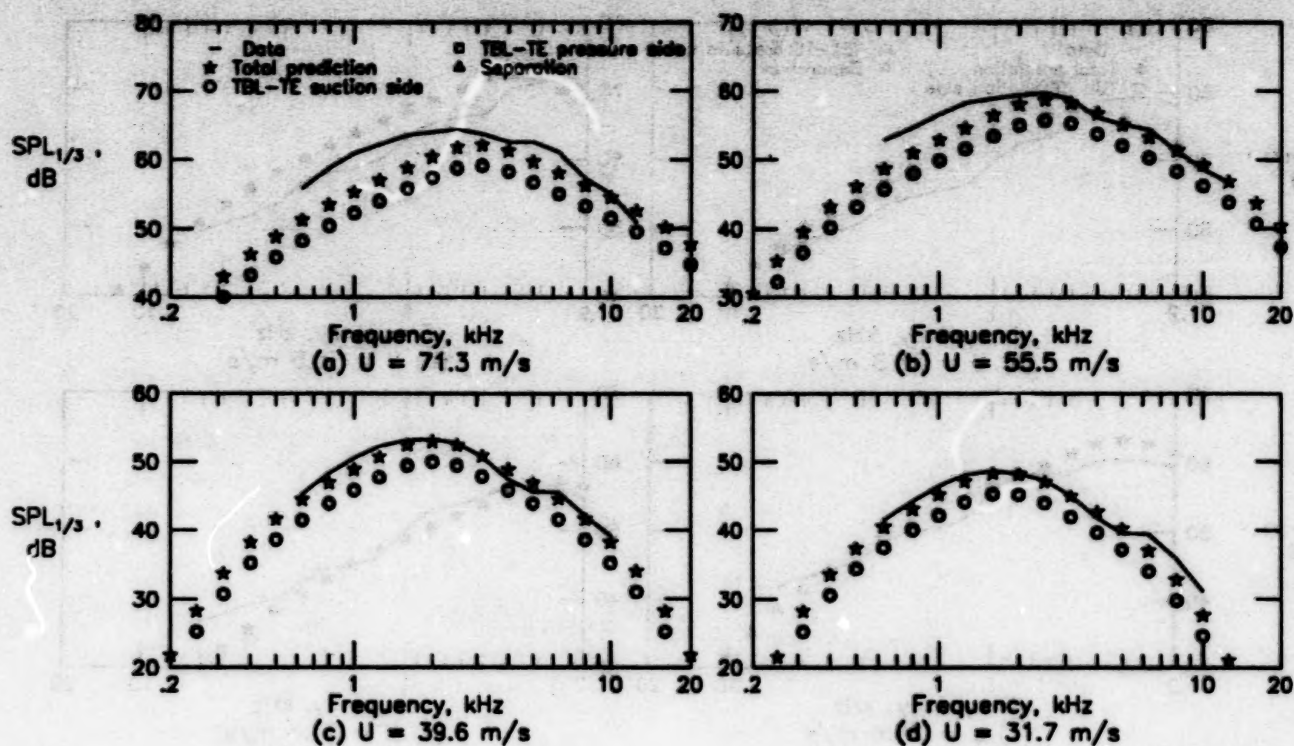


Figure 26. Self-noise spectra for 10.16-cm-chord airfoil with tripped BL at $\alpha_t = 0^\circ$ ($\alpha_s = 0^\circ$).

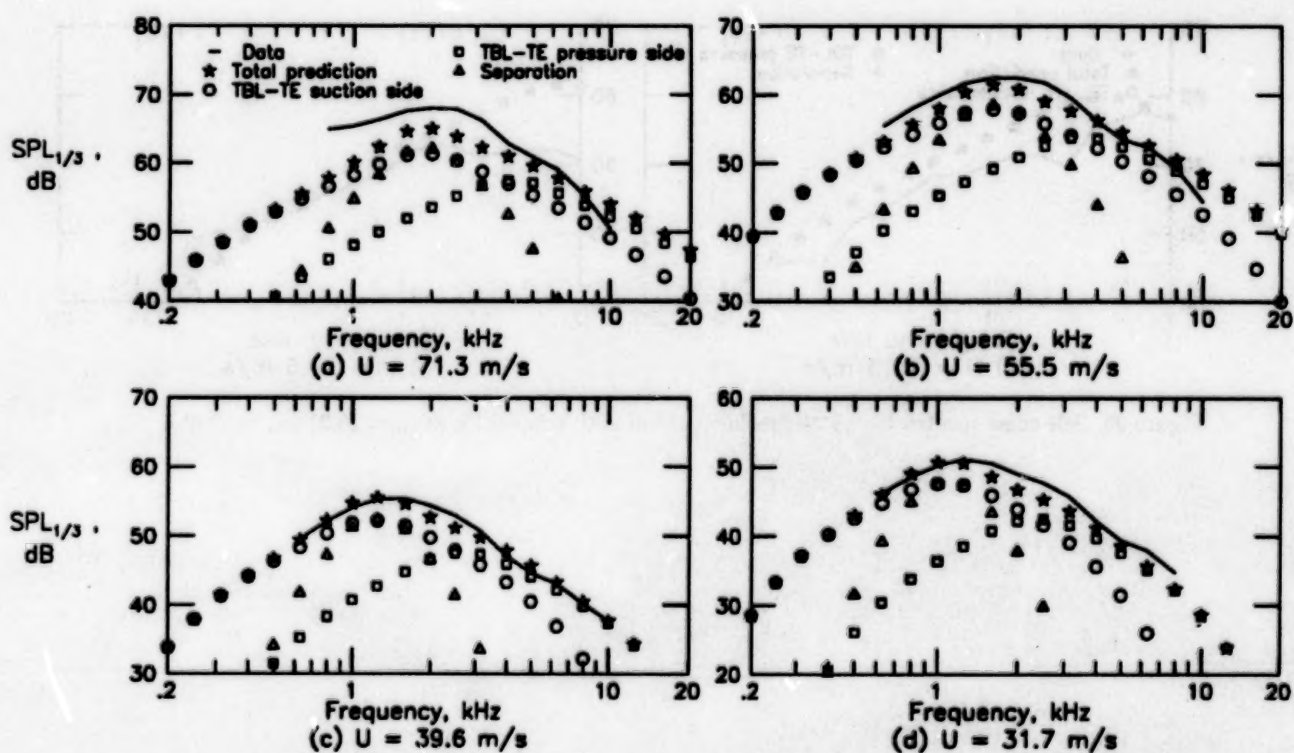


Figure 27. Self-noise spectra for 10.16-cm-chord airfoil with tripped BL at $\alpha_t = 5.4^\circ$ ($\alpha_s = 3.3^\circ$).

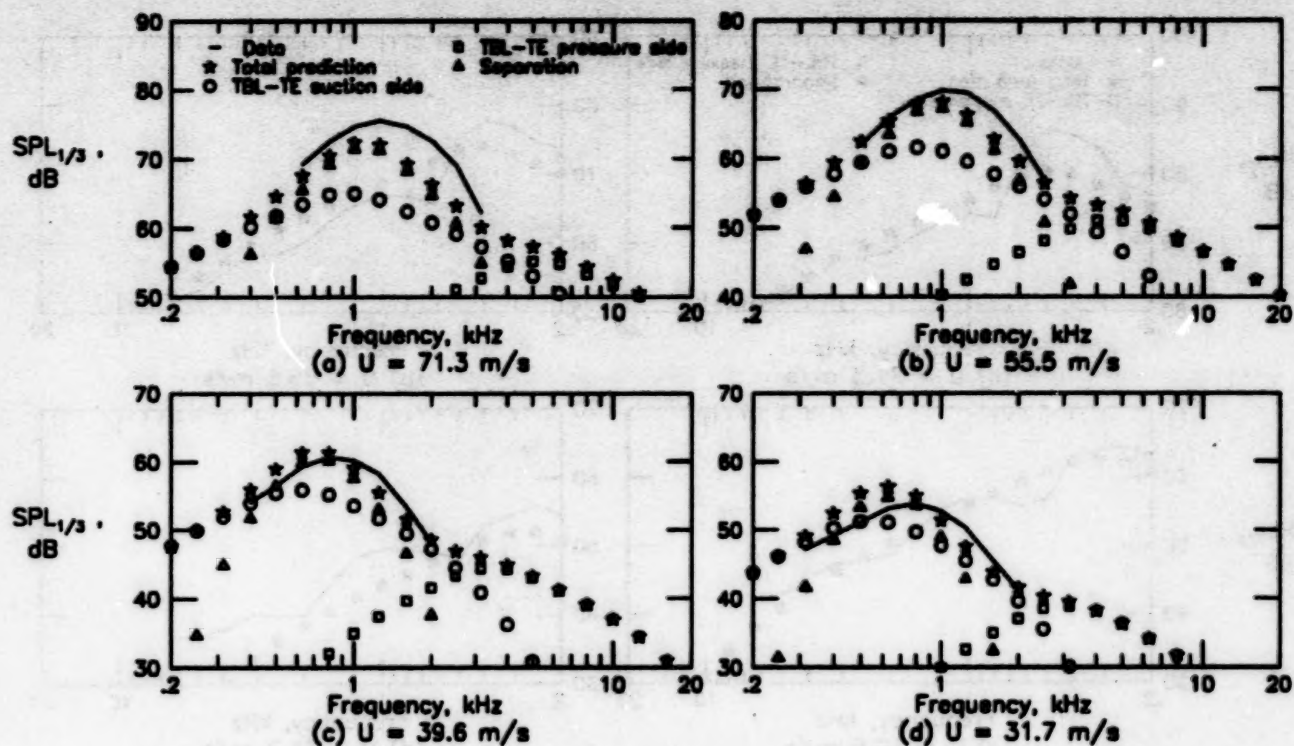


Figure 28. Self-noise spectra for 10.16-cm-chord airfoil with tripped BL at $\alpha_t = 10.8^\circ$ ($\alpha_o = 6.7^\circ$).

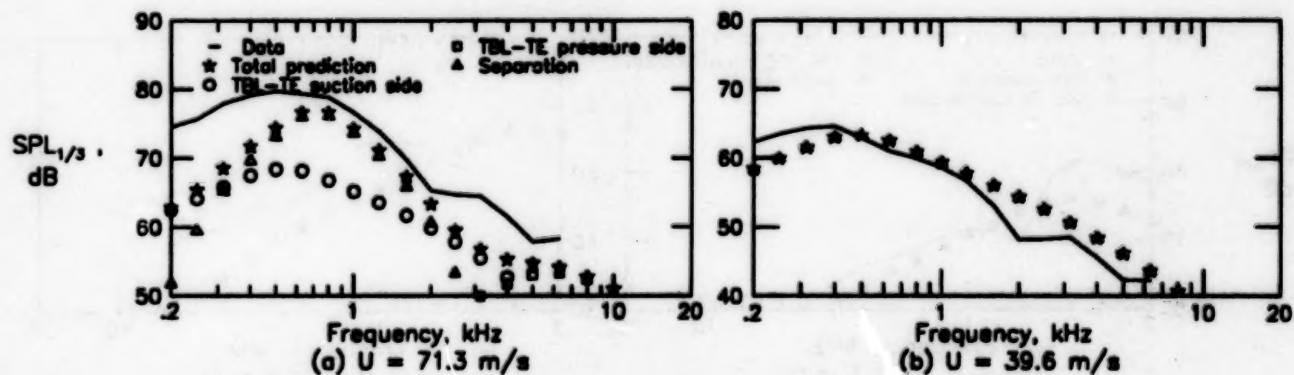


Figure 29. Self-noise spectra for 10.16-cm-chord airfoil with tripped BL at $\alpha_t = 14.4^\circ$ ($\alpha_o = 8.9^\circ$).

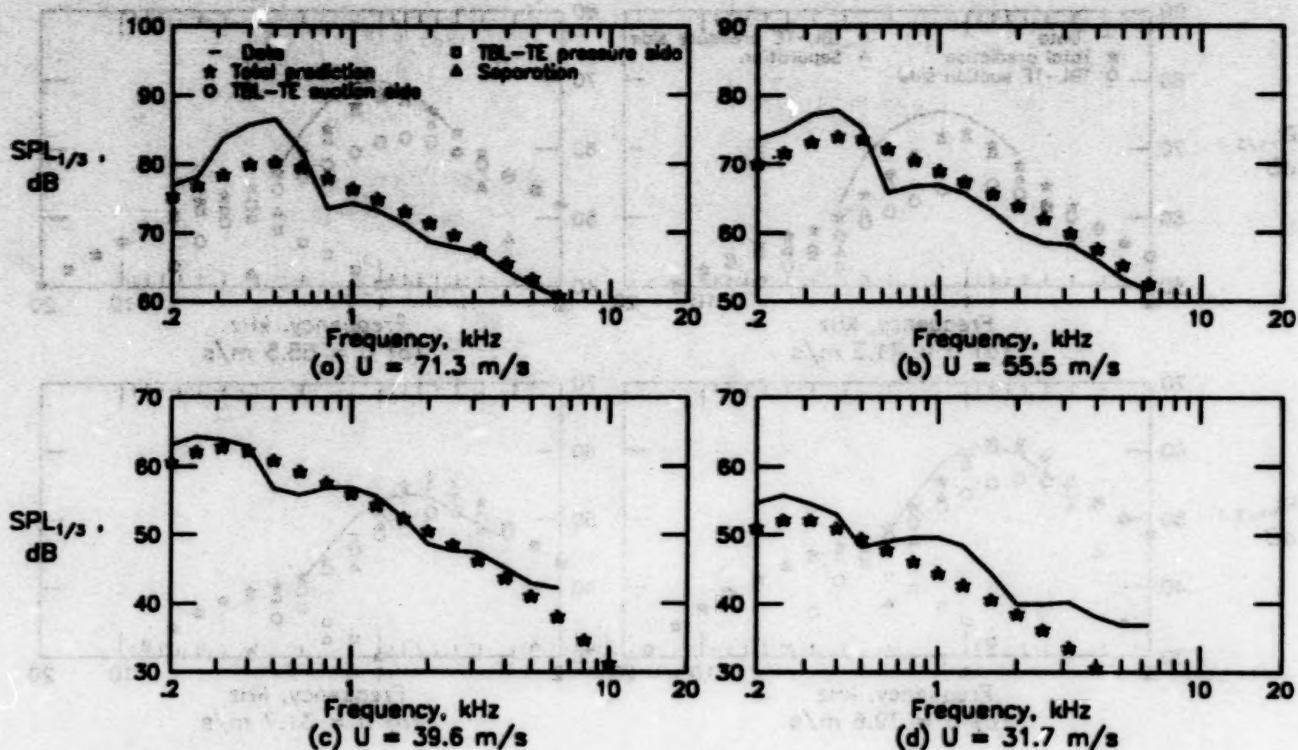


Figure 30. Self-noise spectra for 10.16-cm-chord airfoil with tripped BL at $\alpha_t = 19.8^\circ$ ($\alpha_o = 12.3^\circ$).

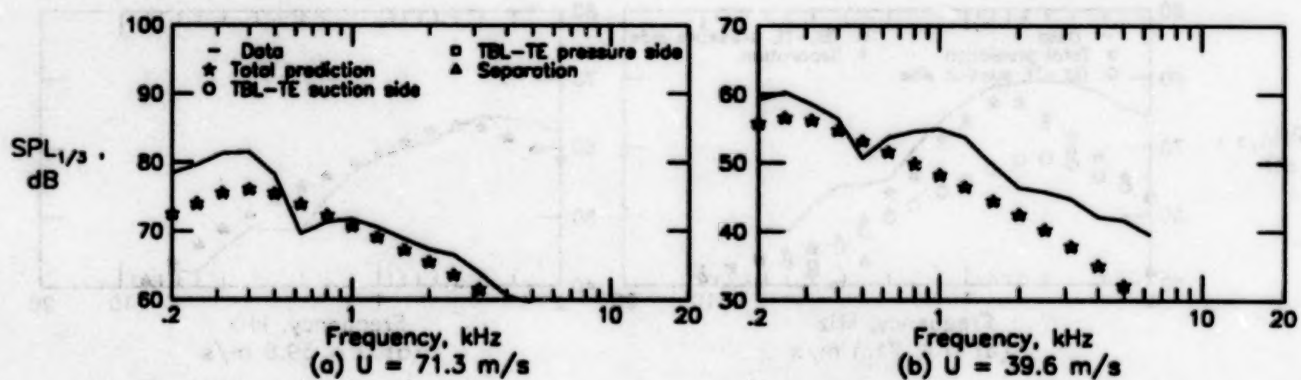


Figure 31. Self-noise spectra for 10.16-cm-chord airfoil with tripped BL at $\alpha_t = 25.2^\circ$ ($\alpha_o = 15.6^\circ$).

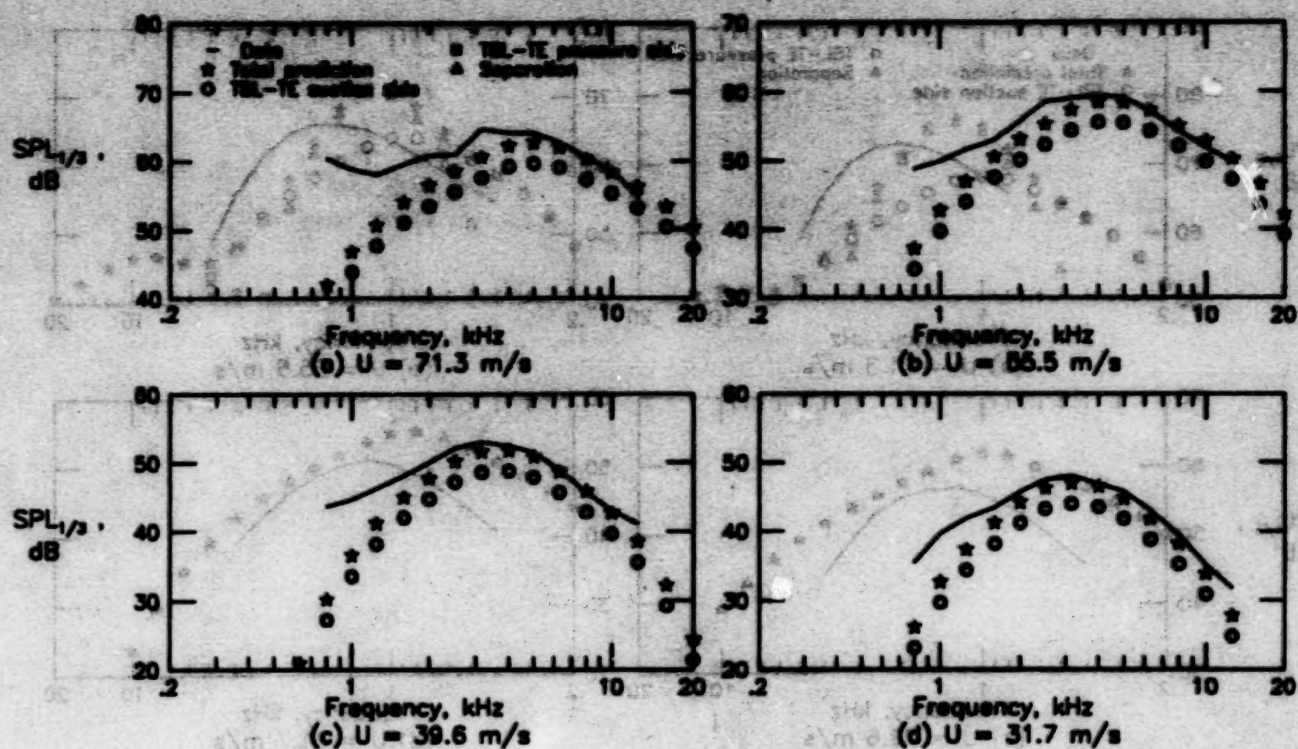


Figure 32. Self-noise spectra for 5.08-cm-chord airfoil with tripped BL at $\alpha_i = 0^\circ$ ($\alpha = 0^\circ$).

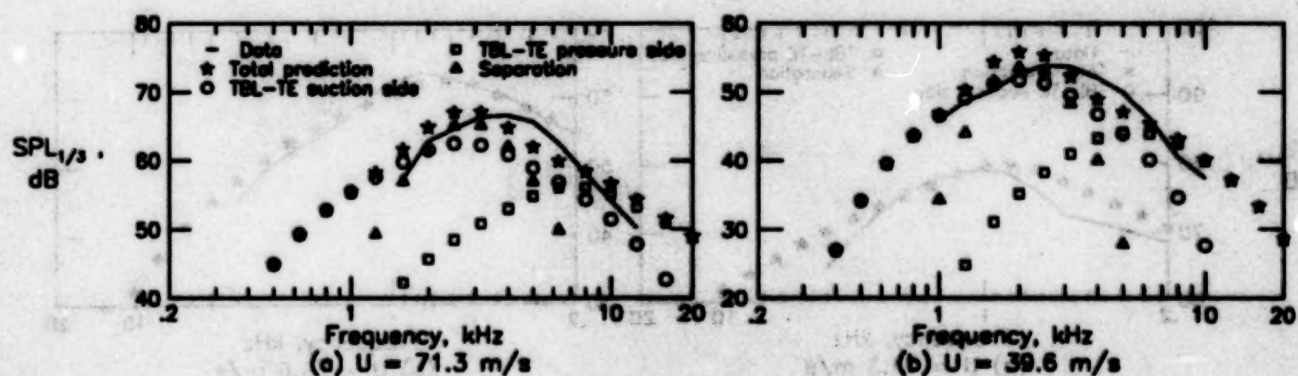


Figure 33. Self-noise spectra for 5.08-cm-chord airfoil with tripped BL at $\alpha_i = 5.4^\circ$ ($\alpha = 4.2^\circ$).

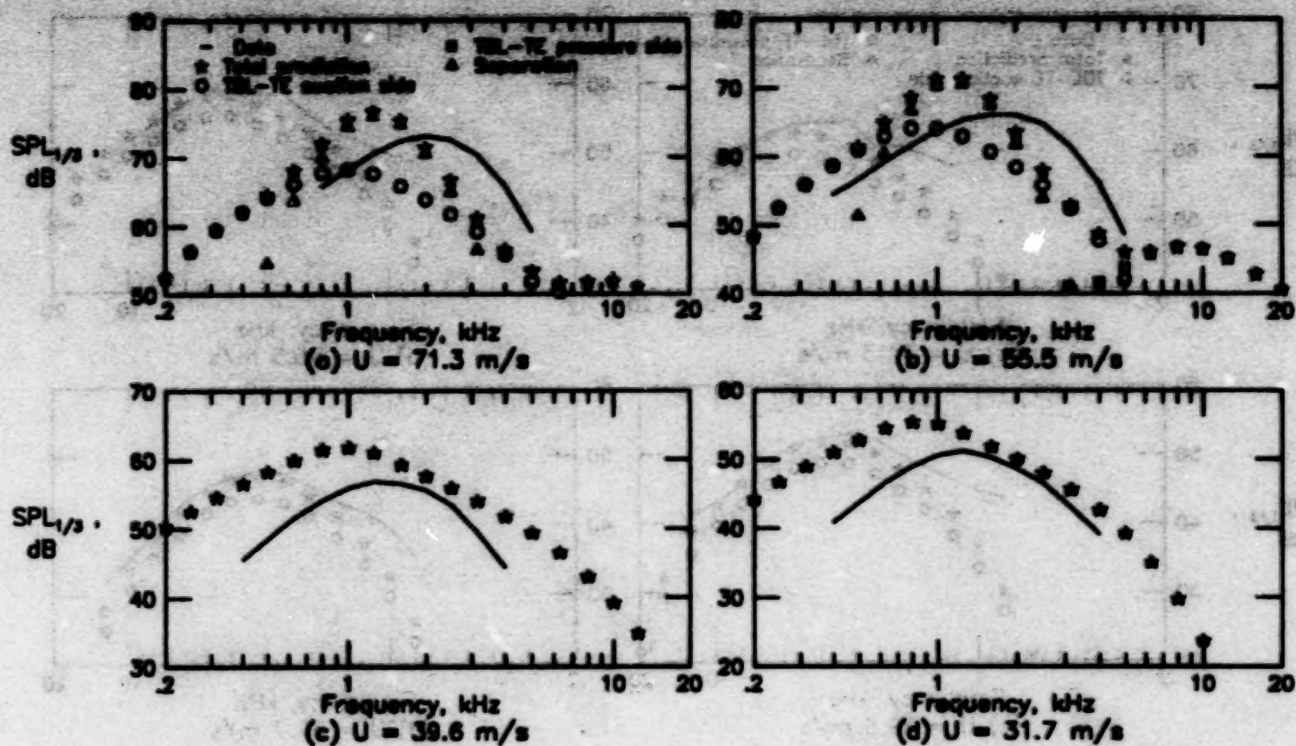


Figure 34. Self-noise spectra for 5.08-cm-chord airfoil with tripped BL at $\alpha_i = 10.8^\circ$ ($\alpha_s = 8.4^\circ$).

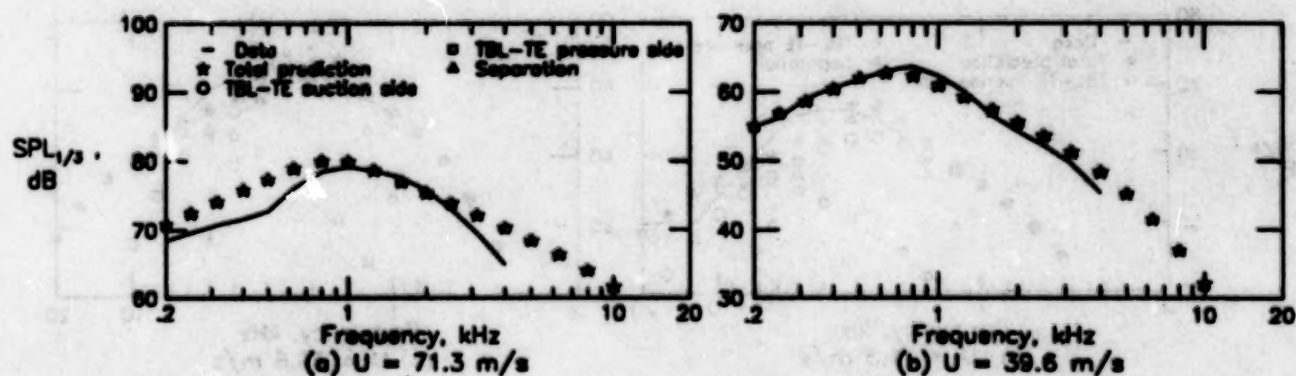


Figure 35. Self-noise spectra for 5.08-cm-chord airfoil with tripped BL at $\alpha_i = 14.4^\circ$ ($\alpha_s = 11.2^\circ$).

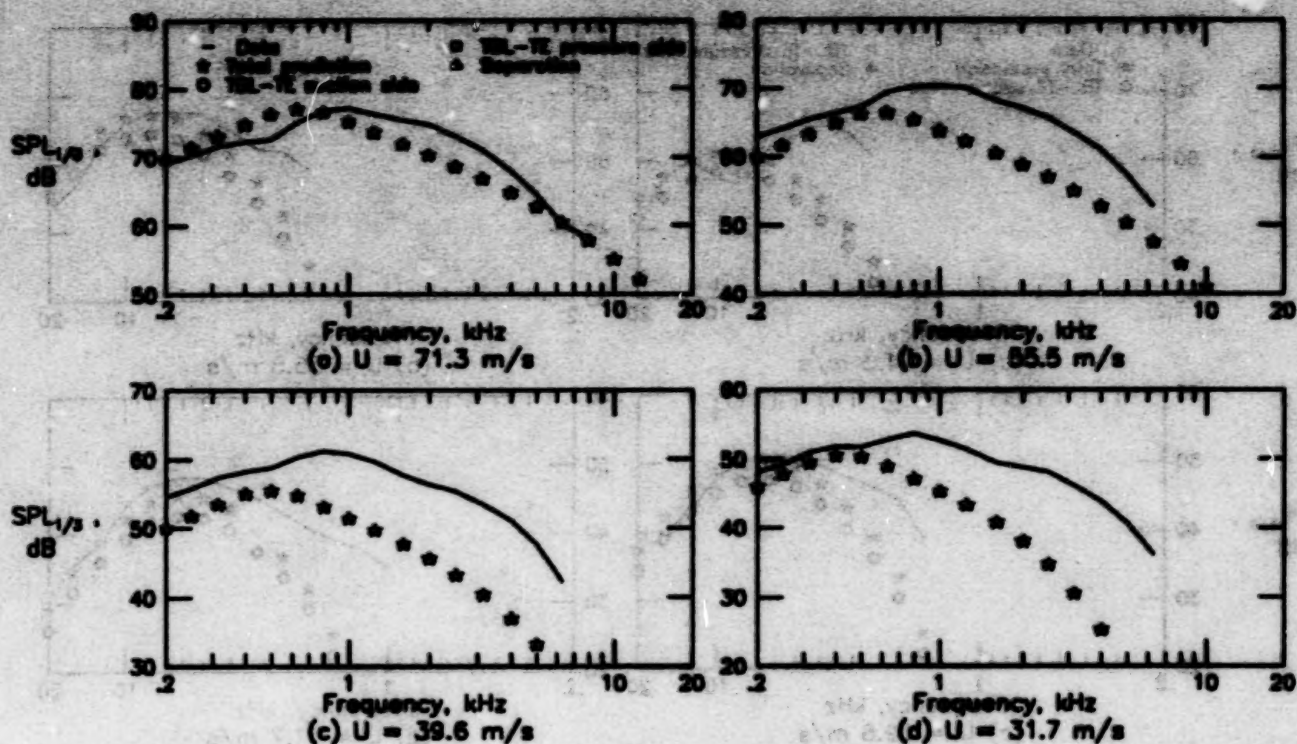


Figure 36. Self-noise spectra for 5.08-cm-chord airfoil with tripped BL at $\alpha_i = 19.8^\circ$ ($\alpha_o = 15.4^\circ$).

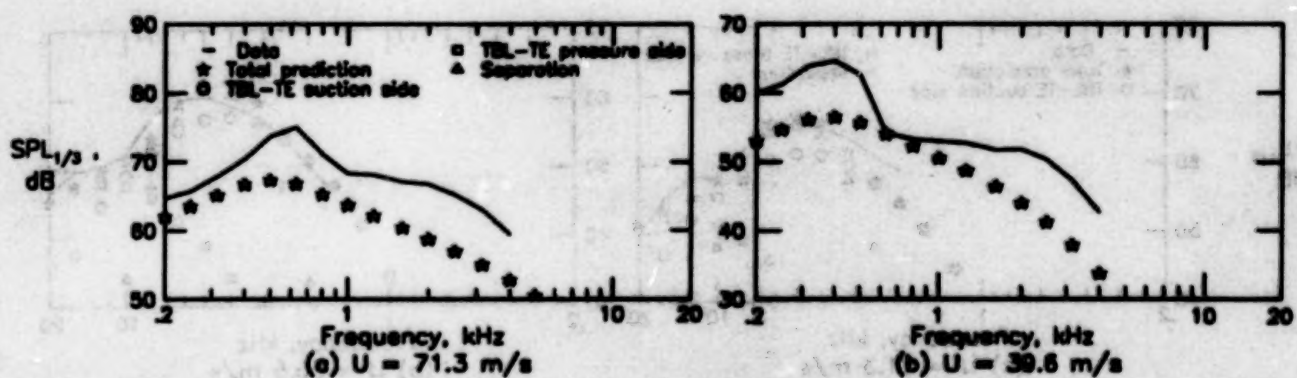


Figure 37. Self-noise spectra for 5.08-cm-chord airfoil with tripped BL at $\alpha_i = 25.2^\circ$ ($\alpha_o = 19.7^\circ$).

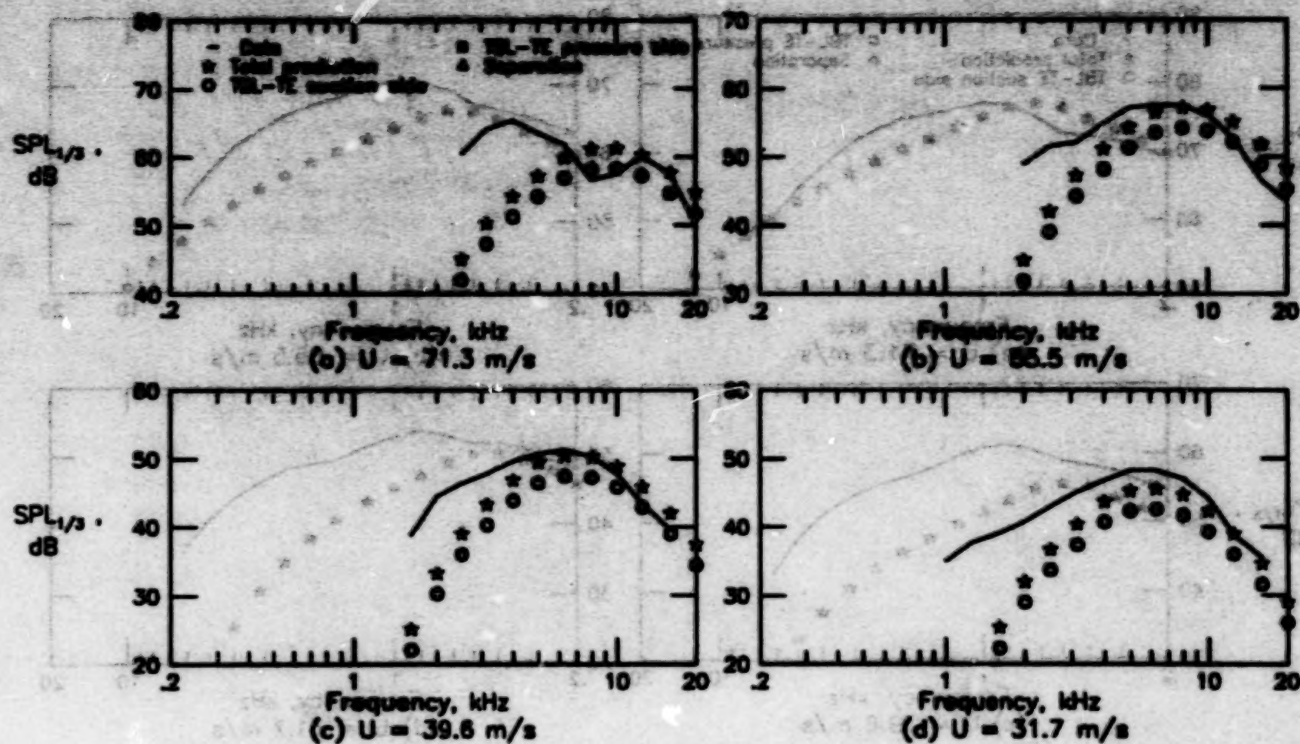


Figure 38. Self-noise spectra for 2.54-cm-chord airfoil with tripped BL at $\alpha_i = 0^\circ$ ($\alpha_s = 0^\circ$).

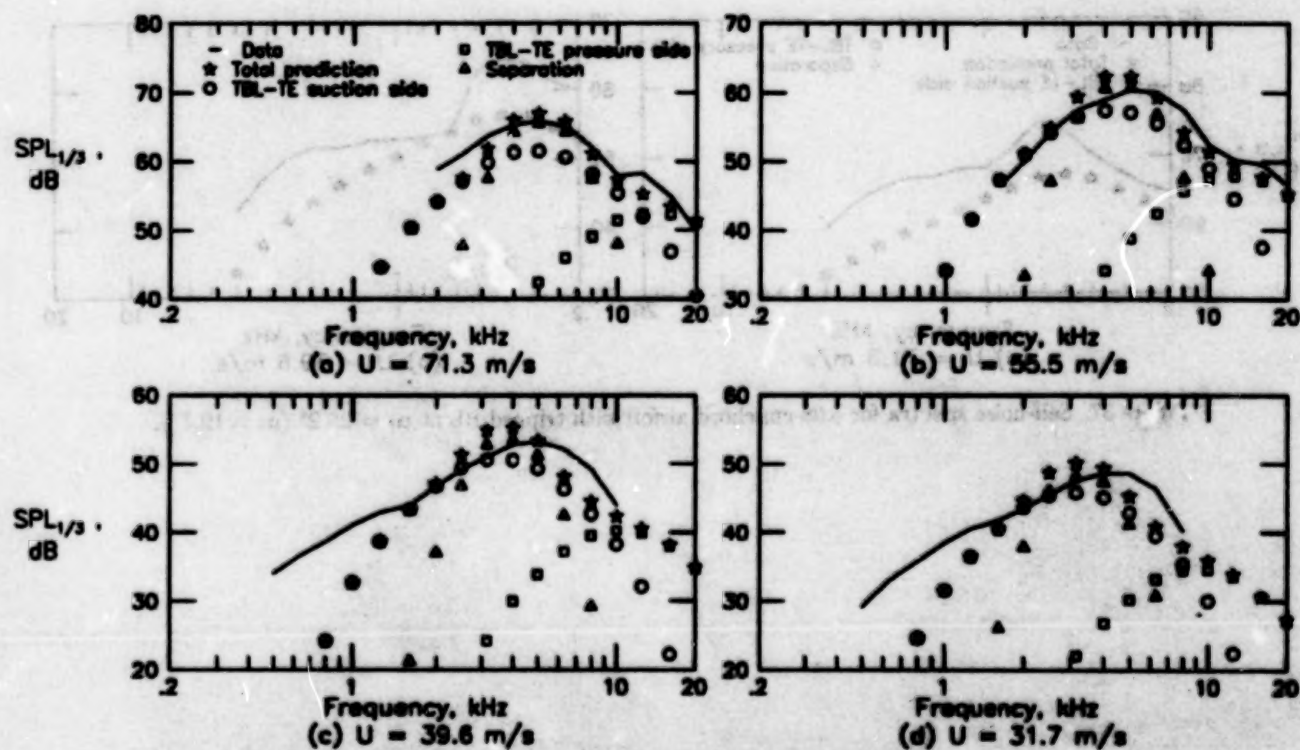


Figure 39. Self-noise spectra for 2.54-cm-chord airfoil with tripped BL at $\alpha_i = 5.4^\circ$ ($\alpha_s = 4.8^\circ$).

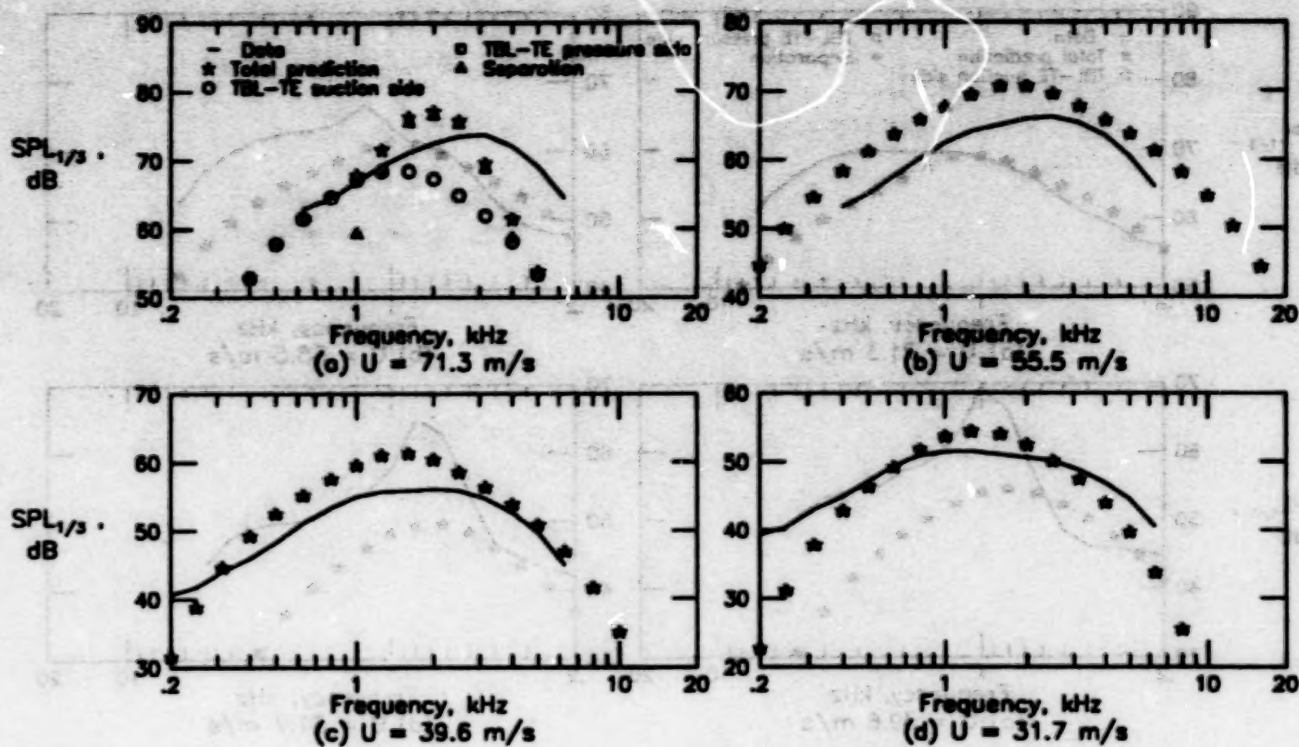


Figure 40. Self-noise spectra for 2.54-cm-chord airfoil with tripped BL at $\alpha_i = 10.8^\circ$ ($\alpha_s = 9.5^\circ$).

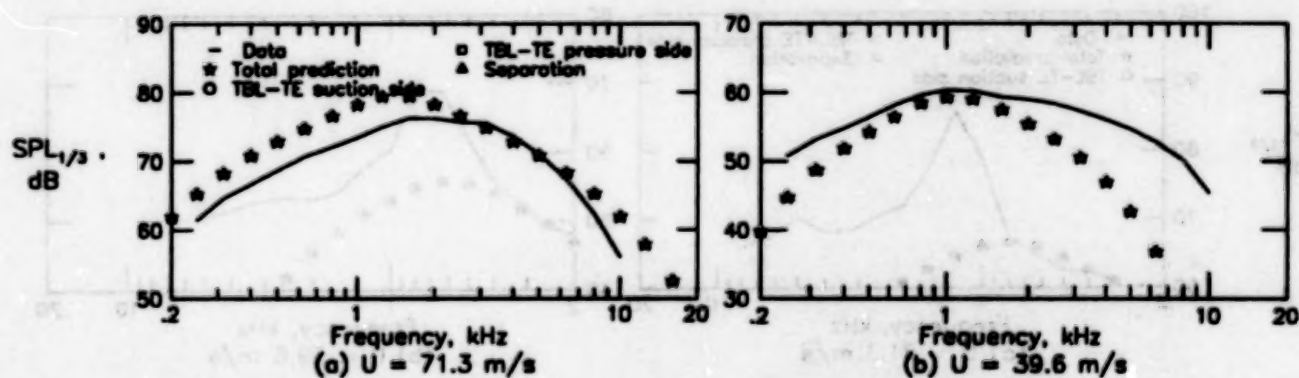


Figure 41. Self-noise spectra for 2.54-cm-chord airfoil with tripped BL at $\alpha_i = 14.4^\circ$ ($\alpha_s = 12.7^\circ$).

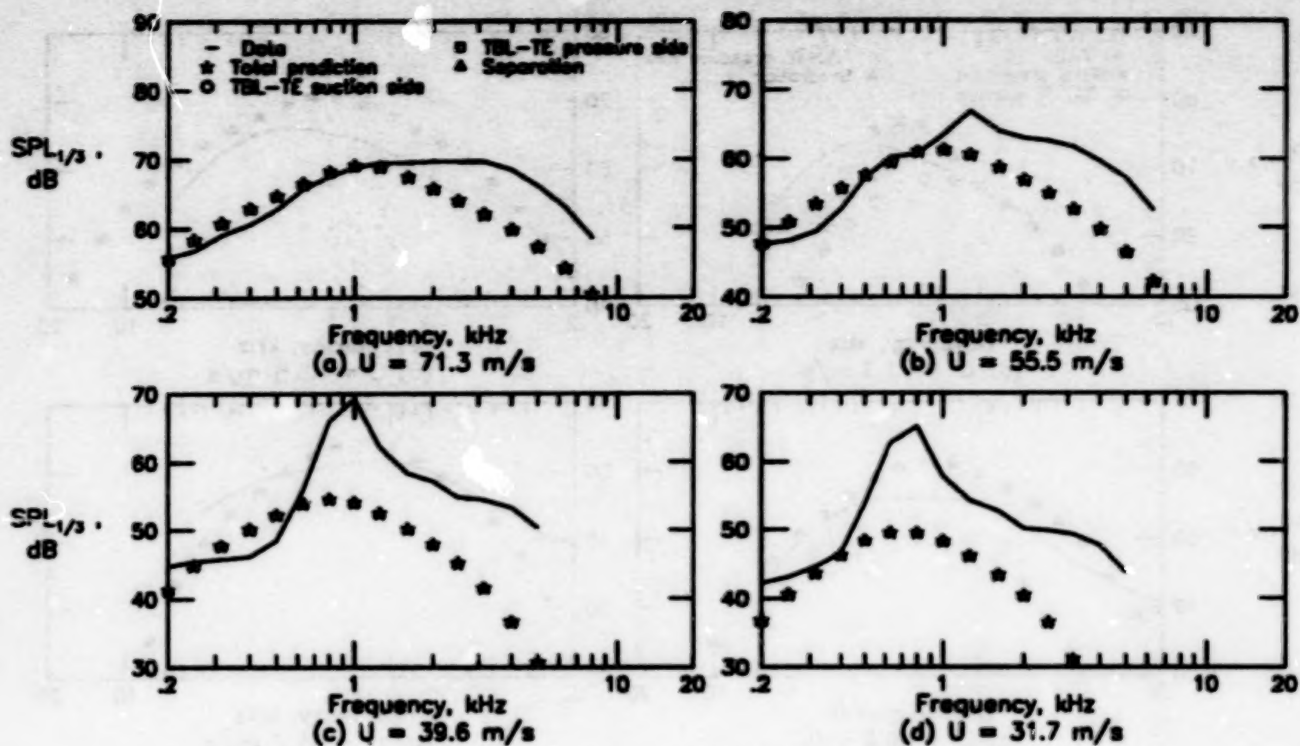


Figure 42. Self-noise spectra for 2.54-cm-chord airfoil with tripped BL at $\alpha_t = 19.8^\circ$ ($\alpha_s = 17.4^\circ$).

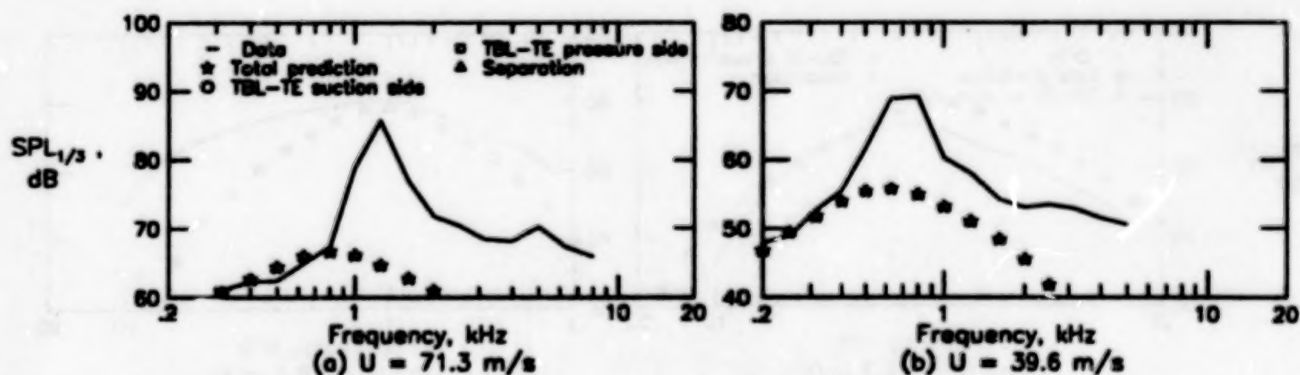


Figure 43. Self-noise spectra for 2.54-cm-chord airfoil with tripped BL at $\alpha_t = 25.2^\circ$ ($\alpha_s = 22.2^\circ$).

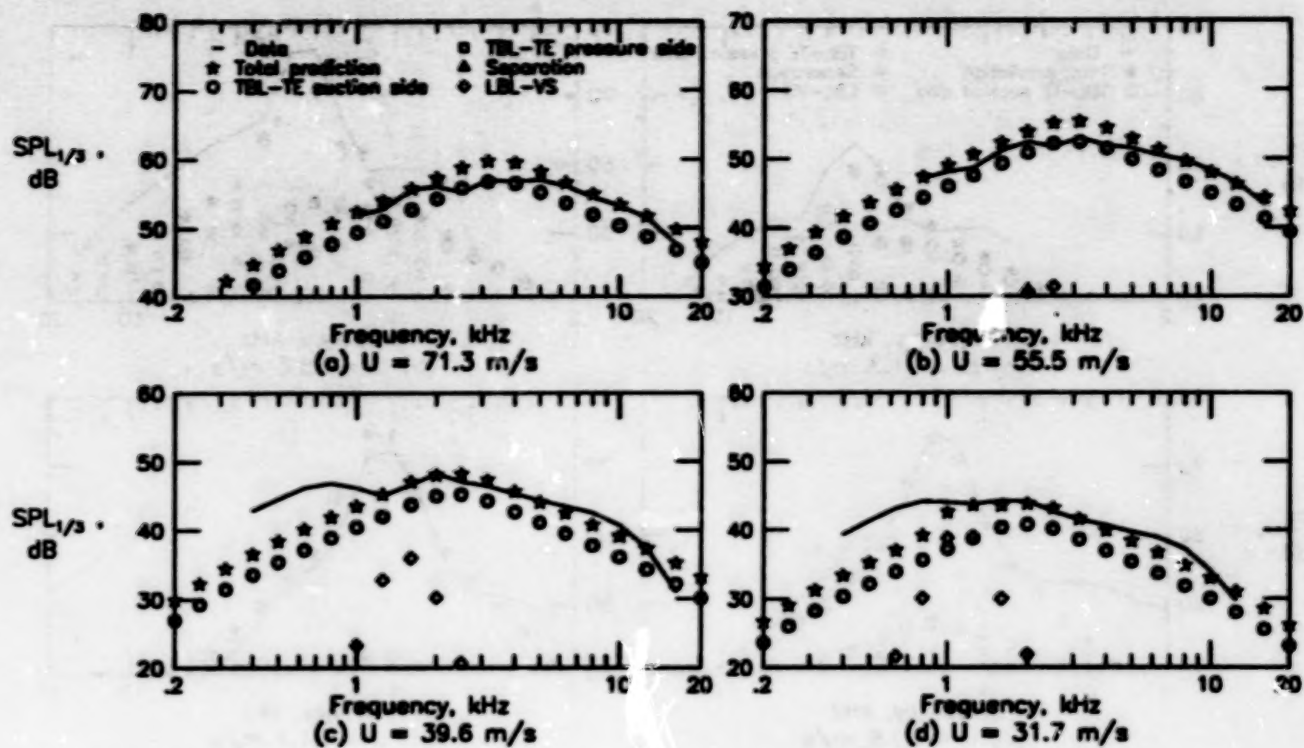


Figure 44. Self-noise spectra for 30.48-cm-chord airfoil with untripped BL (natural transition) at $\alpha_i = 0^\circ$ ($\alpha_s = 0^\circ$).

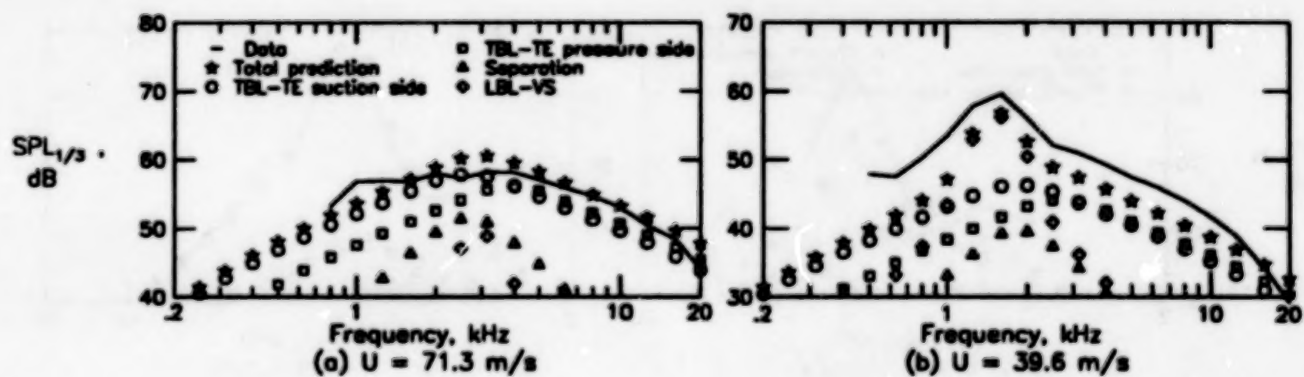


Figure 45. Self-noise spectra for 30.48-cm-chord airfoil with untripped BL at $\alpha_i = 5.4^\circ$ ($\alpha_s = 1.5^\circ$).

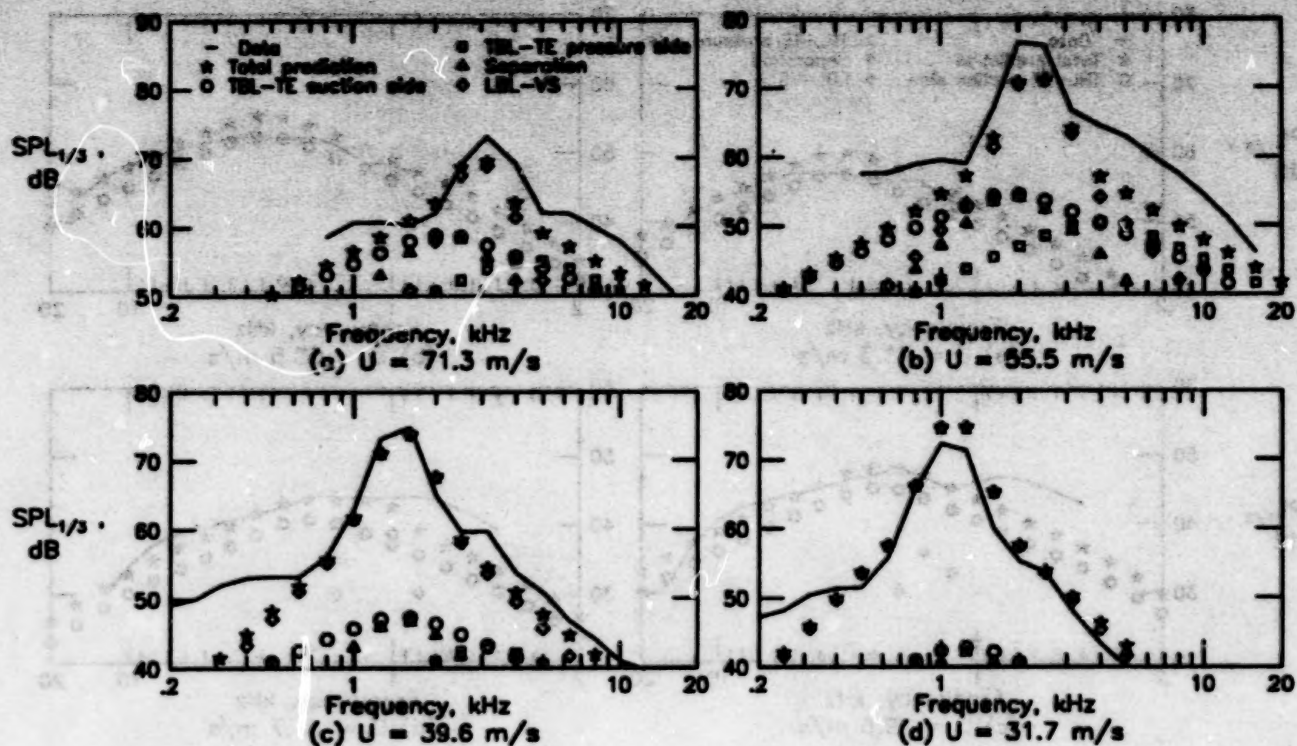


Figure 46. Self-noise spectra for 30.48-cm-chord airfoil with untripped BL at $\alpha_t = 10.8^\circ$ ($\alpha_s = 3.0^\circ$).

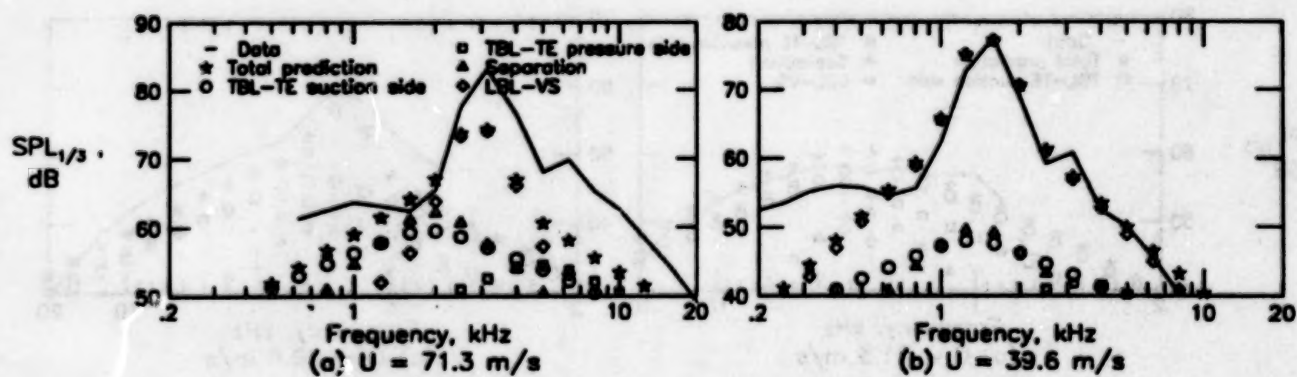


Figure 47. Self-noise spectra for 30.48-cm-chord airfoil with untripped BL at $\alpha_t = 14.4^\circ$ ($\alpha_s = 4.0^\circ$).

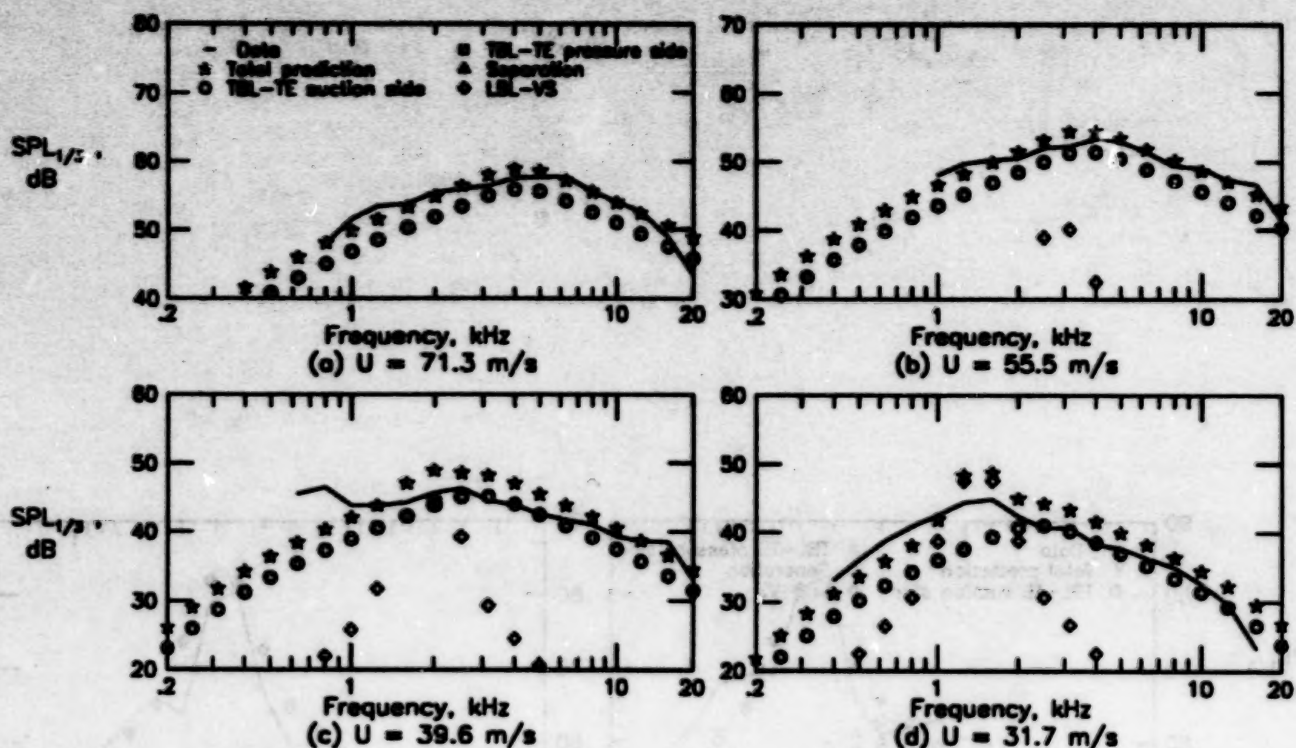


Figure 48. Self-noise spectra for 22.86-cm-chord airfoil with untripped BL at $\alpha_i = 0^\circ$ ($\alpha_s = 0^\circ$).

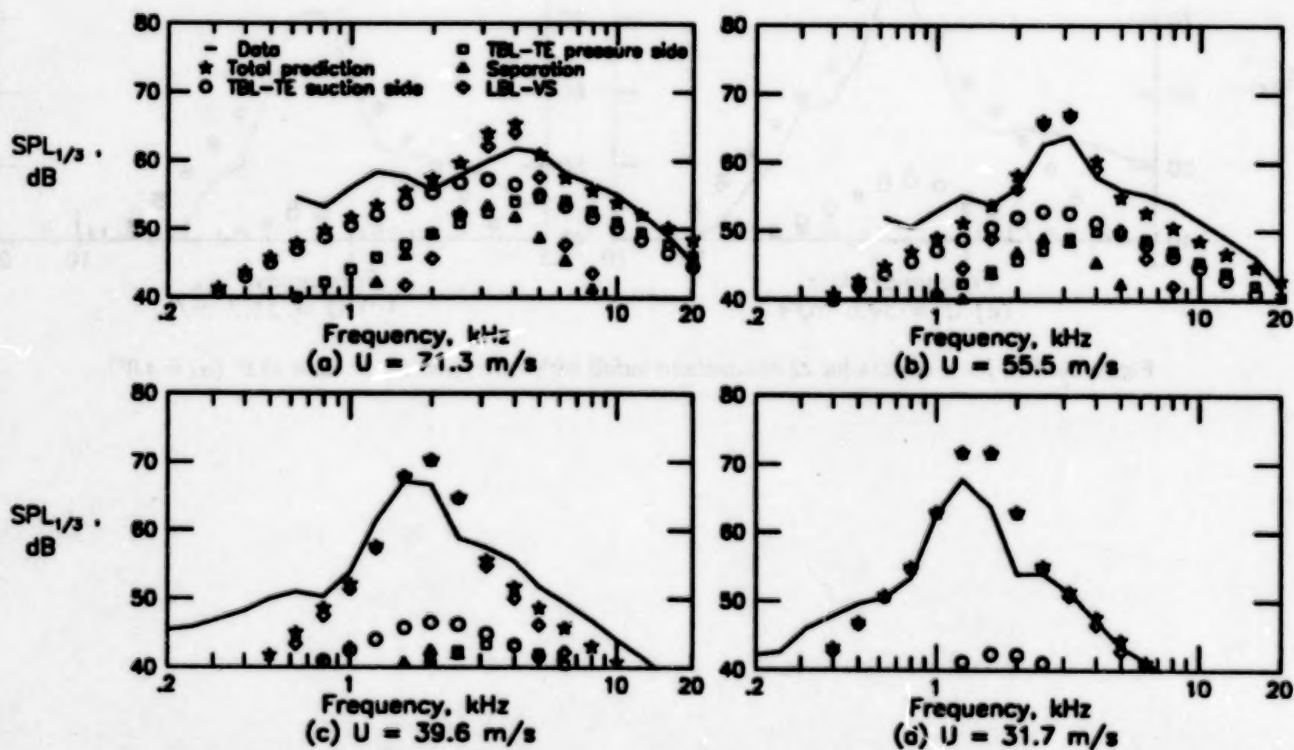


Figure 49. Self-noise spectra for 22.86-cm-chord airfoil with untripped BL at $\alpha_i = 5.4^\circ$ ($\alpha_s = 2.0^\circ$).

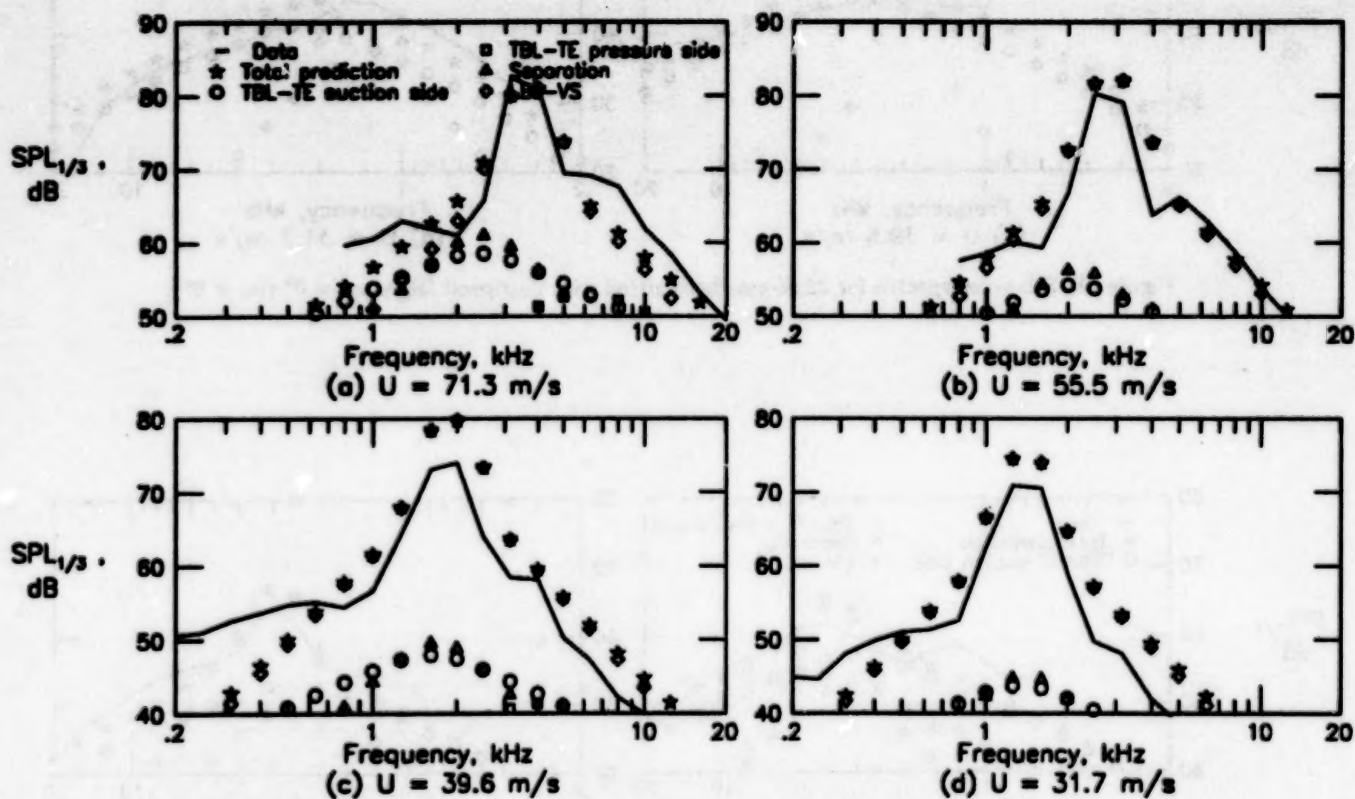


Figure 50. Self-noise spectra for 22.86-cm-chord airfoil with untripped BL at $\alpha_i = 10.8^\circ$ ($\alpha_o = 4.0^\circ$).

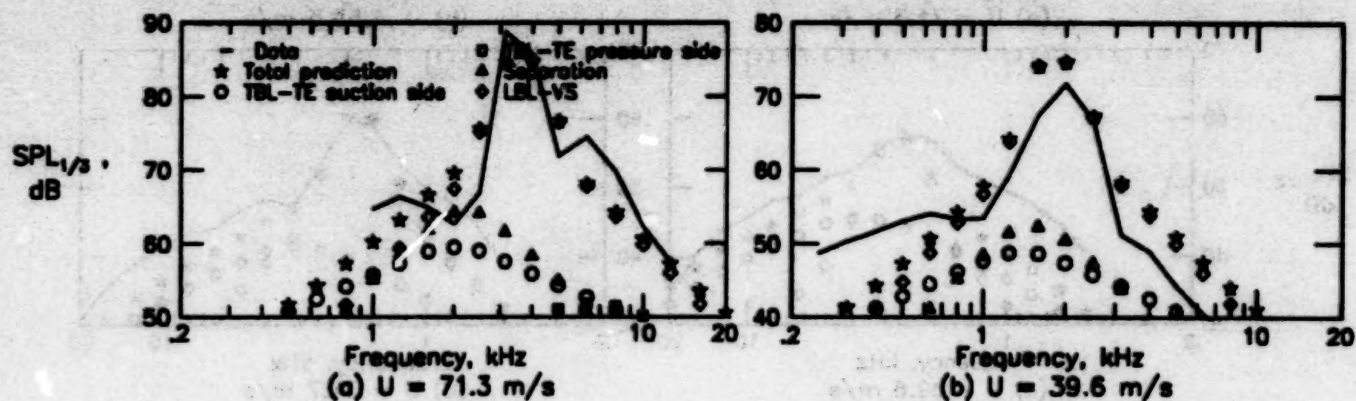


Figure 51. Self-noise spectra for 22.86-cm-chord airfoil with untripped BL at $\alpha_i = 14.4^\circ$ ($\alpha_s = 5.3^\circ$).

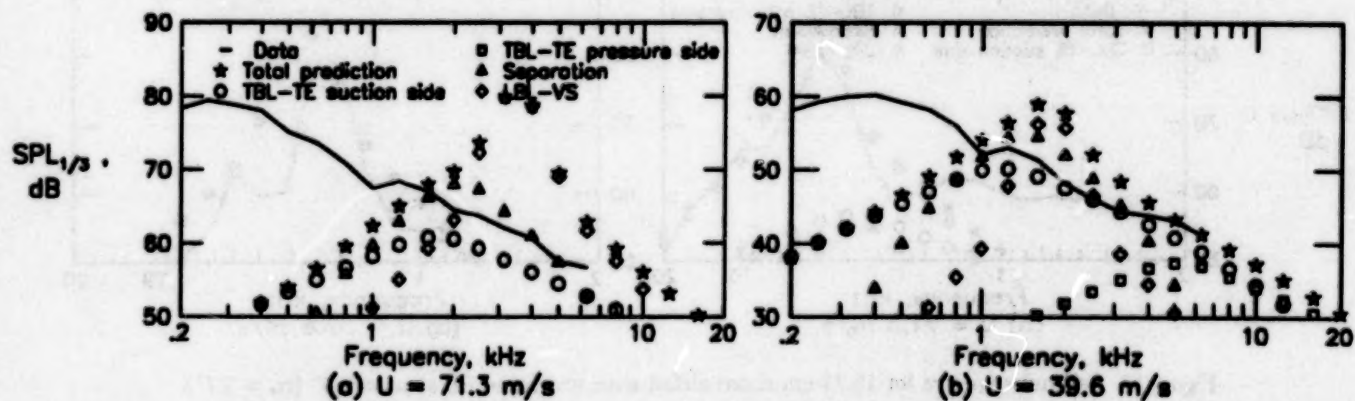


Figure 52. Self-noise spectra for 22.86-cm-chord airfoil with untripped BL at $\alpha_i = 19.8^\circ$ ($\alpha_s = 7.3^\circ$).

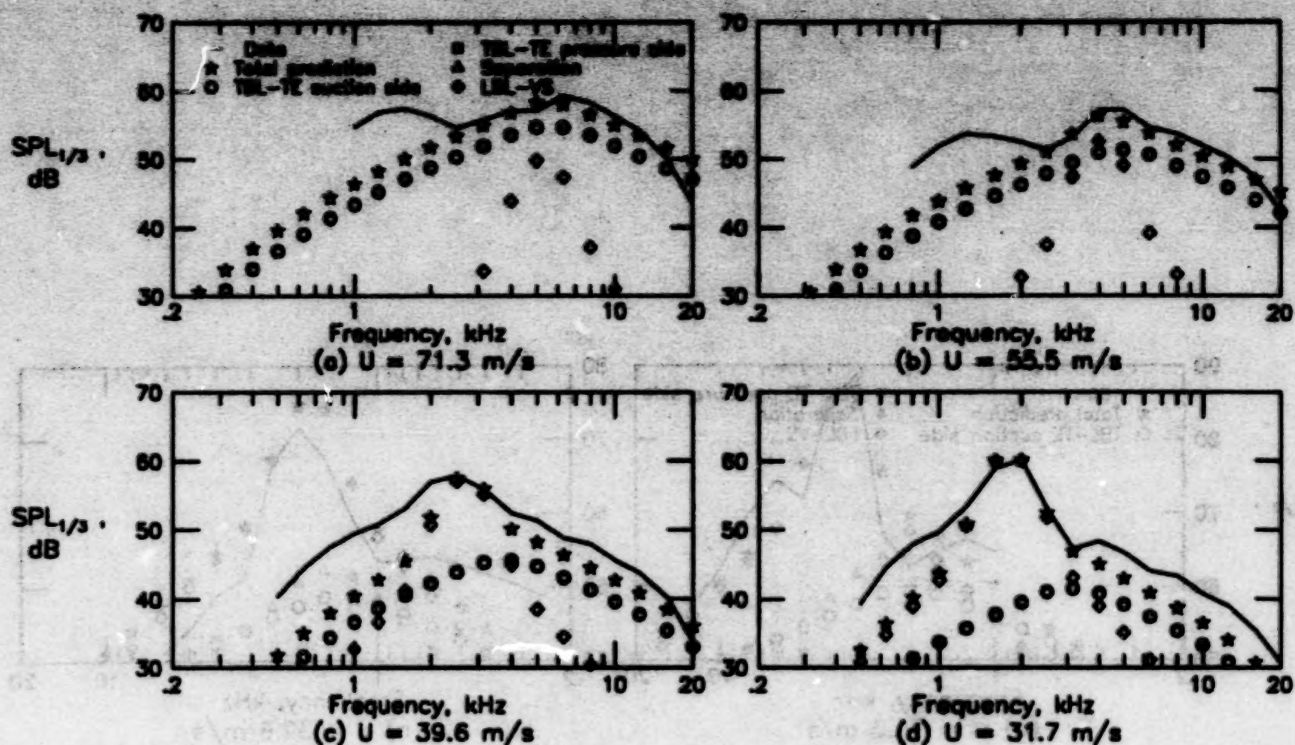


Figure 53. Self-noise spectra for 15.24-cm-chord airfoil with untripped BL at $\alpha_i = 0^\circ$ ($\alpha_s = 0^\circ$).

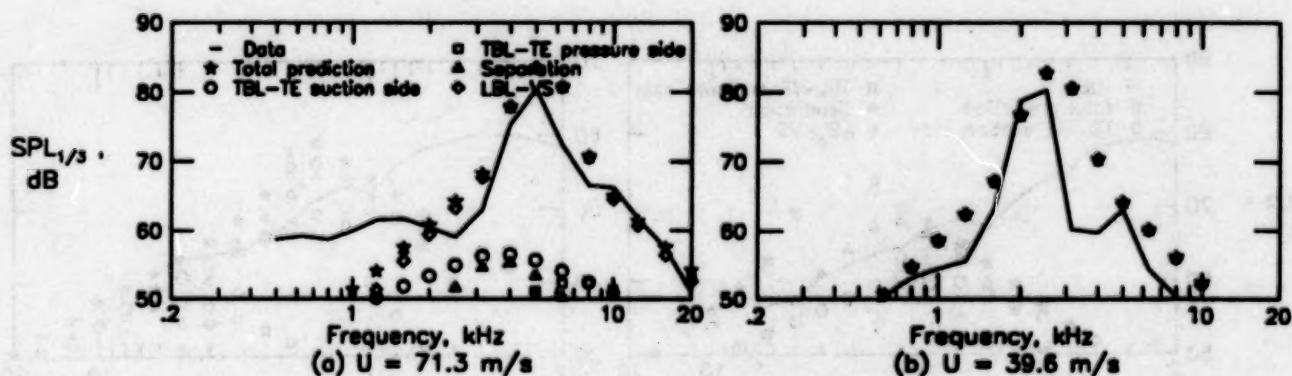


Figure 54. Self-noise spectra for 15.24-cm-chord airfoil with untripped BL at $\alpha_i = 5.4^\circ$ ($\alpha_s = 2.7^\circ$).

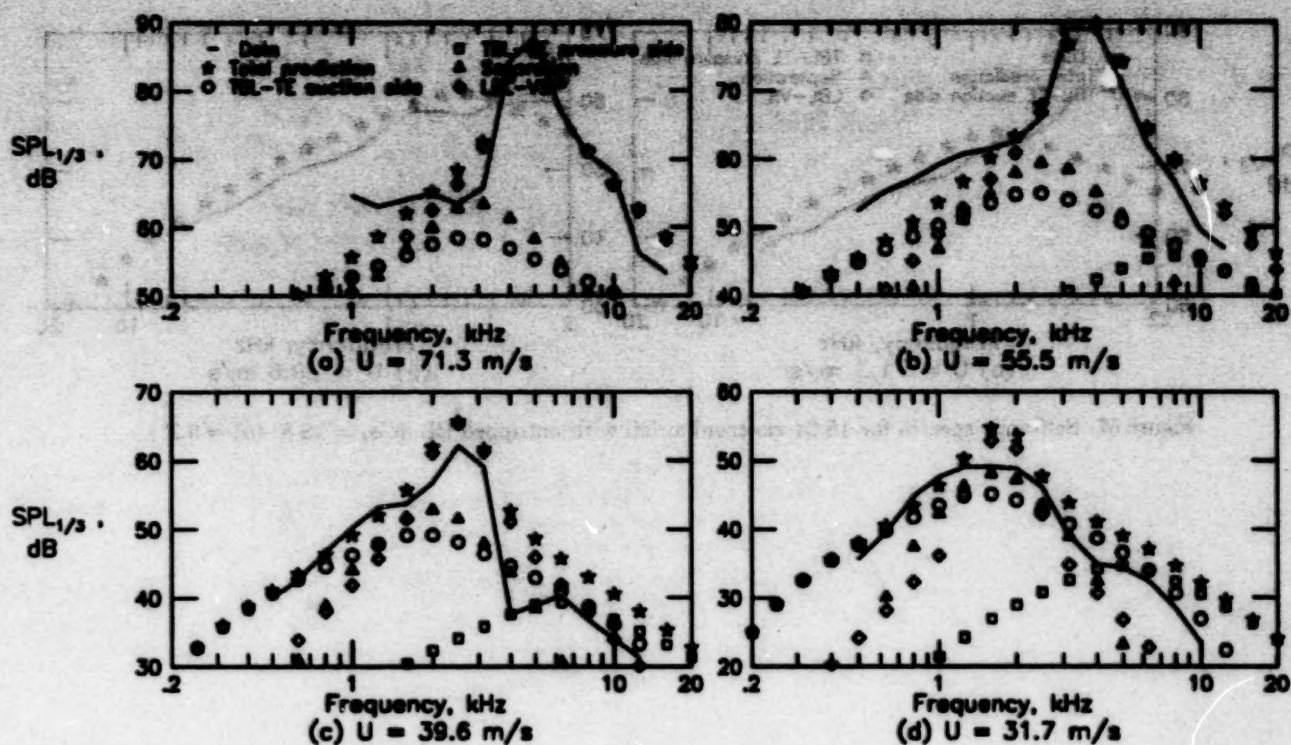


Figure 55. Self-noise spectra for 15.24-cm-chord airfoil with untripped BL at $\alpha_i = 10.8^\circ$ ($\alpha_s = 5.4^\circ$).

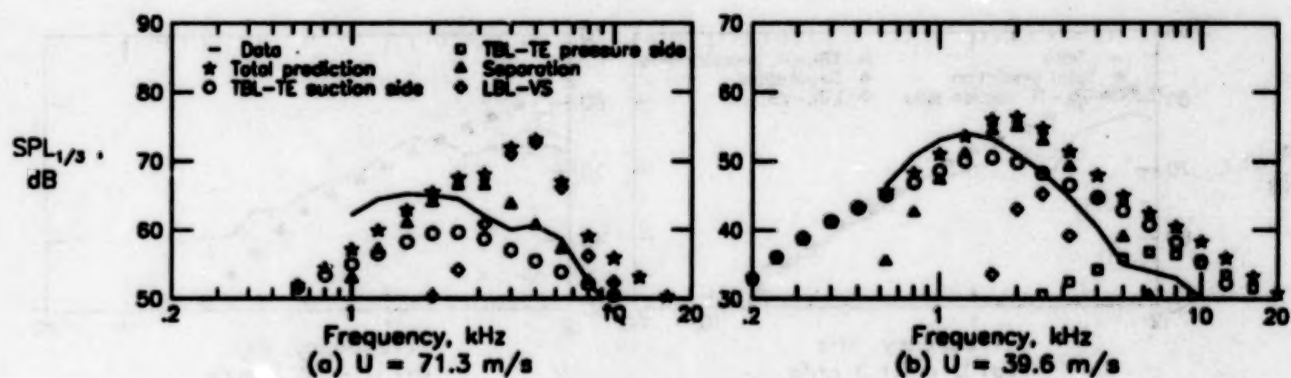


Figure 56. Self-noise spectra for 15.24-cm-chord airfoil with untripped BL at $\alpha_i = 14.4^\circ$ ($\alpha_s = 7.2^\circ$).

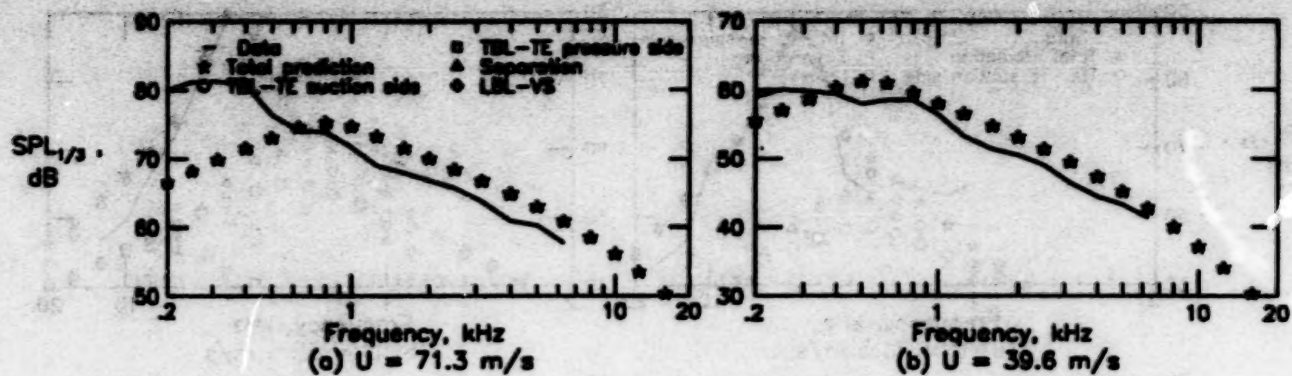


Figure 57. Self-noise spectra for 15.24-cm-chord airfoil with untripped BL at $\alpha_t = 19.8^\circ$ ($\alpha_s = 9.9^\circ$).

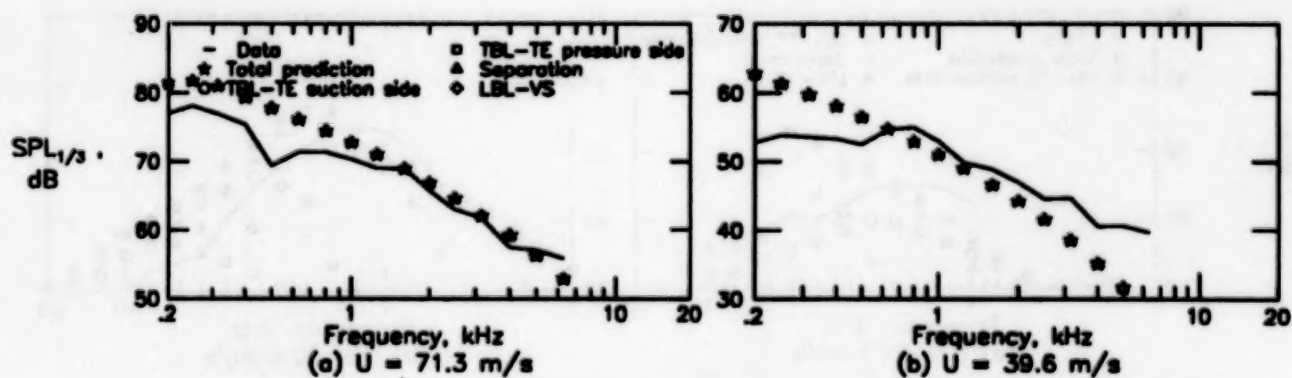


Figure 58. Self-noise spectra for 15.24-cm-chord airfoil with untripped BL at $\alpha_t = 25.2^\circ$ ($\alpha_s = 12.6^\circ$).

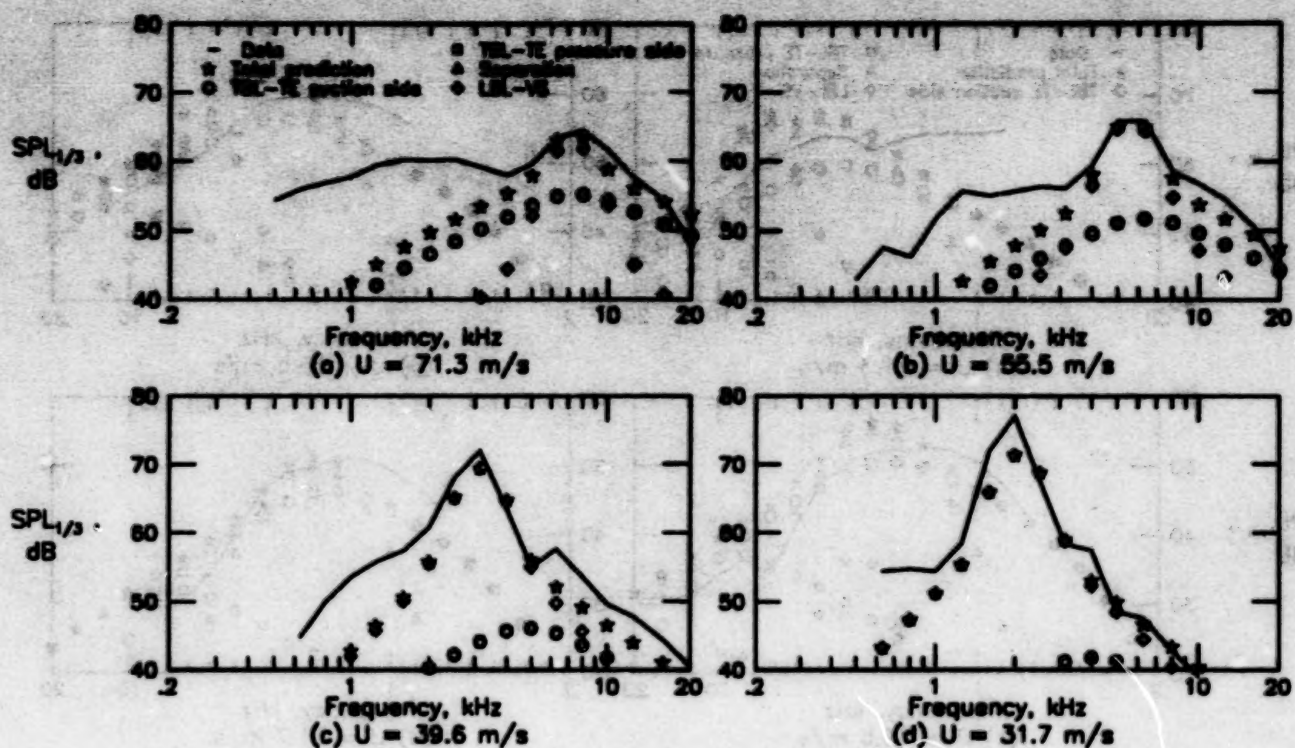


Figure 59. Self-noise spectra for 10.16-cm-chord airfoil with untripped BL at $\alpha_i = 0^\circ$ ($\alpha_s = 0^\circ$).

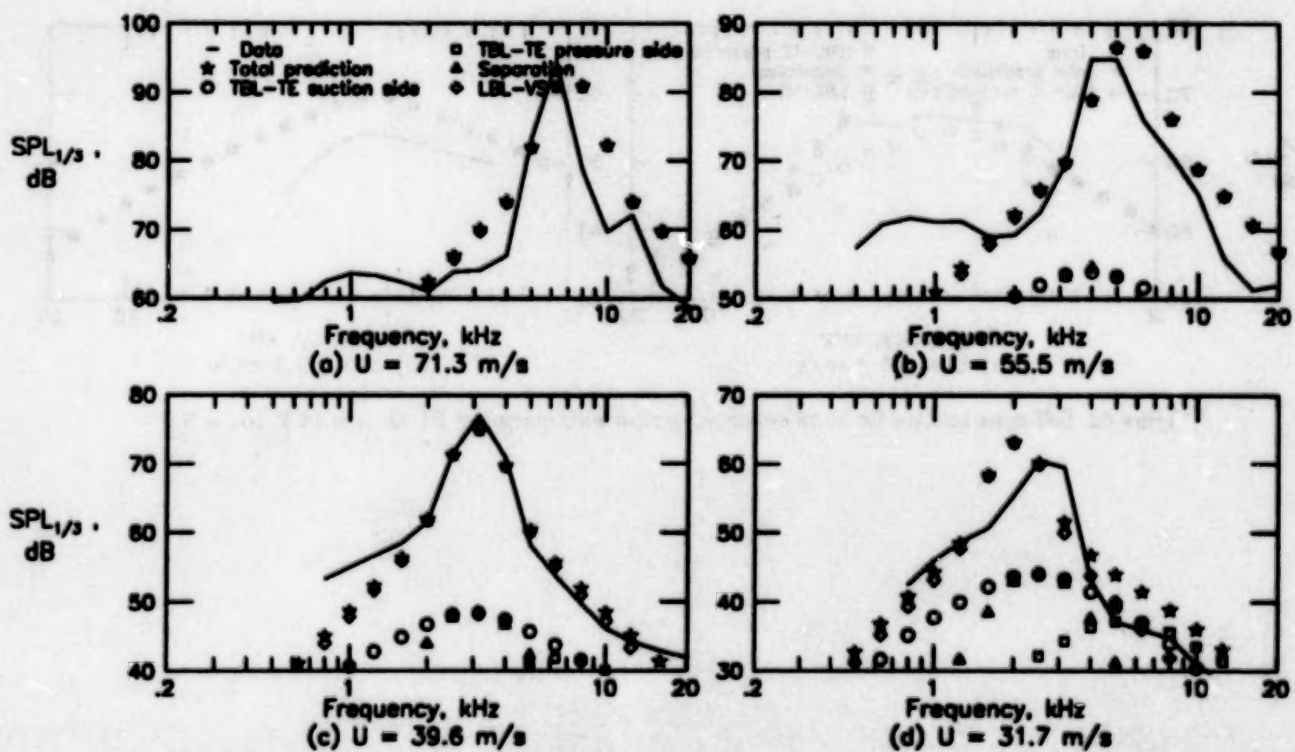


Figure 60. Self-noise spectra for 10.16-cm-chord airfoil with untripped BL at $\alpha_i = 5.4^\circ$ ($\alpha_s = 3.3^\circ$).

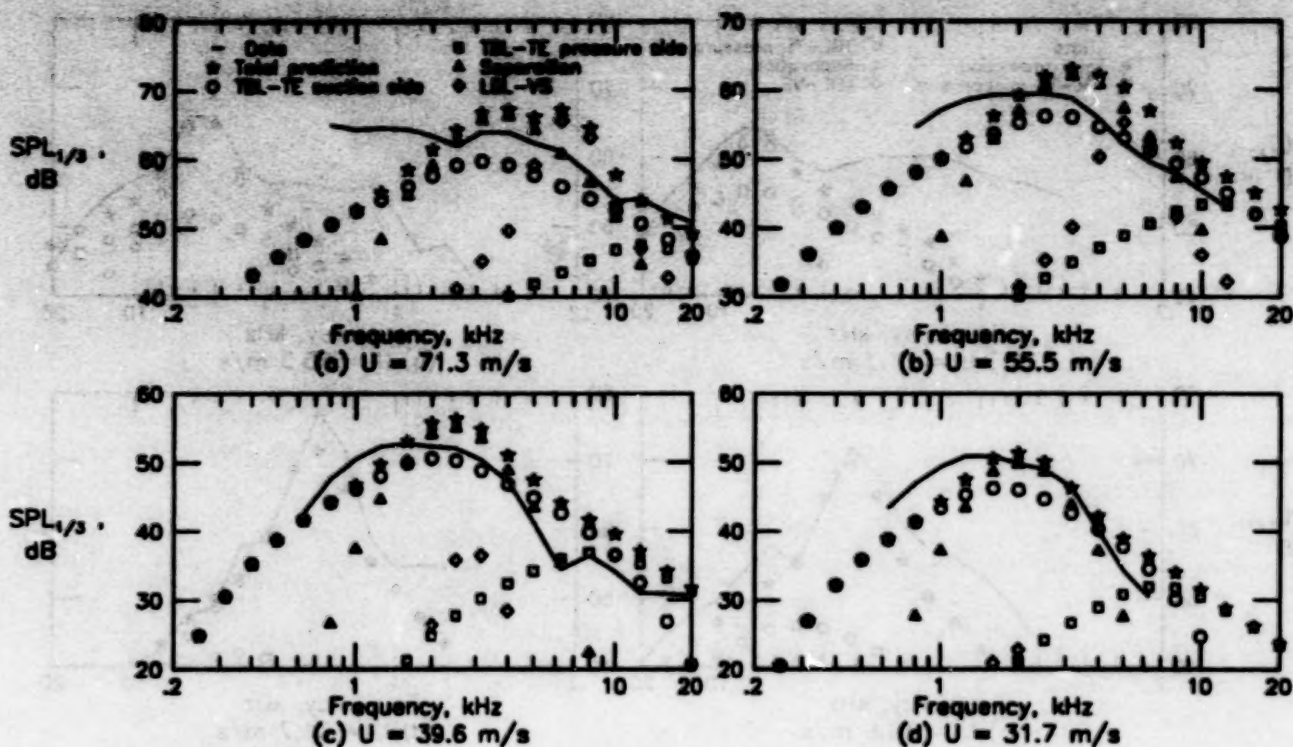


Figure 61. Self-noise spectra for 10.16-cm-chord airfoil with untripped BL at $\alpha_t = 10.8^\circ$ ($\alpha = 6.7^\circ$).

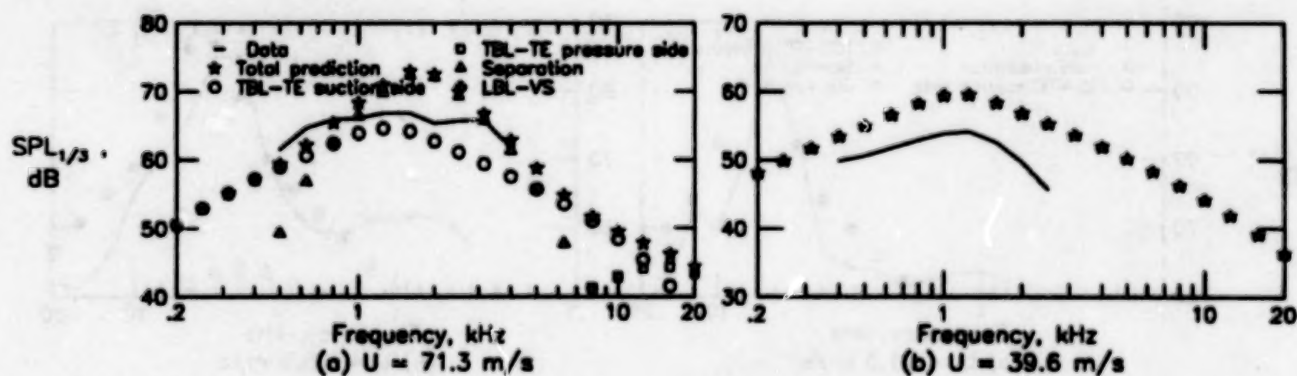


Figure 62. Self-noise spectra for 10.16-cm-chord airfoil with untripped BL at $\alpha_t = 14.4^\circ$ ($\alpha = 8.9^\circ$).

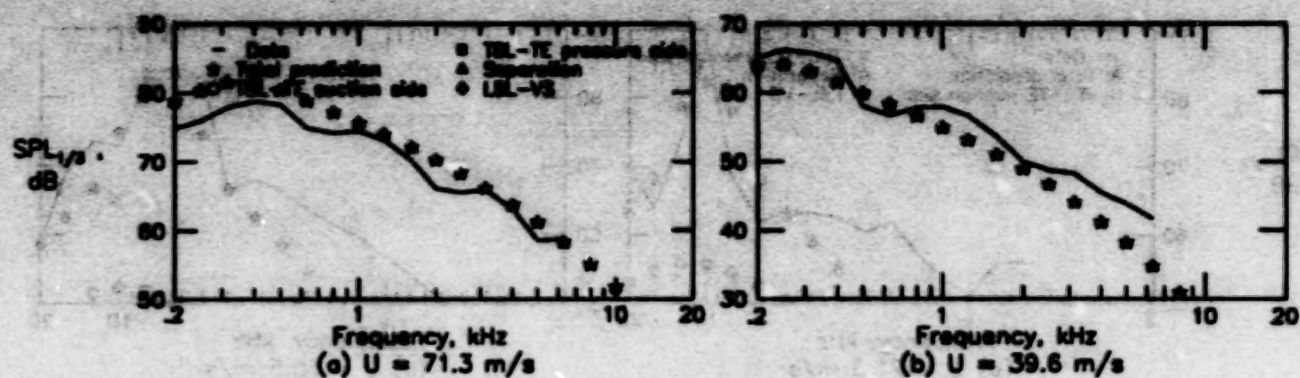


Figure 63. Self-noise spectra for 10.16-cm-chord airfoil with untripped BL at $\alpha_t = 19.8^\circ$ ($\alpha_o = 12.3^\circ$).

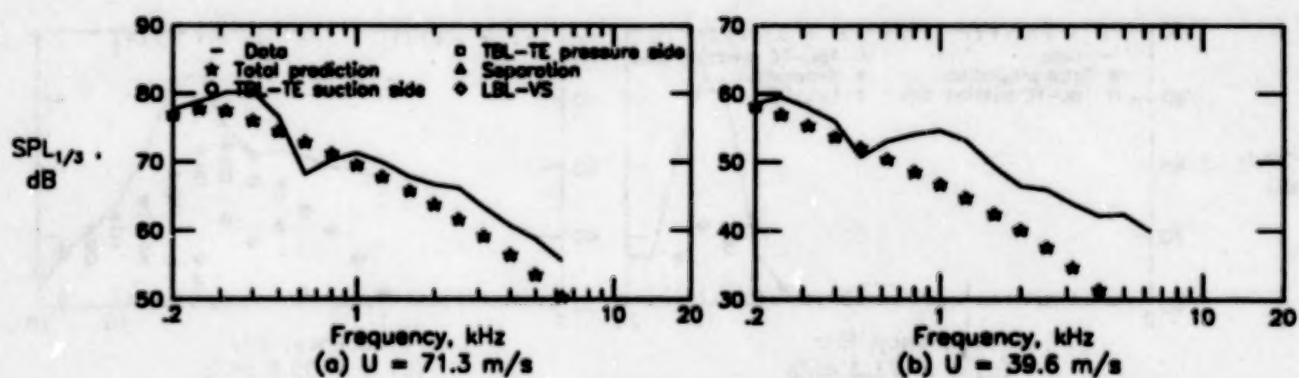


Figure 64. Self-noise spectra for 10.16-cm-chord airfoil with untripped BL at $\alpha_t = 25.2^\circ$ ($\alpha_o = 15.6^\circ$).

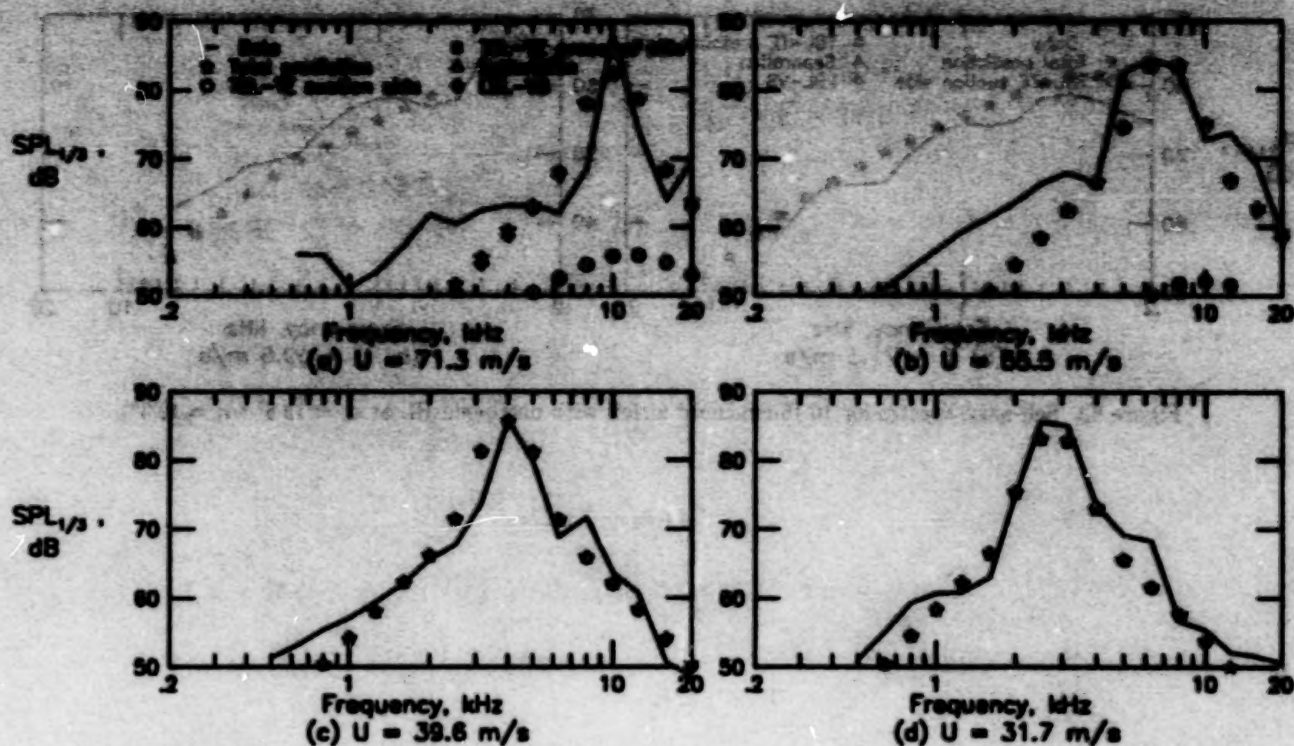


Figure 65. Self-noise spectra for 5.08-cm-chord airfoil with untripped BL at $\alpha_i = 0^\circ$ ($\alpha_o = 0^\circ$).

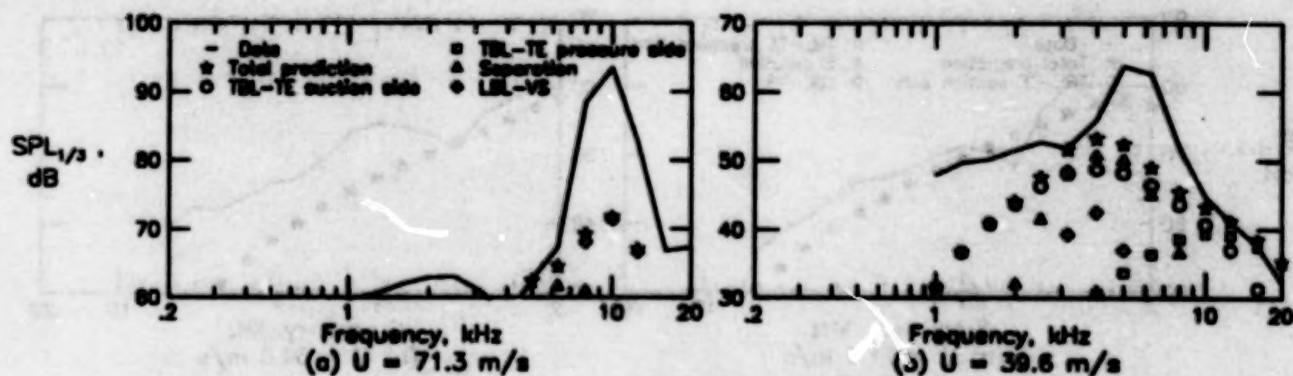


Figure 66. Self-noise spectra for 5.08-cm-chord airfoil with untripped BL at $\alpha_i = 5.4^\circ$ ($\alpha_o = 4.2^\circ$).

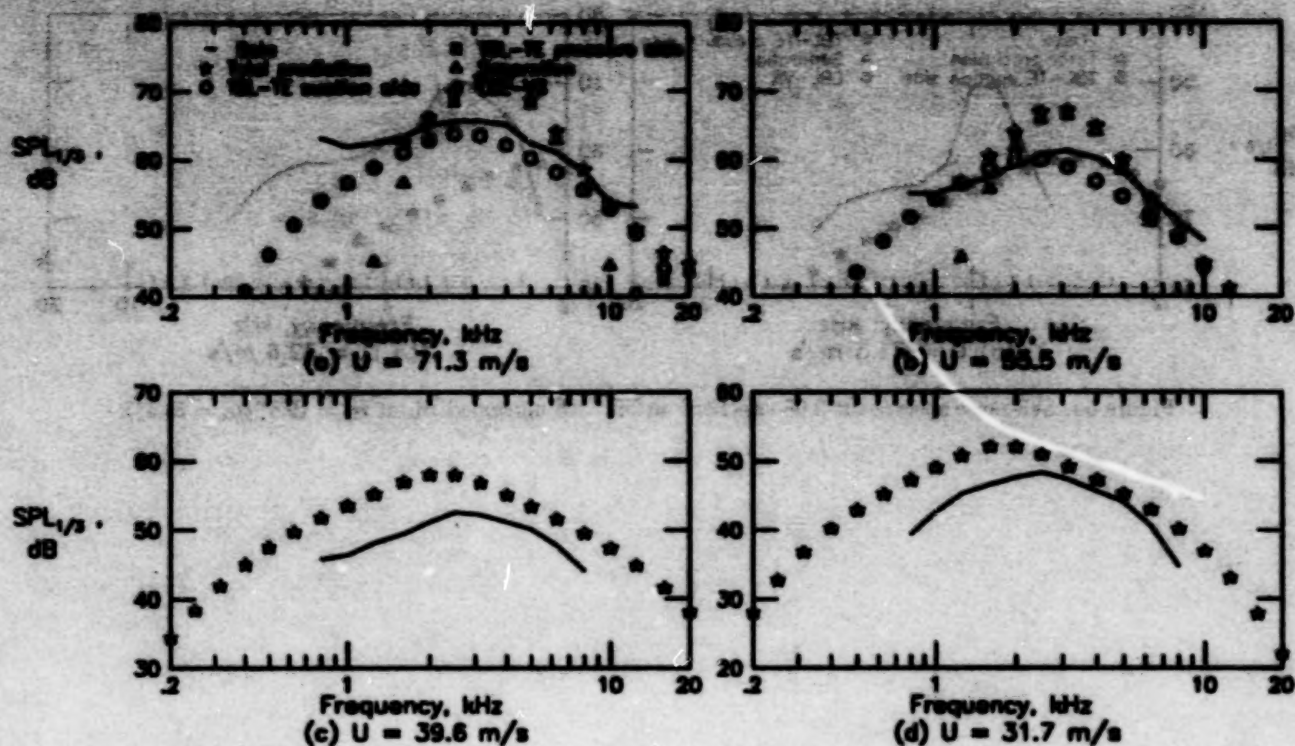


Figure 67. Self-noise spectra for 5.08-cm-chord airfoil with untripped BL at $\alpha_i = 10.6^\circ$ ($\alpha_s = 8.4^\circ$).

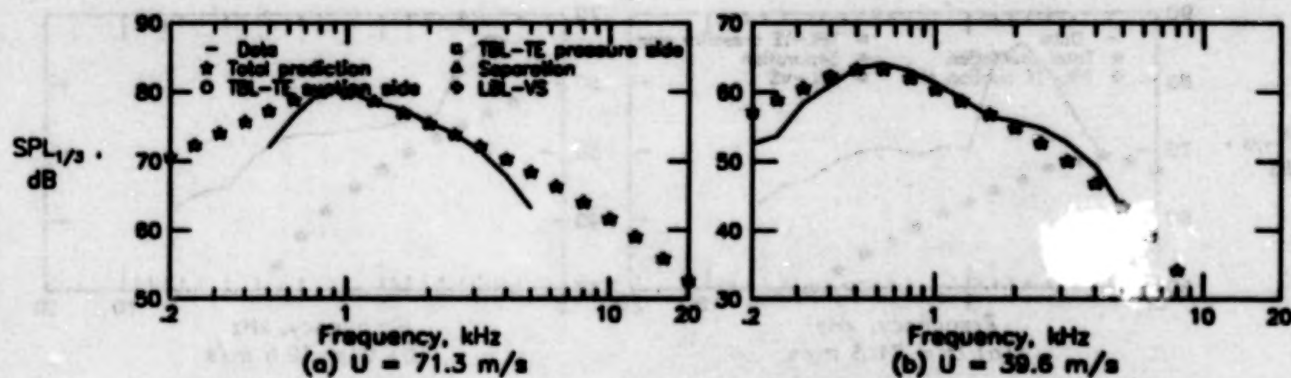


Figure 68. Self-noise spectra for 5.08-cm-chord airfoil with untripped BL at $\alpha_i = 14.4^\circ$ ($\alpha_s = 11.2^\circ$).

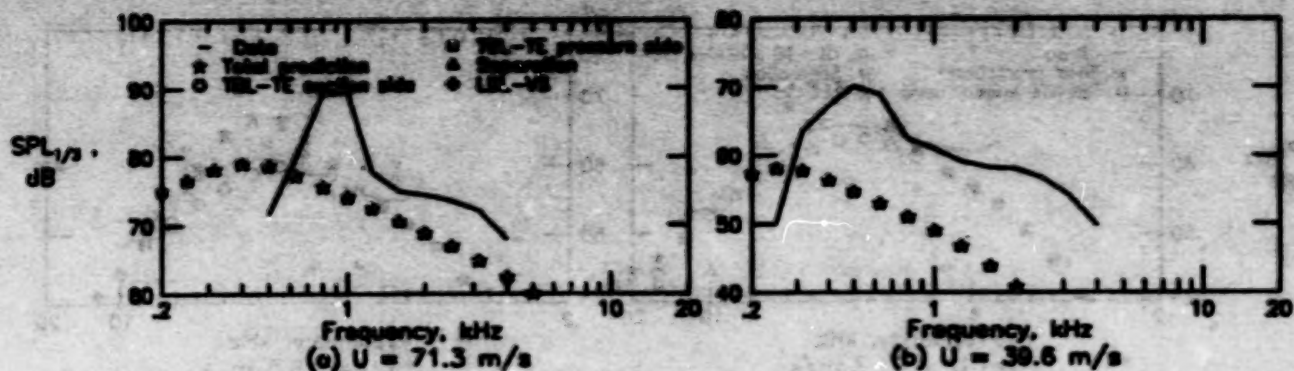


Figure 69. Self-noise spectra for 5.08-cm-chord airfoil with untripped BL at $\alpha_i = 19.8^\circ$ ($\alpha_s = 15.4^\circ$).

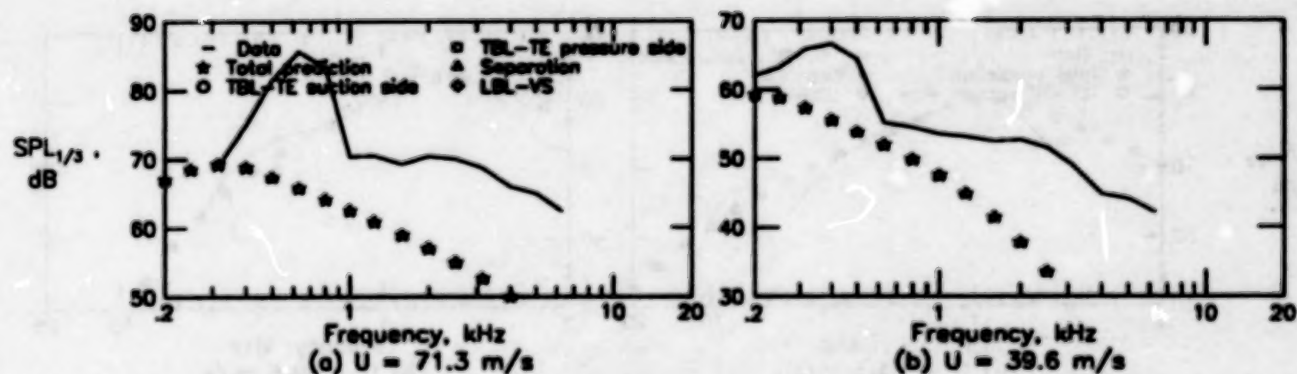


Figure 70. Self-noise spectra for 5.08-cm-chord airfoil with untripped BL at $\alpha_i = 25.2^\circ$ ($\alpha_s = 19.6^\circ$).

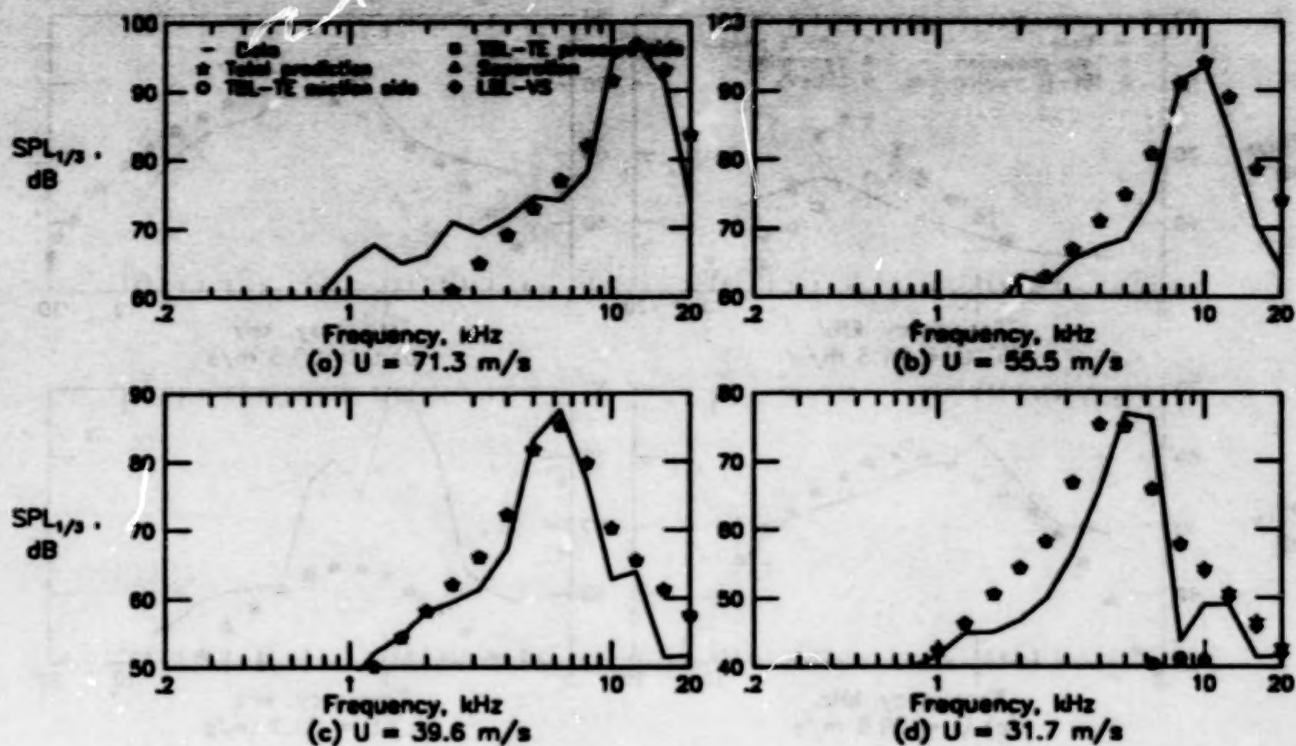


Figure 71. Self-noise spectra for 2.54-cm-chord airfoil with untripped BL at $\alpha_i = 0^\circ$ ($\alpha_s = 0^\circ$).

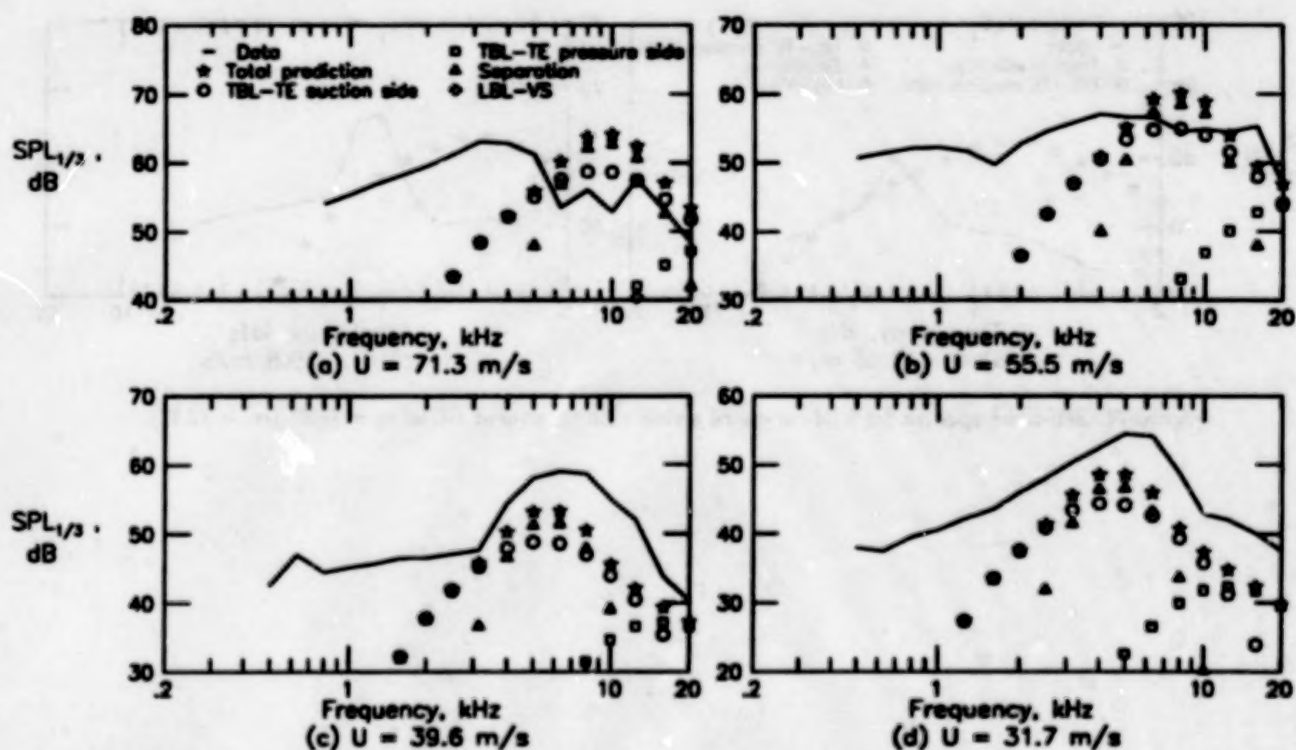


Figure 72. Self-noise spectra for 2.54-cm-chord airfoil with untripped BL at $\alpha_i = 5.4^\circ$ ($\alpha_s = 4.8^\circ$).

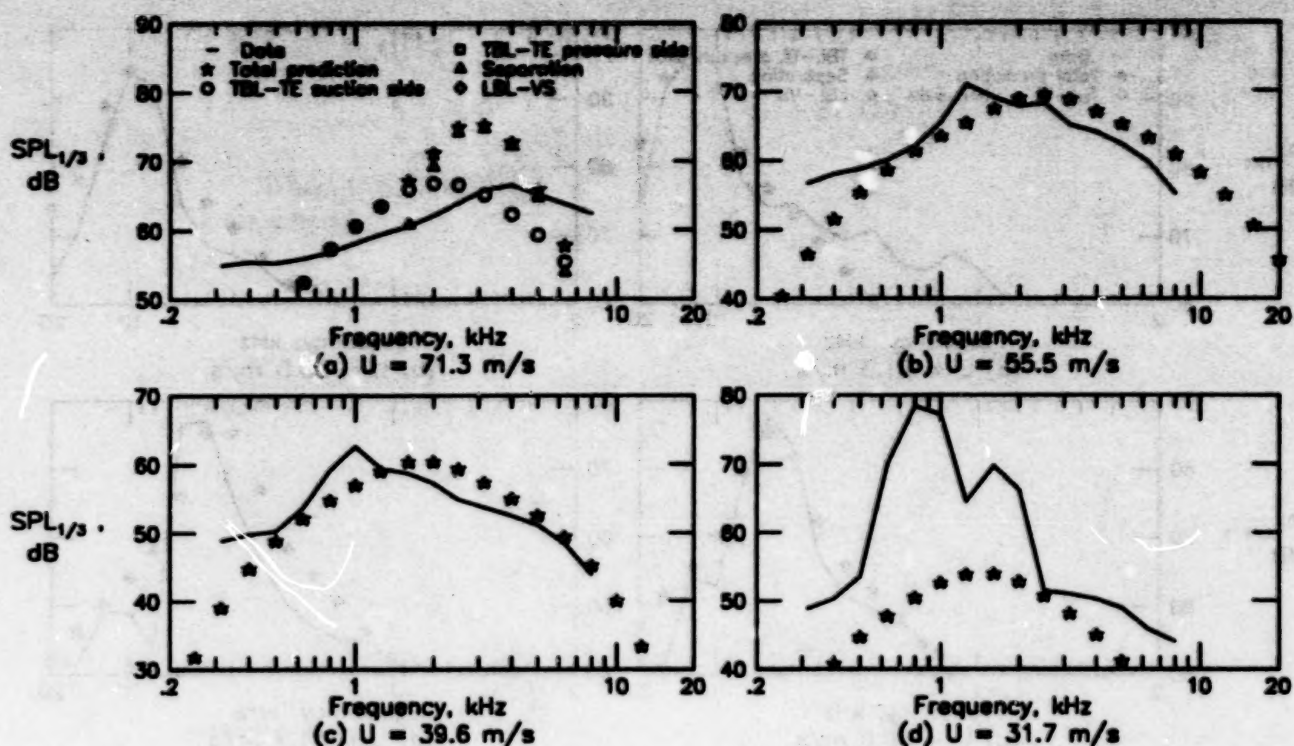


Figure 73. Self-noise spectra for 2.54-cm-chord airfoil with untripped BL at $\alpha_i = 10.8^\circ$ ($\alpha_s = 9.5^\circ$).

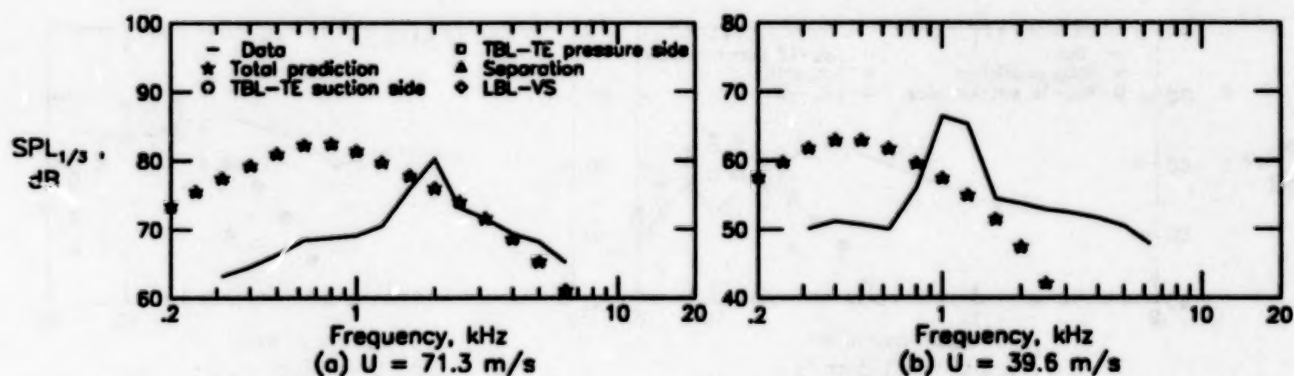


Figure 74. Self-noise spectra for 2.54-cm-chord airfoil with untripped BL at $\alpha_i = 14.4^\circ$ ($\alpha_s = 12.7^\circ$).

5. Spectral Scaling

In this section, the scaling laws are developed for the five self-noise mechanisms. The spectra of figures 11 to 74 form the basis of the scaling for three of the mechanisms: turbulent-boundary-layer-trailing-edge (TBL-TE) noise and separation noise were scaled from the tripped boundary-layer cases, and laminar-boundary-layer-vortex-shedding (LBL-VS) noise was scaled from the untripped cases. For the tip vortex formation noise mechanism, both the data and the scaling approach are obtained from reference 18. Finally, for TE-bluntness-vortex-shedding noise, spectral data from the study of reference 2, as well as previously unpublished data from that study, form the basis of scaling analysis.

5.1. Turbulent-Boundary-Layer-Trailing-Edge Noise and Separated Flow Noise

What has become traditional TE noise scaling is based on the analysis of Ffowcs Williams and Hall (ref. 5). For the problem of turbulence convecting at low subsonic velocity U_c above a large plate and past the trailing edge into the wake, the primary result is

$$\langle p^2 \rangle \propto \rho_0^2 v'^2 \frac{U_c^3}{c_0} \left(\frac{L\mathcal{L}}{r^2} \right) \bar{D} \quad (17)$$

where $\langle p^2 \rangle$ is the mean-square sound pressure at the observer located a distance r from the edge. The medium density is ρ_0 , v'^2 is the mean-square turbulence velocity, c_0 is the speed of sound, L is the spanwise extent wetted by the flow, and \mathcal{L} is a characteristic turbulence correlation scale. The directivity factor \bar{D} equals 1 for observers normal to the surface from the TE. The usual assumptions for boundary-layer flow are that $v' \propto U_c \propto U$ and $\mathcal{L} \propto \delta$ or δ^* , where δ and δ^* are, respectively, the boundary-layer thickness and displacement thickness. Fink (ref. 25), when normalizing airframe noise data where TBL-TE noise was believed to be dominant, assumed a universal spectrum shape $F(\text{St})$ for the noise, where St is the Strouhal number $f\delta/U$. The shape $F(\text{St})$ depended only on the ratio of St to its peak value St_{peak} . This gave the following normalization form for the 1/3-octave sound pressure level spectral presentation:

$$\text{SPL}_{1/3} - 10 \log \left[\left(\frac{U}{100} \right)^5 \frac{\delta L}{r^2} \right] = F(\text{St}) + K \quad (18)$$

with $\text{SPL}_{1/3} = \text{OASPL} + F(\text{St})$ and where K is an empirical constant which was determined when the velocity U is given in units of knots.

As mentioned in section 1, some of the airfoil self-noise spectral data of the present report were presented, in uncorrected form, in reference 6, and normalized in the manner of equation (18) using measured values of δ . It was found that, contrary to what was previously assumed (e.g., refs. 25 and 3), the normalized levels, spectral shape, and Strouhal number were not independent of airfoil size, airfoil angle of attack, and free-stream velocity. However, the limited scope of the paper, as well as the uncertainty caused by the aforementioned extraneous noise contamination of the uncorrected spectra, prevented a clear definition of the functional dependences. The corrected spectra of the present report are used to determine the parametric dependences and to account for these in the spectral scaling.

5.1.1. Scaled Data

Zero angle of attack. In figure 75, 1/3-octave spectra for four airfoil sizes, each at four tunnel speeds, are scaled. The spectra are obtained from figures 11, 20, 26, and 32. The angle of attack is zero and the boundary layers are tripped. The form of the normalization is

$$\text{Scaled SPL}_{1/3} = \text{SPL}_{1/3} - 10 \log \left(M^5 \frac{\delta_0^* L}{r_e^2} \right) \quad (19)$$

where Mach number replaces the velocity in knots, δ_0^* replaces δ , and r_e replaces r . The retarded observer distance r_e equals here the measured value, 122 cm (see appendix B). For the right side of equation (19) to be accurately expressible by the form $F(\text{St}) + K$ of equation (18), the scaled spectra of figure 75 should be identical to one another for all cases. However, the peak Strouhal number, spectral shape, and scaled level vary significantly.

For each spectrum in figure 75, a symbol indicates the approximate spectral peak location. The peak locations were based on gross spectral shapes and trends rather than specific peak maximums. The peak Strouhal number, $\text{St}_{\text{peak}} = (f\delta^*/U)_{\text{peak}}$, and scaled levels corresponding to these peak locations are shown in figures 76 and 77, respectively, as a function of Reynolds number R_c . These data are also presented in table 1 (at the back of this report). Included in the figures are the other cases for tripped BL airfoils of different chord lengths. Also included are data at nonzero angle of attack for subsequent discussion. The displacement thicknesses for the suction side, δ_s^* , are used for these normalizations. In figure 76, St_{peak} for zero angle of attack (solid symbols) shows no clear R_c -dependence, but a Mach number dependence is apparent. The horizontal lines through the data correspond to the function

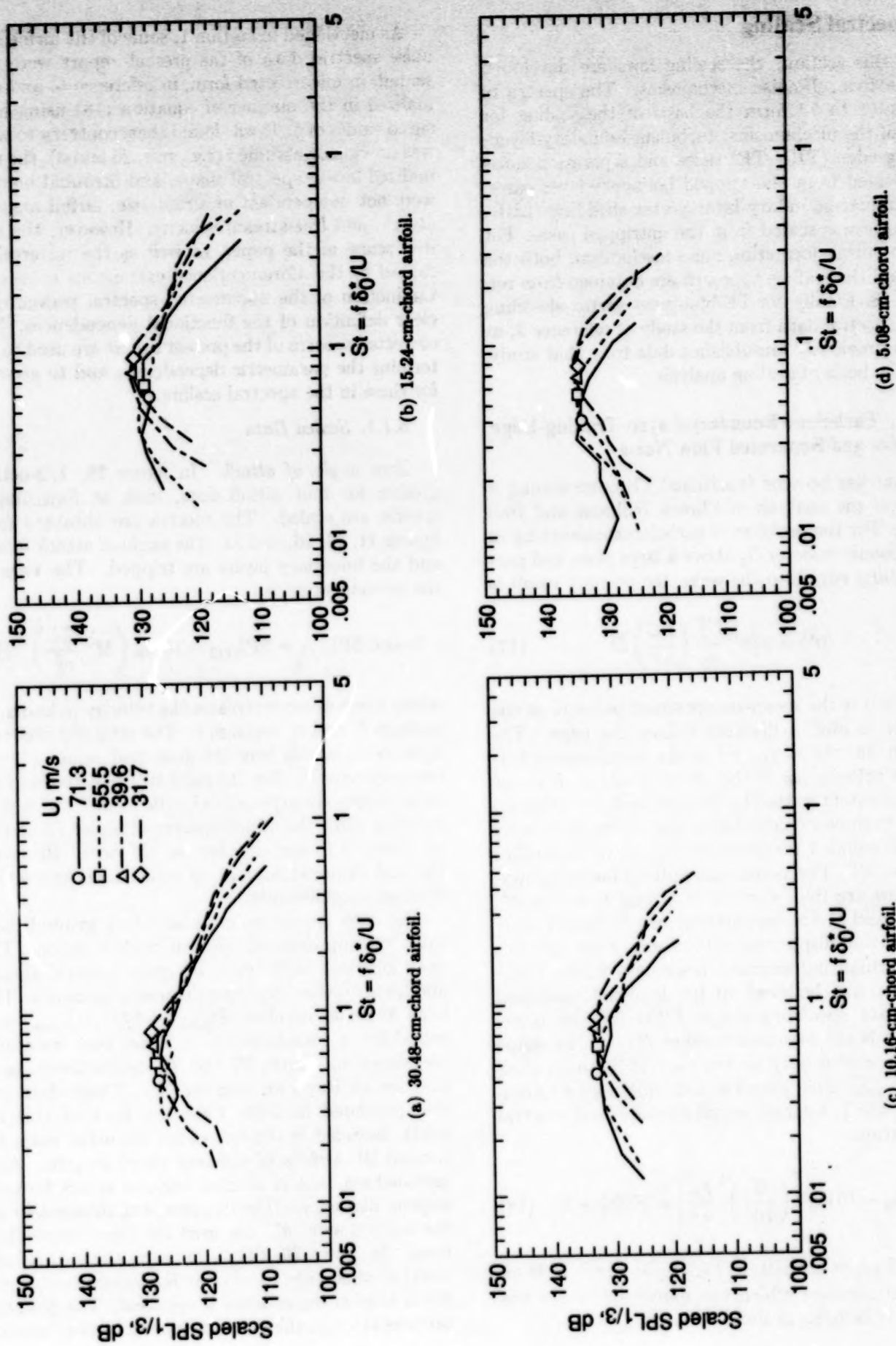


Figure 75. Scaled 1/3-octave spectra of tripped BL airfoils at $\alpha_t = 0^\circ$ ($\alpha_s = 0^\circ$). Symbols indicate approximate spectral peak locations.

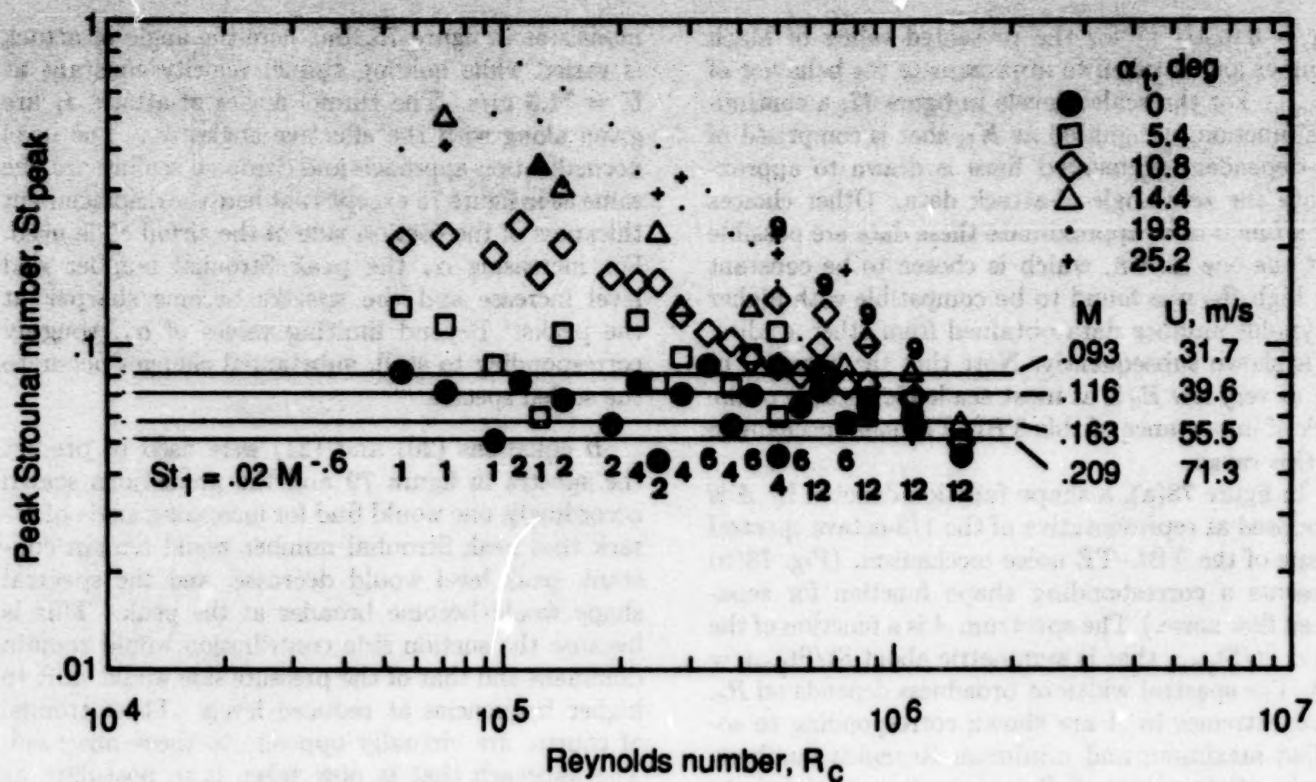


Figure 76. Peak Strouhal number for TBL-TE noise versus Reynolds number. Numbers aligned with data are chord sizes in inches (for brevity of notation).

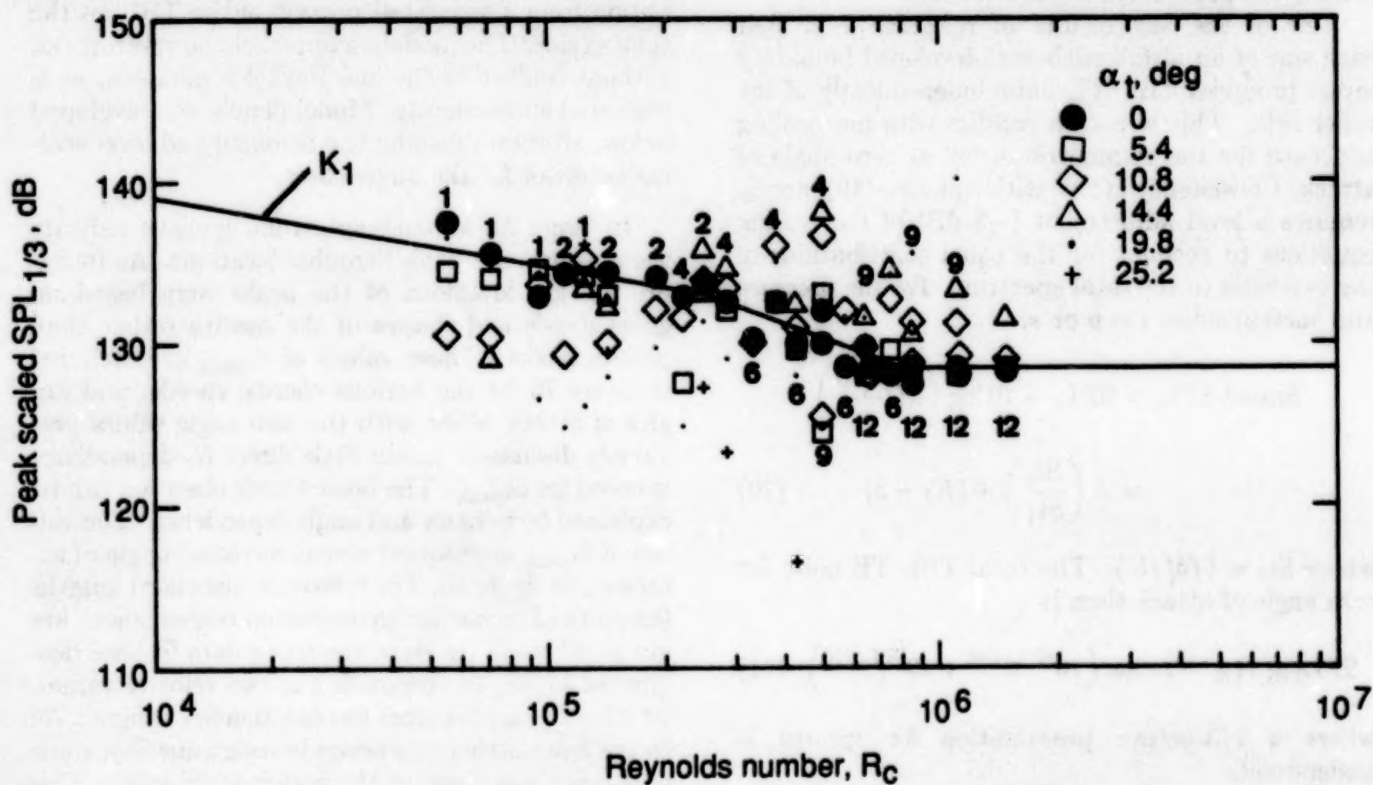


Figure 77. Peak scaled level for TBL-TE noise versus Reynolds number. Numbers aligned with data are chord sizes in inches.

$St_1 = 0.02M^{-0.5}$ for the presented values of Mach number and is taken to approximate the behavior of St_{peak} . For the scaled levels in figure 77, a continuous function, designated as K_1 , that is comprised of R_c -dependent segmented lines is drawn to approximate the zero-angle-of-attack data. Other choices for a function to approximate these data are possible but the one shown, which is chosen to be constant for high R_c , was found to be compatible with higher Reynolds number data obtained from other studies, as is shown subsequently. Note that the behavior of K_1 at very low R_c is at most academic because of the lack of importance of this TBL-TE noise mechanism in this range.

In figure 78(a), a shape function denoted by A is proposed as representative of the 1/3-octave spectral shape of the TBL-TE noise mechanism. (Fig. 78(b) presents a corresponding shape function for separated flow noise.) The spectrum A is a function of the ratio St/St_{peak} that is symmetric about $St/St_{peak} = 1.0$. The spectral width or broadness depends on R_c . Two extremes in A are shown corresponding to so-called maximum and minimum Reynolds numbers. Intermediate values of R_c require interpolation. As seen in figure 75, the larger chords have the broadest TBL-TE spectra. The spectrum A was matched to these and the other chord lengths. The specific details of A and the other functions are given in the calculation procedures section (5.1.2.).

One of the key results of reference 2 is that each side of an airfoil with well-developed boundary layers produces TBL-TE noise independently of the other side. This is not in conflict with our scaling approach for the symmetric airfoil at zero angle of attack. Consistency of this with equation (19) merely requires a level adjustment (-3 dB) of the scaling equations to account for the equal contributions of the two sides to the total spectrum. For the pressure and suction sides, $i = p$ or s ,

$$\begin{aligned} \text{Scaled } SPL_i &= SPL_i - 10 \log \left(M^5 \frac{\delta_i^* L}{r_e^2} \right) \\ &= A \left(\frac{St_i}{St_1} \right) + (K_1 - 3) \end{aligned} \quad (20)$$

where $St_i = (f\delta_i^*/U)$. The total TBL-TE noise for zero angle of attack then is

$$SPL_{TBL-TE} = 10 \log \left(10^{SPL_s/10} + 10^{SPL_p/10} \right) \quad (21)$$

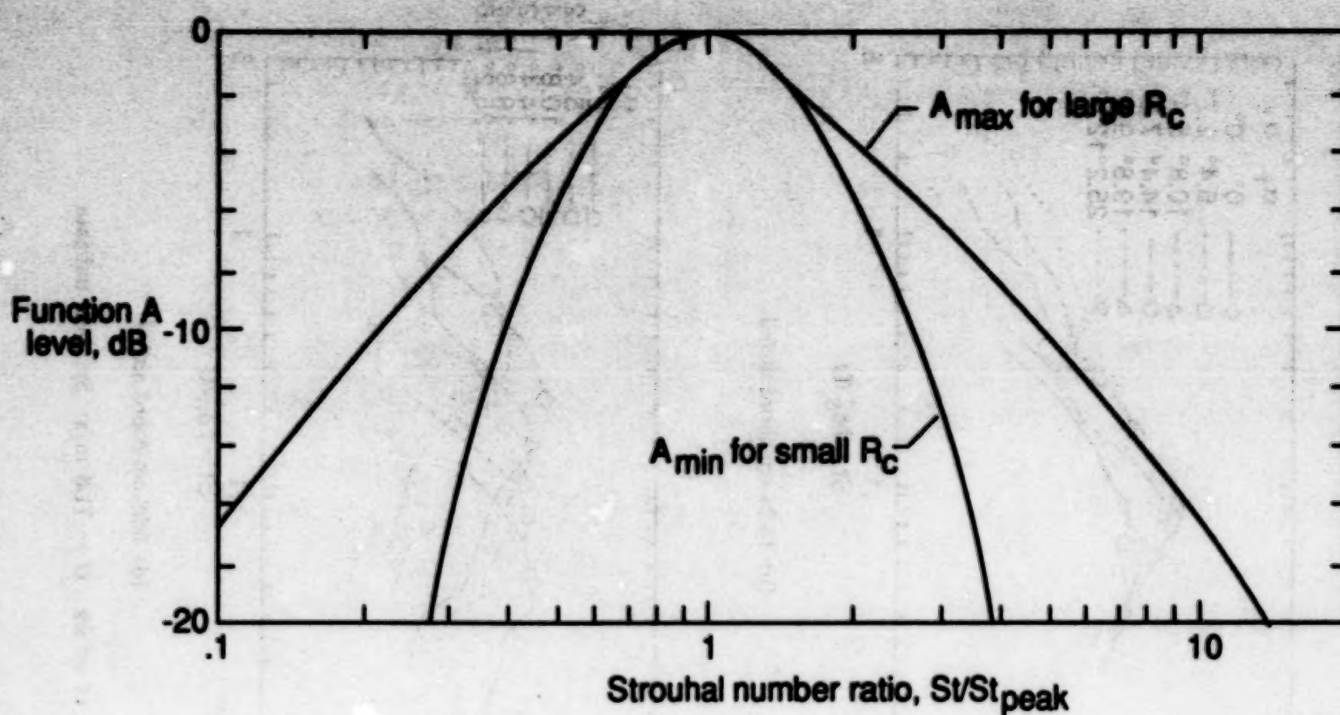
where a 1/3-octave presentation for spectra is understood.

Nonzero angle of attack. In figure 79, scaled noise spectra are presented for the same tripped BL airfoil

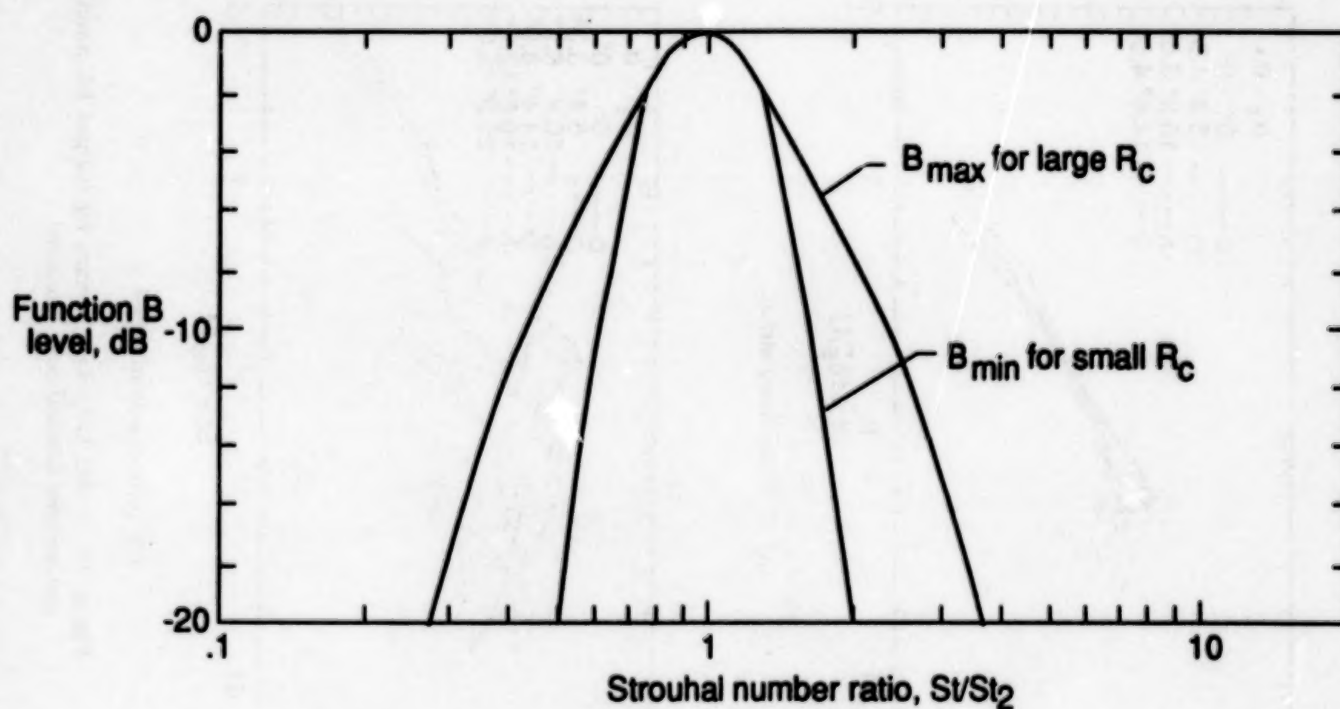
models as in figure 75, but here the angle of attack is varied while holding tunnel velocity constant at $U = 71.3$ m/s. The tunnel angles of attack α_t are given along with the effective angles α_e . The level normalization approach and Strouhal scaling are the same as in figure 75 except that here the displacement thickness of the suction side of the airfoil δ_s^* is used. For increasing α_e , the peak Strouhal number and level increase and the spectra become sharper at the peaks. Beyond limiting values of α_e , roughly corresponding to stall, substantial changes occur to the scaled spectra.

If equations (20) and (21) were used to predict the spectra in figure 79 and the predictions scaled accordingly, one would find for increasing angle of attack that peak Strouhal number would remain constant, peak level would decrease, and the spectral shape would become broader at the peak. This is because the suction side contribution would remain dominant and that of the pressure side would shift to higher frequencies at reduced levels. These trends, of course, are virtually opposite to those observed. The approach that is now taken is to postulate at nonzero angles of attack an additional contribution to the spectrum that controls the spectral peak. To justify this, one could hypothesize that the spectrum is the total from attached TBL contributions, as formulated in equations (20) and (21), and a contribution from a separated portion of the TBL on the suction side. The modeling approach, however, is not without conflict at the low Reynolds numbers, as is discussed subsequently. Model details are developed below, after establishing the Strouhal and level scaling behavior for the angle cases.

In figure 79, for each spectrum, symbols indicate the approximate peak Strouhal locations. As in figure 75, the locations of the peaks were based on gross trends and shapes of the spectra rather than precise peaks. These values of St_{peak} are included in figure 76 for the various chords, speeds, and angles of attack, along with the zero angle values previously discussed. Again little direct R_c -dependence is noted for St_{peak} . The basic trends observed can be explained by velocity and angle dependence. The values of St_{peak} are plotted versus corrected angle of attack α_e in figure 80. For reference, the chord lengths (in units of inches for presentation convenience) are given. Through the data are drawn data-fit lines designated as St_2 , corresponding to two velocity values. At $\alpha_e = 0^\circ$, St_2 becomes the function St_1 of figure 76. In the hand-fitting procedure to determine St_2 , some preference was given to the higher speed cases. This preference is discussed subsequently with regard to Strouhal peak level scaling. As for the substantial

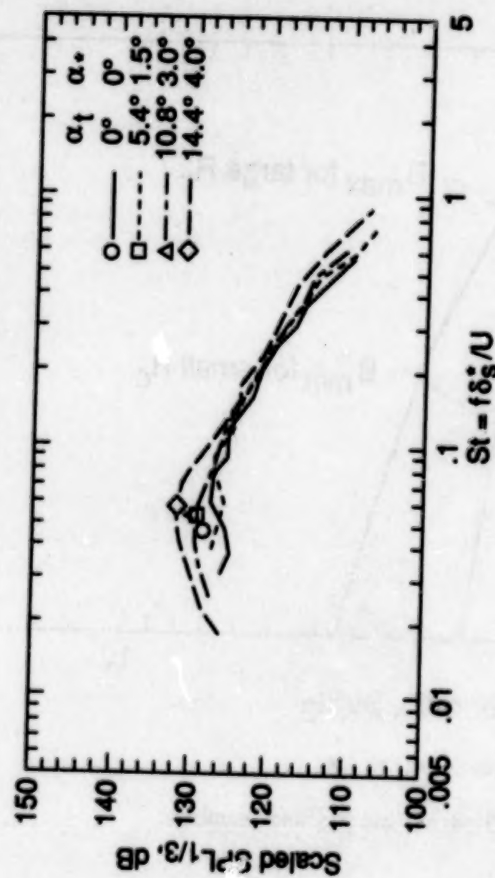


(a) Function A for TBL-TE noise, equations (35) to (40).

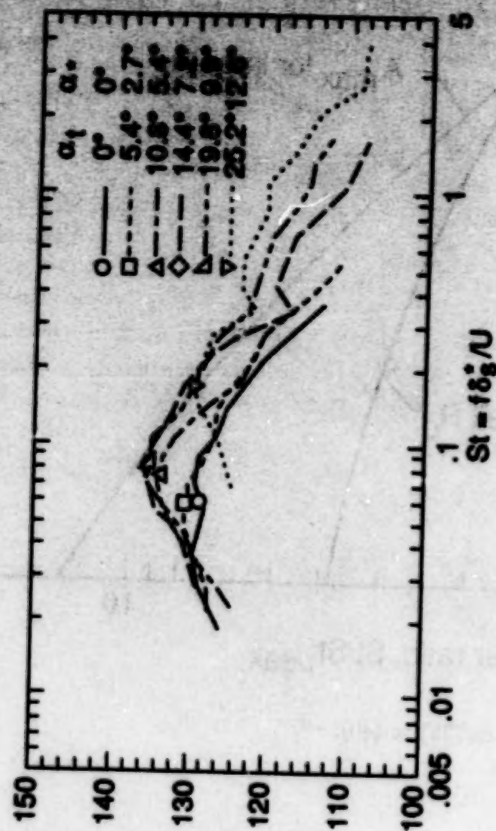


(b) Function B for separated flow noise, equations (41) to (46).

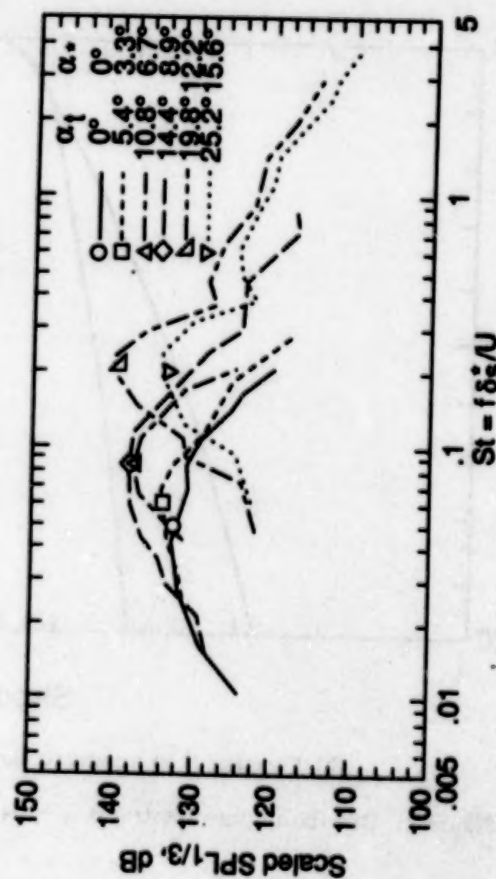
Figure 78. One-third-octave spectral shapes as functions of Strouhal and Reynolds numbers.



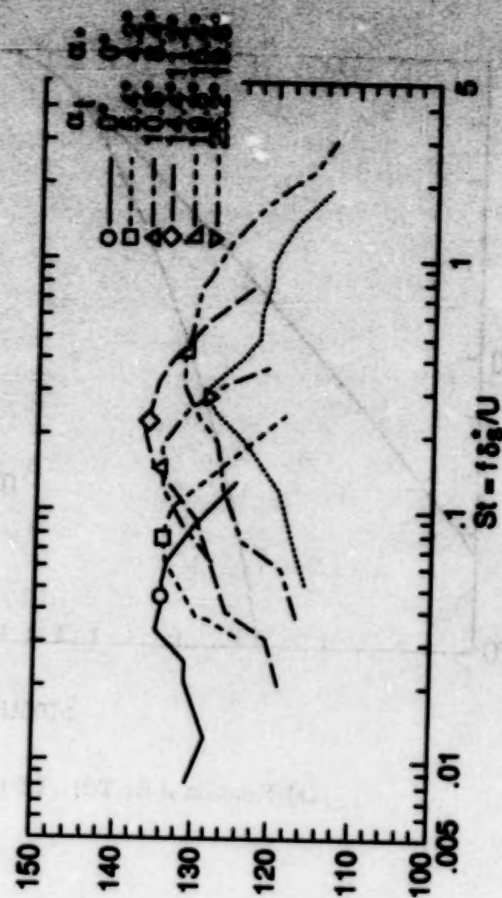
(a) 30.48-cm-chord airfoil.



(b) 15.24-cm-chord airfoil.



(c) 10.16-cm-chord airfoil.



(d) 5.08-cm-chord airfoil.

Figure 79. Scaled 1/3-octave spectra for tripped BL airfoils at various angles of attack. $U = 71.3$ m/s. Symbols indicate approximate spectral peak locations.

data scatter of figure 80, some comments are warranted. It was found that if one used the actual measured values of δ_s^* (where available) in the Strouhal scaling, one would have a similar degree of scatter to that shown in figure 80, where scaled values of δ_s^* (eq. (12)) were used. Also if untripped BL airfoil results were plotted, for those limited number of cases where the LBL-VS shedding source is not apparent in the spectra, the scatter and trend would be about the same as those shown in figure 80. Other deviations of the data from the St_2 lines occur at mid to high angles of attack, where the low-frequency parts of the spectra were limited by the experimental high-pass filtering and thus values of St_{peak} were inaccurately large. The behavior of St_2 seen in figure 80 at the higher angles of attack (where the horizontal lines are placed lower than the data) was chosen to approximately correct this bias.

The scaled levels corresponding to spectral peaks chosen in figure 79 are shown in figure 77 with the other cases. The previously indicated conflict within the data base for the proposed modeling approach, which hypothesizes contributions from two attached TBL's and an angle-dependent separation-related portion, is seen in figure 77. Peak levels for the two smallest chord lengths, except at the highest speeds, significantly decrease as the angle of attack increases from zero. This is incompatible with the modeling approach. A choice is made to ignore the conflicting low Reynolds number data in the model development. While admitting that the inclusion of the low Reynolds number behavior would conceptually be desirable for completeness of the modeling, the exclusion is believed justifiable because of the greater interest in higher Reynolds number conditions. The TBL-TE noise mechanism is not considered important for low Reynolds numbers. Even if this were not the case, it is not certain that the present test flow conditions with heavy leading-edge tripping for airfoils at nonzero angles of attack properly represent the mechanism, especially for higher angles where relaminarization of the pressure-side boundary layer is possible. Regardless, the results of the scaling are compared subsequently with the spectra of all the data to allow a direct assessment of the effect of modeling choices.

The scaled levels of figure 77 for chord lengths of 10.16, 15.24, 22.86, and 30.48 cm are plotted in figure 81 versus α_s . If the portion of these levels that cannot be accounted for by the modeling of equations (20) and (21) can be extracted, this portion would be designated as the separated flow noise contribution. Calculations were performed by taking into account that the Strouhal dependence of A in equation (20) would follow St_1 of figure 76

rather than St_2 of figure 80, which applies to that portion extracted. The extracted levels are given in figure 82. These extracted levels are normalized by subtracting the zero-angle-of-attack function of figure 77 (K_1) for the particular chord lengths and speeds. Although substantial scatter is present, a basic trend of increasing importance for increasing angle and speed is seen. Drawn through the data is a function designated as $K_2 - K_1$ which represents a partially observed, partially postulated dependence on velocity and angle of attack. The assigned spectral shape for this additive source is function B , which is given in figure 78(b) and is defined in a manner similar to function A of figure 78(a) to have a width which is dependent on chord Reynolds number.

The resulting scaling model for the angle-dependent noise SPL_α is

$$\begin{aligned} \text{Scaled } SPL_\alpha &= SPL_\alpha - 10 \log \left(M^5 \frac{\delta_s^* L}{r_c^2} \right) \\ &= B \left(\frac{St_s}{St_2} \right) + K_2 \end{aligned} \quad (22)$$

where this represents the separated-boundary-layer noise contribution to the total noise. The total TBL-TE and separation noise is then

$$\begin{aligned} SPL_{TOT} &= 10 \log \left(10^{SPL_\alpha/10} + 10^{SPL_s/10} \right. \\ &\quad \left. + 10^{SPL_p/10} \right) \end{aligned} \quad (23)$$

During development of the scaling procedures, equations (20), (22), and (23) were compared with spectra for all tripped BL airfoils and with spectra for the untripped BL airfoils for which TBL-TE noise appeared to significantly contribute. Analyses of comparisons resulted in optimization of curves A and B , as well as development of the specific calculation procedures. The analysis found that better results are obtained when the Strouhal dependency of the suction-side spectrum SPL_s is $(St_1 + St_2)/2$ rather than St_1 . It was found that for better SPL agreement, one should make an adjustment in pressure-side level SPL_p (defined as ΔK_1 in the following section) as a function of angle of attack and Reynolds number based on the displacement thickness δ_p^* . This adjustment diminishes the pressure-side contribution for increasing angle and decreasing velocity. Also it was found that the drastic spectral shape changes that occur at sufficiently high angles of attack, near stall, are roughly simulated by a calculation procedure change. At the value of α_s corresponding to the peak of the appropriate K_2 curve, the spectral

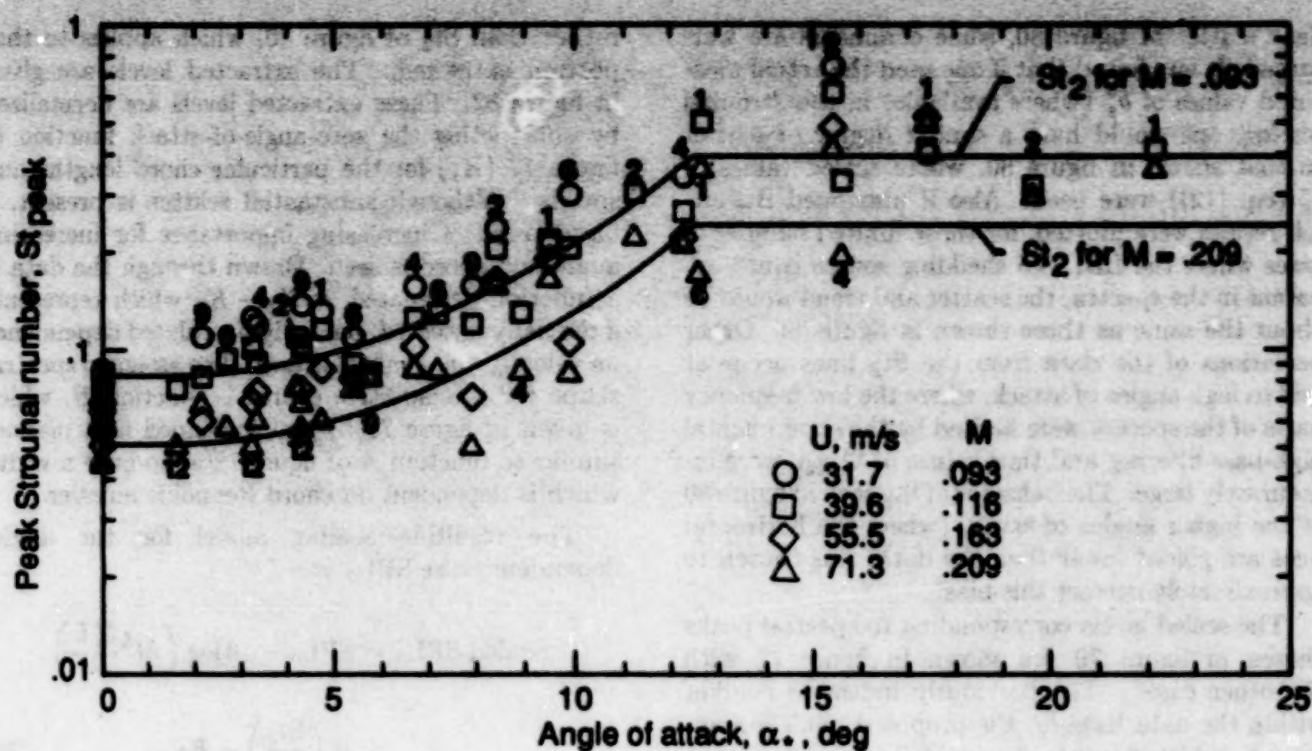


Figure 80. Peak Strouhal number for TBL-TE noise versus angle of attack. Data from figure 76. Numbers aligned with data are chord sizes in inches.

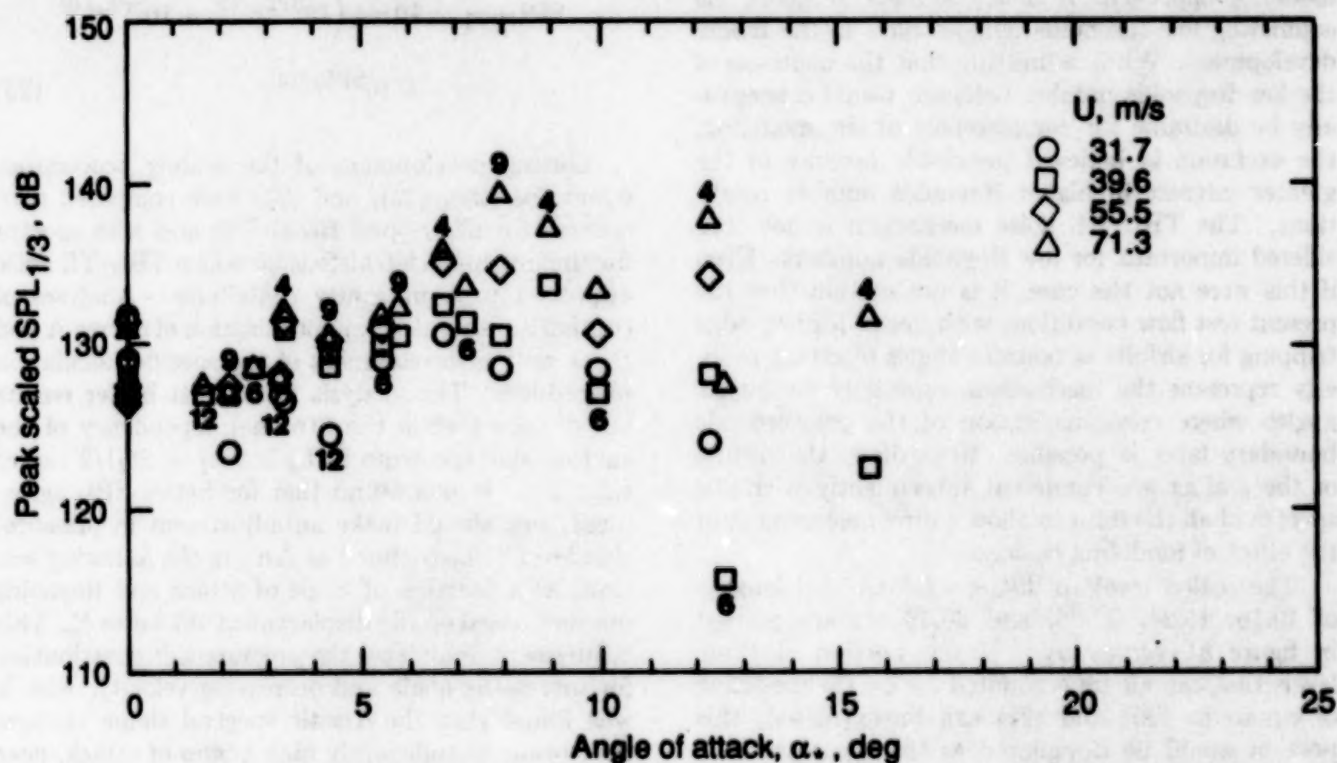


Figure 81. Peak scaled level for TBL-TE versus angle of attack. Data from figure 77. Numbers aligned with data are chord sizes in inches.

contributions SPL_p and SPL_s in equation (23) are eliminated and the B curve of equation (22) is replaced by an A curve corresponding to a value of R_s which is three times the actual value.

The calculation procedures are specified in the next section followed by comparison with the spectral data base.

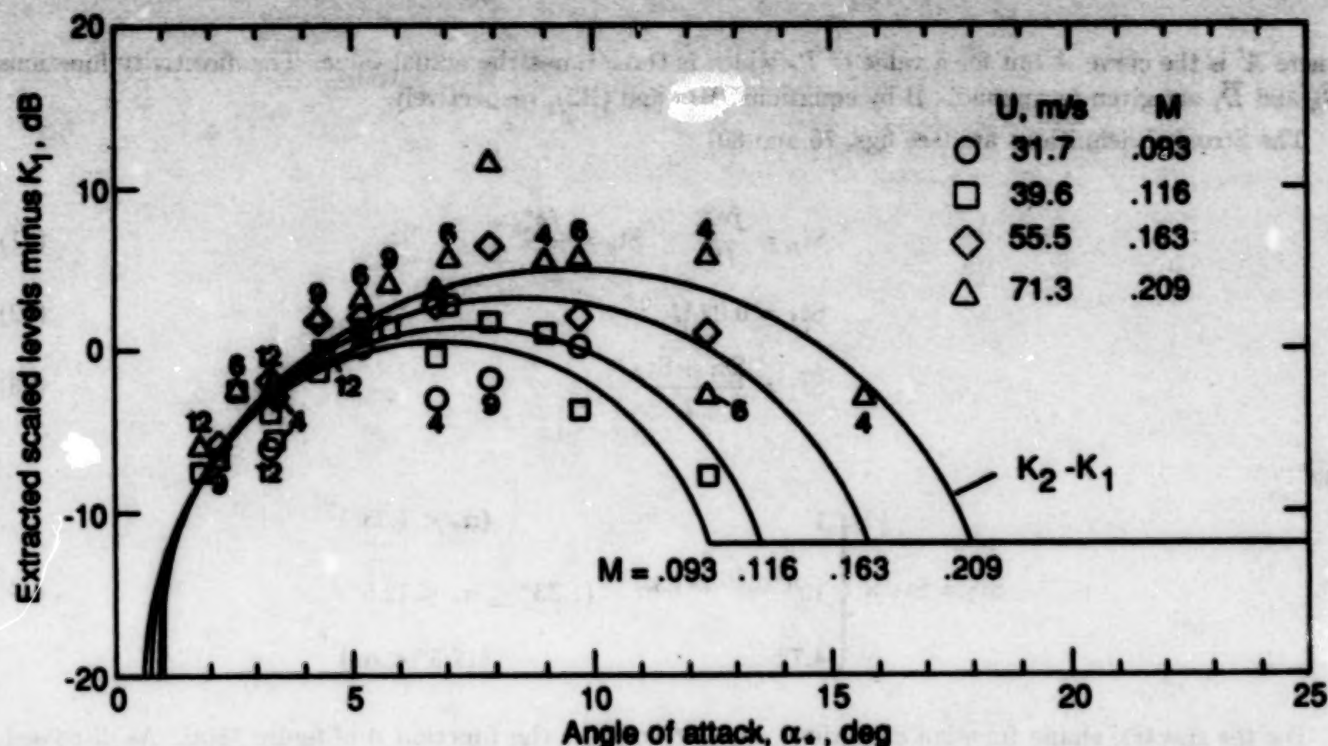


Figure 82. Angle-dependent scaled noise levels as referenced to zero angle of attack, TBL-TE noise model. Numbers aligned with data are chord sizes in inches.

5.1.2. Calculation Procedures

The total TBL-TE and separation noise spectrum in a 1/3-octave presentation is predicted by

$$SPL_{TOT} = 10 \log \left(10^{SPL_{\alpha}/10} + 10^{SPL_p/10} + 10^{SPL_s/10} \right) \quad (24)$$

where

$$SPL_p = 10 \log \left(\frac{\delta_p^* M^5 L \bar{D}_h}{r_e^2} \right) + A \left(\frac{St_p}{St_1} \right) + (K_1 - 3) + \Delta K_1 \quad (25)$$

$$SPL_s = 10 \log \left(\frac{\delta_s^* M^5 L \bar{D}_h}{r_e^2} \right) + A \left(\frac{St_s}{St_1} \right) + (K_1 - 3) \quad (26)$$

and

$$SPL_{\alpha} = 10 \log \left(\frac{\delta_s^* M^5 L \bar{D}_h}{r_e^2} \right) + B \left(\frac{St_s}{St_2} \right) + K_2 \quad (27)$$

for angles of attack up to $(\alpha_s)_0$, an angle to be defined later in this section. At angles above $(\alpha_s)_0$,

$$SPL_p = -\infty \quad (28)$$

$$SPL_s = -\infty \quad (29)$$

and

$$SPL_{\alpha} = 10 \log \left(\frac{\delta_s^* M^5 L \bar{D}_t}{r_c^2} \right) + A' \left(\frac{St_s}{St_2} \right) + K_2 \quad (30)$$

where A' is the curve A but for a value of R_c which is three times the actual value. The directivity functions \bar{D}_h and \bar{D}_t are given in appendix B by equations (B1) and (B2), respectively.

The Strouhal definitions are (see figs. 76 and 80)

$$St_p = \frac{f \delta_p^*}{U} \quad St_s = \frac{f \delta_s^*}{U} \quad (31)$$

$$St_1 = 0.02 M^{-0.6} \quad (32)$$

$$\bar{St}_1 = \frac{St_1 + St_2}{2} \quad (33)$$

and

$$St_2 = St_1 \times \begin{cases} 1 & (\alpha_s < 1.33^\circ) \\ 10^{0.0054(\alpha_s - 1.33)^2} & (1.33^\circ \leq \alpha_s \leq 12.5^\circ) \\ 4.72 & (12.5^\circ < \alpha_s) \end{cases} \quad (34)$$

For the spectral shape function definitions, we first consider the function A of figure 78(a). As discussed, the function A for a particular Reynolds number R_c is obtained from an interpolation of the curves A_{\max} and A_{\min} , corresponding to chosen values, $(R_c)_{\max}$ and $(R_c)_{\min}$. The two curves are defined as

$$A_{\min}(a) = \begin{cases} \sqrt{67.552 - 886.788a^2} - 8.219 & (a < 0.204) \\ -32.665a + 3.981 & (0.204 \leq a \leq 0.244) \\ -142.795a^3 + 103.656a^2 - 57.757a + 6.006 & (0.244 < a) \end{cases} \quad (35)$$

and

$$A_{\max}(a) = \begin{cases} \sqrt{67.552 - 886.788a^2} - 8.219 & (a < 0.13) \\ -15.901a + 1.098 & (0.13 \leq a \leq 0.321) \\ -4.669a^3 + 3.491a^2 - 16.699a + 1.149 & (0.321 < a) \end{cases} \quad (36)$$

where a is the absolute value of the logarithm of the ratio of Strouhal number, $St = St_p$ or St_s , to the peak Strouhal number, $St_{\text{peak}} = St_1, \bar{St}_1$, or St_2 :

$$a = |\log(St/St_{\text{peak}})| \quad (37)$$

The absolute value is used because the spectral shape is modeled to be symmetric about $a = 0$.

The interpolative procedure includes defining a value, $a_0(R_c)$, at which the spectrum has a value of -20 dB. This -20 dB corresponds to a horizontal axis intercept in figure 78(a) for an interpolated curve. The function

$a_0(R_c)$ is given by

$$a_0(R_c) = \begin{cases} 0.57 & (R_c < 9.52 \times 10^4) \\ (-9.57 \times 10^{-13})(R_c - 8.57 \times 10^5)^2 + 1.13 & (9.52 \times 10^4 \leq R_c \leq 8.57 \times 10^5) \\ 1.13 & (8.57 \times 10^5 < R_c) \end{cases} \quad (38)$$

An interpolation factor $A_R(a_0)$ is determined from

$$A_R(a_0) = \frac{-20 - A_{\min}(a_0)}{A_{\max}(a_0) - A_{\min}(a_0)} \quad (39)$$

where $A_{\min}(a_0)$ and $A_{\max}(a_0)$ are the A_{\max} and A_{\min} spectra evaluated at a_0 . The spectrum shape A can now be evaluated for any frequency by computing the Strouhal number St and the corresponding a and using the interpolation factor. The result for use in equations (25), (26), and (30) is

$$A(a) = A_{\min}(a) + A_R(a_0)[A_{\max}(a) - A_{\min}(a)] \quad (40)$$

The function B in equation (27) and shown plotted in figure 78(b) is calculated in a manner similar to function A above. The two curves B_{\max} and B_{\min} , through which B is obtained from interpolation, are

$$B_{\min}(b) = \begin{cases} \sqrt{16.888 - 886.788b^2} - 4.109 & (b < 0.13) \\ -83.607b + 8.138 & (0.13 \leq b \leq 0.145) \\ -817.810b^3 + 355.210b^2 - 135.024b + 10.619 & (0.145 < b) \end{cases} \quad (41)$$

and

$$B_{\max}(b) = \begin{cases} \sqrt{16.888 - 886.788b^2} - 4.109 & (b < 0.10) \\ -31.330b + 1.854 & (0.10 \leq b \leq 0.187) \\ -80.541b^3 + 44.174b^2 - 39.381b + 2.344 & (0.187 < b) \end{cases} \quad (42)$$

where

$$b = |\log(St_s/St_2)| \quad (43)$$

The spectral shape B for intermediate values of R_c have horizontal axis intercepts at -20 dB in figure 78(b) for values of b of

$$b_0(R_c) = \begin{cases} 0.30 & (R_c < 9.52 \times 10^4) \\ (-4.48 \times 10^{-13})(R_c - 8.57 \times 10^5)^2 + 0.56 & (9.52 \times 10^4 \leq R_c \leq 8.57 \times 10^5) \\ 0.56 & (8.57 \times 10^5 < R_c) \end{cases} \quad (44)$$

The interpolation factor $B_R(b_0)$ is defined as

$$B_R(b_0) = \frac{-20 - B_{\min}(b_0)}{B_{\max}(b_0) - B_{\min}(b_0)} \quad (45)$$

and thus the result for use in equation (27) is

$$B(b) = B_{\min}(b) + B_R(b_0)[B_{\max}(b) - B_{\min}(b)] \quad (46)$$

The amplitude function K_1 in equations (25) and (26) is plotted in figure 77 and is given by

$$K_1 = \begin{cases} -4.31 \log(R_c) + 156.3 & (R_c < 2.47 \times 10^5) \\ -9.0 \log(R_c) + 181.6 & (2.47 \times 10^5 \leq R_c \leq 8.0 \times 10^5) \\ 128.5 & (8.0 \times 10^5 < R_c) \end{cases} \quad (47)$$

The level adjustment previously mentioned for the pressure-side contribution for nonzero angles of attack appears as ΔK_1 in equation (25). This is given by

$$\Delta K_1 = \begin{cases} \alpha_s [1.43 \log(R_{\delta_s}) - 5.29] & (R_{\delta_s} \leq 5000) \\ 0 & (5000 < R_{\delta_s}) \end{cases} \quad (48)$$

where R_{δ_s} is the Reynolds number based on pressure-side displacement thickness.

The amplitude function K_2 of equations (27) and (30) is plotted for some values of M in figure 82 and is given as

$$K_2 = K_1 + \begin{cases} -1000 & (\alpha_s < \gamma_0 - \gamma) \\ \sqrt{\beta^2 - (\beta/\gamma)^2(\alpha_s - \gamma_0)^2} + \beta_0 & (\gamma_0 - \gamma \leq \alpha_s \leq \gamma_0 + \gamma) \\ -12 & (\gamma_0 + \gamma < \alpha_s) \end{cases} \quad (49)$$

where

$$\left. \begin{aligned} \gamma &= 27.094M + 3.31 & \gamma_0 &= 23.43M + 4.651 \\ \beta &= 72.65M + 10.74 & \beta_0 &= -34.19M - 13.82 \end{aligned} \right\} \quad (50)$$

The angle definitions above are in units of degrees and are taken as positive in sign. The K_2 definition above is valid for all values of α_s , even when the calculation of the total noise in equation (24) switches from the use of equations (25), (26), and (27) for assumed attached TBL flow to equations (28), (29), and (30) for a supposedly stalled flow condition. The angle where the switch occurs, specified previously as $(\alpha_s)_0$, is taken to be equal to the peak of the K_2 function defined by γ_0 in equation (50) or whenever α_s exceeds 12.5° , whichever is first.

5.1.3. Comparison With Data

The scaling predictions of TBL-TE and separation noise are compared with the noise data in figures 11 to 43 for the tripped BL airfoils. The calculations used the appropriate values of δ^* from section 3 and the directivity functions from appendix B (where $r_e = 1.22$ m, $\Theta_e = 90^\circ$, and $\Phi_e = 90^\circ$). The total self-noise is given as well as the individual noise components of TBL-TE noise from the suction and pressure sides and separation noise. The predictions follow the shapes and levels of the data, especially for the larger airfoils and the lower angles of attack where the scaling accuracy was most emphasized. Predictions of TBL-TE and separation noise are also shown for the untripped BL airfoils in figures 44

to 74. For the many untripped cases where these sources are predicted to be dominant, the agreement is generally good. Even where the LBL-VS noise dominates, the TBL-TE and separation contributions help with the overall spectral agreement.

5.2. Laminar-Boundary-Layer-Vortex-Shedding Noise

As previously described in section 1, laminar-boundary-layer instabilities couple with acoustic feedback to produce quasi-tonal noise. In contrast to TBL-TE noise, there are no LBL-VS noise scaling methods established in the literature because of the erratic behavior of the multiple tones in the narrow-band spectra and the general complexity of the

mechanism. Two key results from the literature which provide initial scaling guidance are (1) that the gross trend of the frequency dependence was found to scale on a Strouhal basis, with the relevant length scale being the laminar-boundary-layer thickness at the airfoil trailing edge (ref. 16), and (2) that on the basis of the limited data from the data base of the present paper as reported in reference (6), overall levels tended to coalesce to a unique function of R_c when normalized in the fashion of TBL-TE noise.

The scaling approach taken herein is similar to that taken for TBL-TE noise in the last section in that a universal spectral shape and Strouhal dependency is modeled in terms of boundary-layer parameters, Mach number, angle of attack, and Reynolds number. The use of 1/3-octave spectra, rather than narrow band, permits such an approach because the broad spectral bands overlap the tonal frequency spacing to give smoother and generally single-peaked spectra.

5.2.1. Scaled Data

Scaled 1/3-octave sound pressure level spectra for four airfoil sizes, each at four tunnel speeds, are presented in figure 83 from figures 44, 53, 59, and 65. The angle of attack for all is zero and the boundary layers are untripped. The normalization employs

$$\text{Scaled SPL}_{1/3} = \text{SPL}_{1/3} - 10 \log \left(M^5 \frac{\delta_p L}{r_c^2} \right) \quad (51)$$

for level scaling and

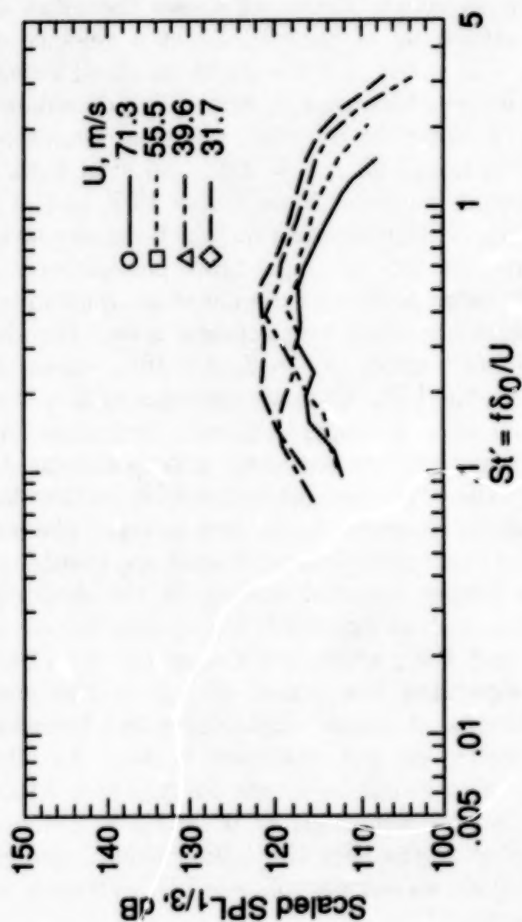
$$\text{St}' = \frac{f \delta_p}{U} \quad (52)$$

for Strouhal frequency scaling. For the symmetric airfoils at zero angle of attack, $\delta_p = \delta_s = \delta_0$. The scaling approach differs from the TBL-TE noise scaling because of the use of δ_p , the boundary-layer thickness on the pressure side of the airfoil, rather than δ_s^* , the boundary-layer displacement thickness on the suction side. The use of δ_p as the pertinent length scale follows from reference 16 and was found to give seemingly better results in initial scaling of the present data base than δ_p^* and by far better than c , δ_s , or δ_s^* for angles of attack other than zero.

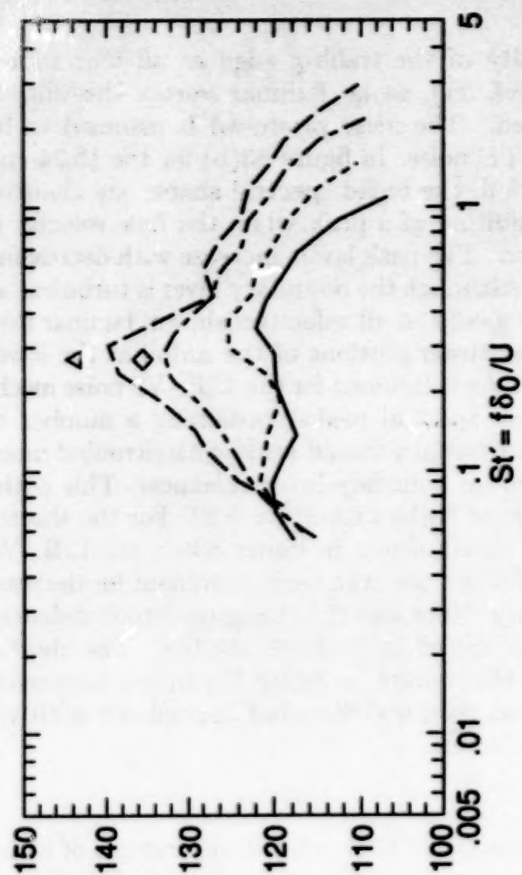
In figure 83(a) for the large 30.48-cm-chord airfoil, the spectra appear to be of smooth broad hump shapes. There is no apparent contribution to the spectra from LBL-VS noise which is peaked in character. The boundary layers are fully turbulent in

the vicinity of the trailing edge at all four tunnel speeds (ref. 21), so no laminar vortex shedding is established. The noise produced is assumed to be all TBL-TE noise. In figure 83(b) for the 15.24-cm-chord airfoil, the broad spectral shapes are changed by the addition of a peak when the flow velocity is diminished. The peak levels increase with decreasing velocity. Although the boundary layer is turbulent at the trailing edge at all velocities shown, laminar flow exists over larger portions of the airfoil at the lower velocities. As mentioned for the LBL-VS noise mechanism, any spectral peaks containing a number of tonal contributions should scale with Strouhal numbers based on boundary-layer thickness. This is the case in figure 83(b) with $\text{St}' \approx 0.27$. For the shorter 10.16-cm-chord airfoil, in figure 83(c), the LBL-VS noise peaks become even more dominant for decreasing velocity. Note also the changing Strouhal dependence, not noted in previous studies. The shorter 5.08-cm-chord airfoil, in figure 83(d), has even more pronounced level and Strouhal dependence with velocity variations.

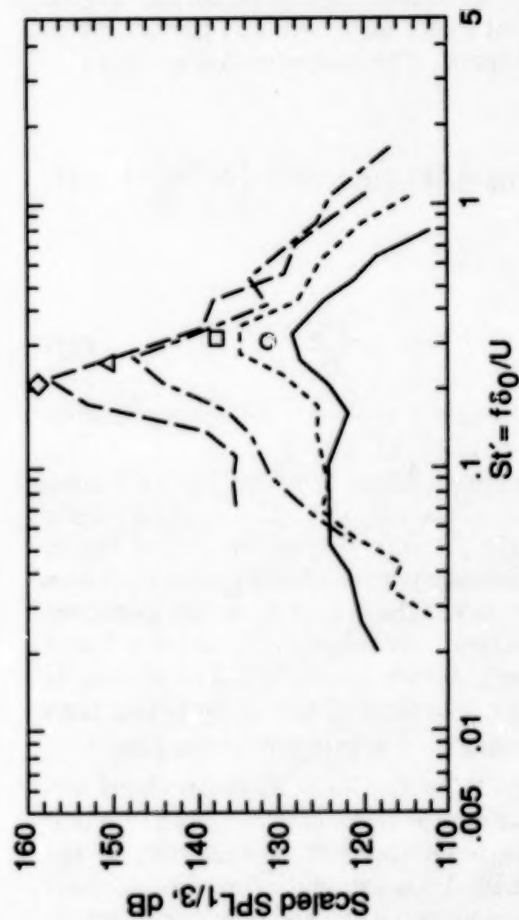
Whereas figure 83 shows the dependence of LBL-VS noise on velocity for the various airfoil sizes at zero angle of attack, figure 84 shows the effect of angle of attack α_s of the airfoils at a velocity of 71.3 m/s. The spectra for the 30.48-cm-chord airfoil, shown in figure 84(a), change from being dominated by TBL-TE noise, for $\alpha_s = 0^\circ$, to being dominated by LBL-VS noise, for $\alpha_s = 4.0^\circ$. So even with a large Reynolds number ($R_c = 1.52 \times 10^6$), LBL-VS noise occurs. With increasing α_s , the boundary layer on the pressure side becomes more laminar over a sufficiently large portion of the chord to result in increased shedding and corresponding noise. For the 15.24-cm-chord airfoil ($R_c = 7.58 \times 10^5$), shown in figure 84(b), the LBL-VS noise increases with α_s until a certain value is reached where it diminishes. At $\alpha_s = 7.2^\circ$, no apparent shedding noise is shown. At $\alpha_s = 9.5^\circ$, the noise changes appreciably to that for stalled flow as discussed in the last section. The use of δ_p as the characteristic length scale apparently results in a proper Strouhal scaling for the shedding noise peaks; but, as expected, the spectra for $\alpha_s = 0^\circ$, 7.2° , and 9.9° , which are dominated by TBL-TE and separated flow noise, diverge in this normalized format. A similar angle-dependent behavior where spectra do not coalesce is seen for the 10.16-cm-chord airfoil, in figure 84(c), where LBL-VS noise is apparent at $\alpha_s = 0^\circ$ and 3.3° but not at the higher angles. For the 5.08-cm-chord model, figure 84(d) shows large-amplitude LBL-VS noise at $\alpha_s = 0^\circ$ and 4.2° .



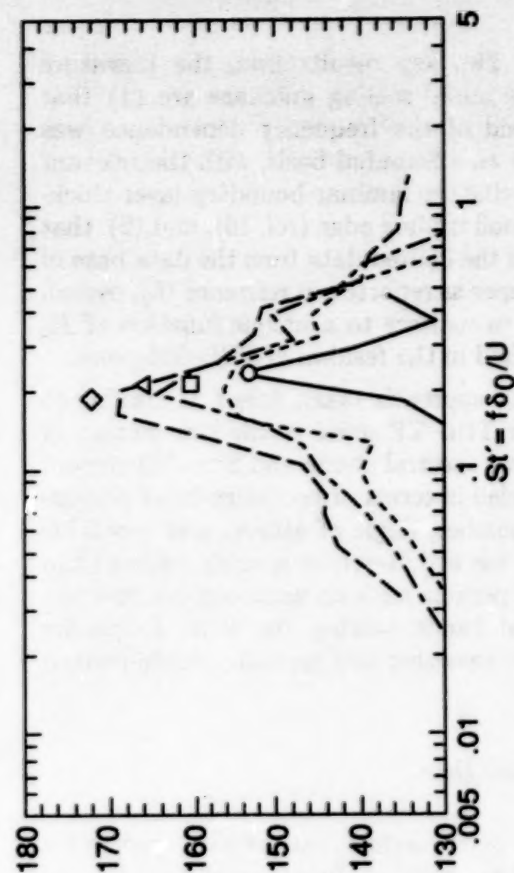
(a) 30.48-cm-chord airfoil.



(b) 15.24-cm-chord airfoil.

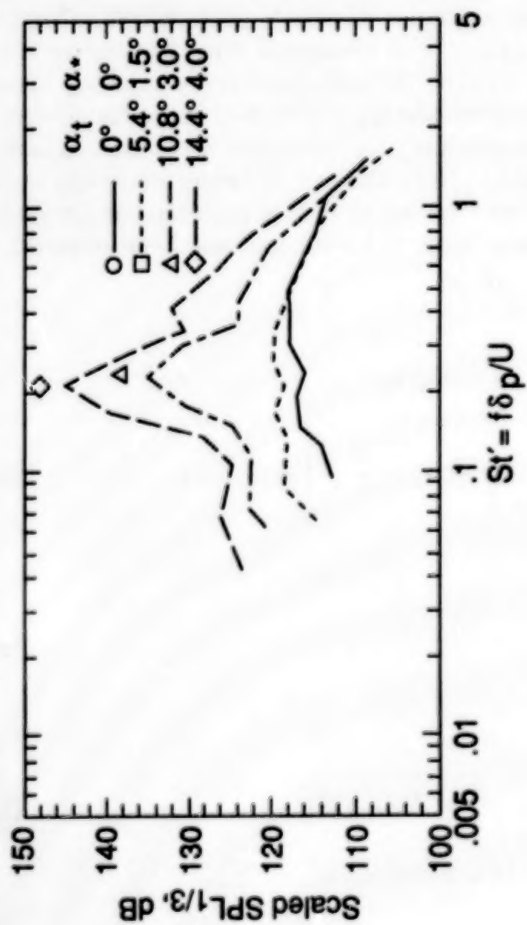


(c) 10.16-cm-chord airfoil.

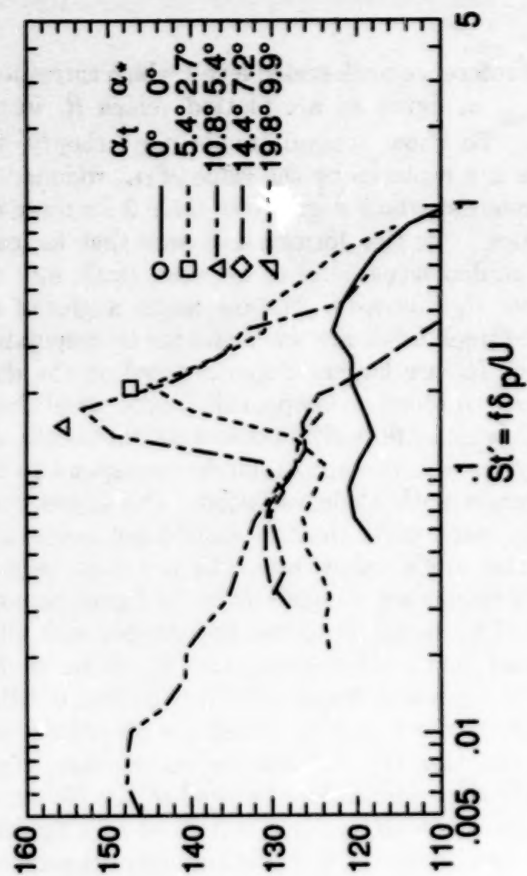


(d) 5.08-cm-chord airfoil.

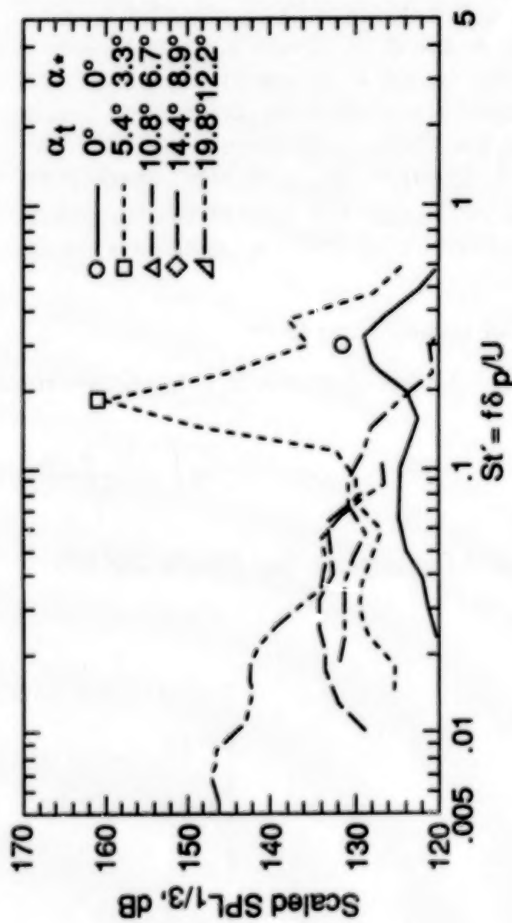
Figure 83. Scaled $1/3$ -octave spectra for untripped BL airfoils at $\alpha_i = 0^\circ$ ($\alpha_s = 0^\circ$). Symbols indicate approximate LBL-VS reference peak location.



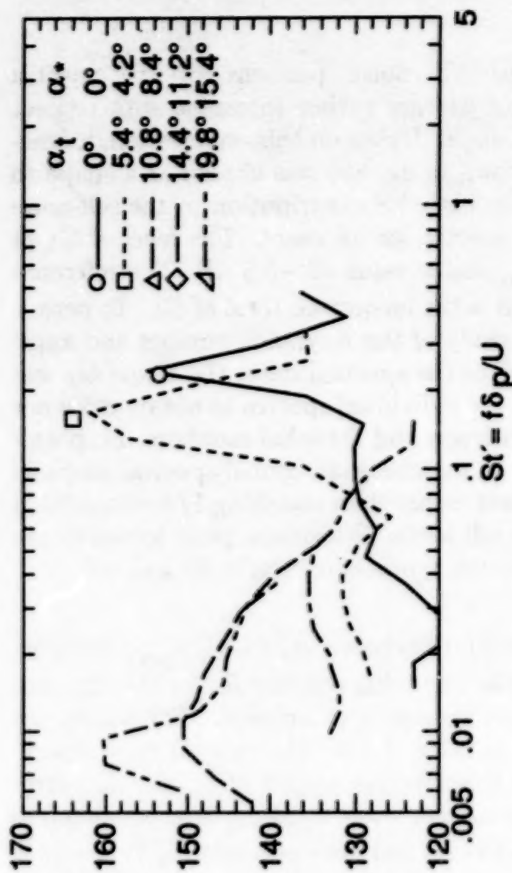
(a) 30.48-cm-chord airfoil.



(b) 15.24-cm-chord airfoil.



(c) 10.16-cm-chord airfoil.



(d) 5.08-cm-chord airfoil.

Figure 84. Scaled 1/3-octave spectra for untripped BL airfoils at various angles of attack. $U = 71.3$ m/s. Symbols indicate approximate LBL-VS reference peak locations.

The LBL-VS noise portions of the spectra (figs. 83 and 84) are rather invariant with respect to spectral shape. Based on this observation, a function G_1 (shown in fig. 85) was chosen as a shape to represent the LBL-VS contribution to the self-noise 1/3-octave spectra for all cases. The level of G_1 at $St' = St'_{peak}$ has a value of -3.5 dB. The reference level of 0 dB is the integrated total of G_1 . To permit an orderly study of the Reynolds number and angle dependences of the spectral data, the shape G_1 was matched to the individual spectra to obtain reference overall peak levels and Strouhal numbers. Emphasis was placed on matching the global spectral shape of G_1 to the data rather than matching 1/3-octave band peak or overall levels. Reference peak locations are indicated by the symbols in figures 83 and 84.

In figure 86, the chosen values of St'_{peak} are plotted versus the Reynolds number R_c for the 42 cases where LBL-VS noise is prominent. The values are also given in table 2 (at the back of this report) along with the effective angles of attack α_* corresponding to α_t . For $\alpha_* = 0$, St'_{peak} is approximately constant at low R_c and increases with R_c in the mid-range of R_c shown. The values of St'_{peak} are lower for nonzero angles of attack. A function St'_1 is drawn to approximate the data of zero angle of attack. A constant value for St'_1 is chosen for high R_c , where no zero-angle-of-attack data are present, because the value permits a simple angle dependence definition for St'_{peak} . In figure 87, St'_{peak} is normalized by St'_1 and plotted versus α_* . For each of the six airfoils, the line described by $10^{-0.04\alpha_*}$ approximates the angle dependence.

5.2.2. Calculation Procedures

The LBL-VS noise spectrum in a 1/3-octave presentation is predicted by

$$SPL_{LBL-VS} = 10 \log \left(\frac{\delta_p M^5 L \bar{D}_h}{r_e^2} \right) + G_1 \left(\frac{St'}{St'_{peak}} \right) + G_2 \left[\frac{R_c}{(R_c)_0} \right] + G_3(\alpha_*) \quad (53)$$

The Strouhal definitions are (see figs. 86 and 87)

$$St' = \frac{f \delta_p}{U} \quad (54)$$

$$St'_1 = \begin{cases} 0.18 & (R_c \leq 1.3 \times 10^5) \\ 0.001756 R_c^{0.3931} & (1.3 \times 10^5 < R_c \leq 4.0 \times 10^5) \\ 0.28 & (4.0 \times 10^5 < R_c) \end{cases} \quad (55)$$

The reference peak scaled levels which correspond to St'_{peak} in figure 86 are plotted versus R_c in figure 88. To show general trends more clearly, the symbols are replaced by the value of α_* , rounded off to the nearest whole degree (see table 2 for more exact values). In this format it is seen that for each α_* the scaled levels tend to increase, peak, and decrease as R_c increases. For the larger angles of attack, the peak levels are lower and the corresponding values of R_c are larger. Superimposed on the data are curves of identical shape, called here "level shape curves," which are positioned in a monotonically decreasing fashion to approximately correspond to the data trends with angle variation. The angles indicated for each curve position should not necessarily match the angle values listed for the data because the data values are rounded off in the figure, as mentioned. The intent is to use the curves, with their functional relationship to α_* and R_c shown in figure 88, to represent the amplitude definition of LBL-VS noise. In the following calculation procedures section, a function G_2 specifies the curve shape, G_3 is the angle dependence for the level of the G_2 curve, and a reference $(R_c)_0$ value is defined as a function of angle to specify the Reynolds number dependence. The success of the functions in normalizing the data is shown in figure 89 where peak scaled 1/3-octave level minus G_3 is compared with the function G_2 . In this format the individual angle numbers should ideally match the G_2 curve. Although the agreement shown is certainly not complete, it is regarded here as acceptable. Note that much better curve fits to the data would be possible if a requirement for monotonic functional behavior had not been imposed on G_3 and $(R_c)_0$.

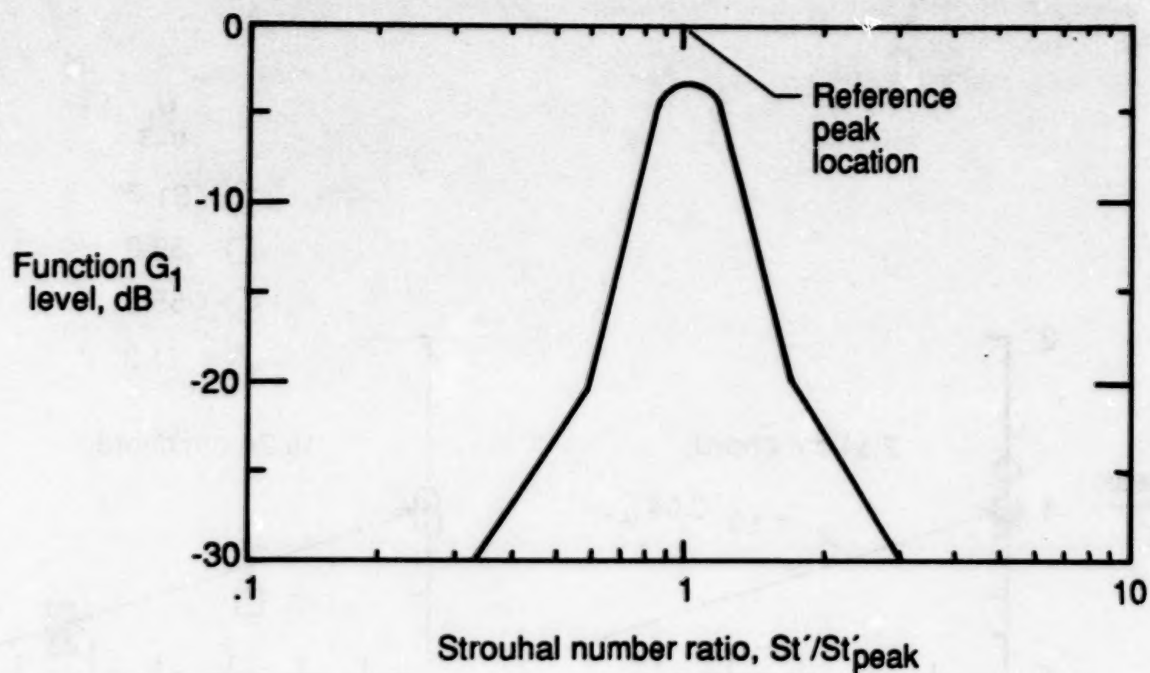


Figure 85. One-third-octave spectral shape function G_1 for LBL-VS noise, equation (57).

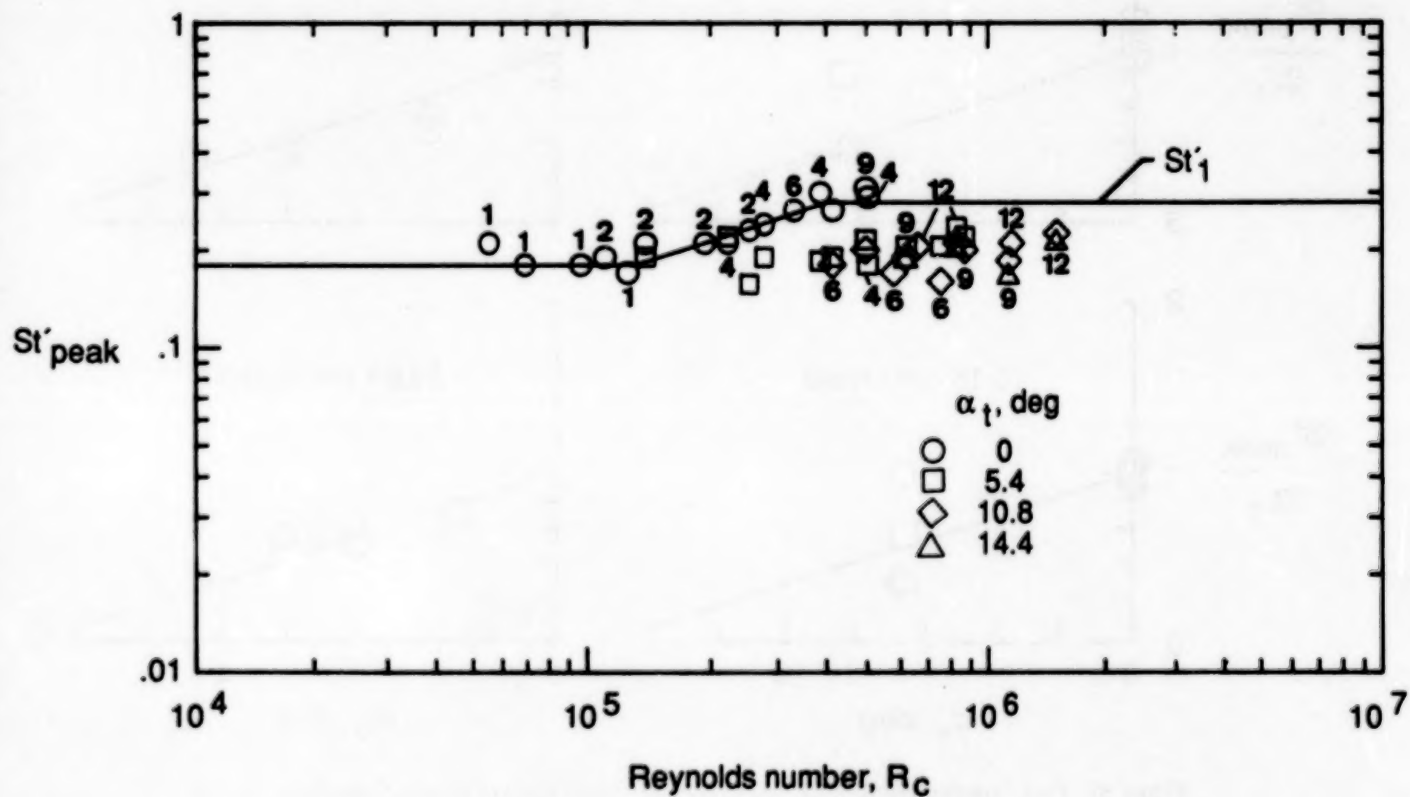


Figure 86. Peak Strouhal number for LBL-VS noise versus Reynolds number. Numbers aligned with data are chord sizes in inches.

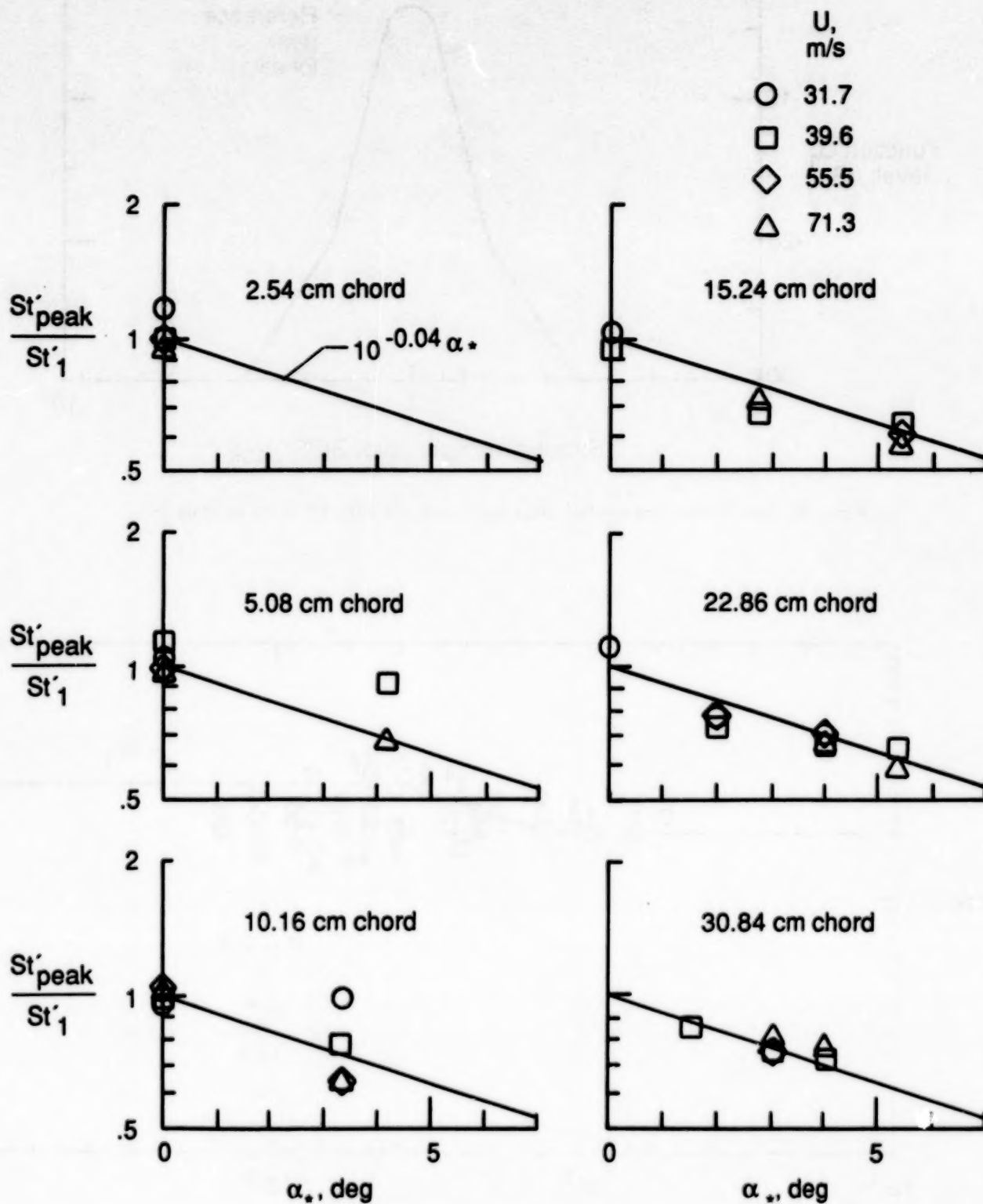


Figure 87. Peak Strouhal number for LBL-VS noise versus angle of attack. Data from figure 86.

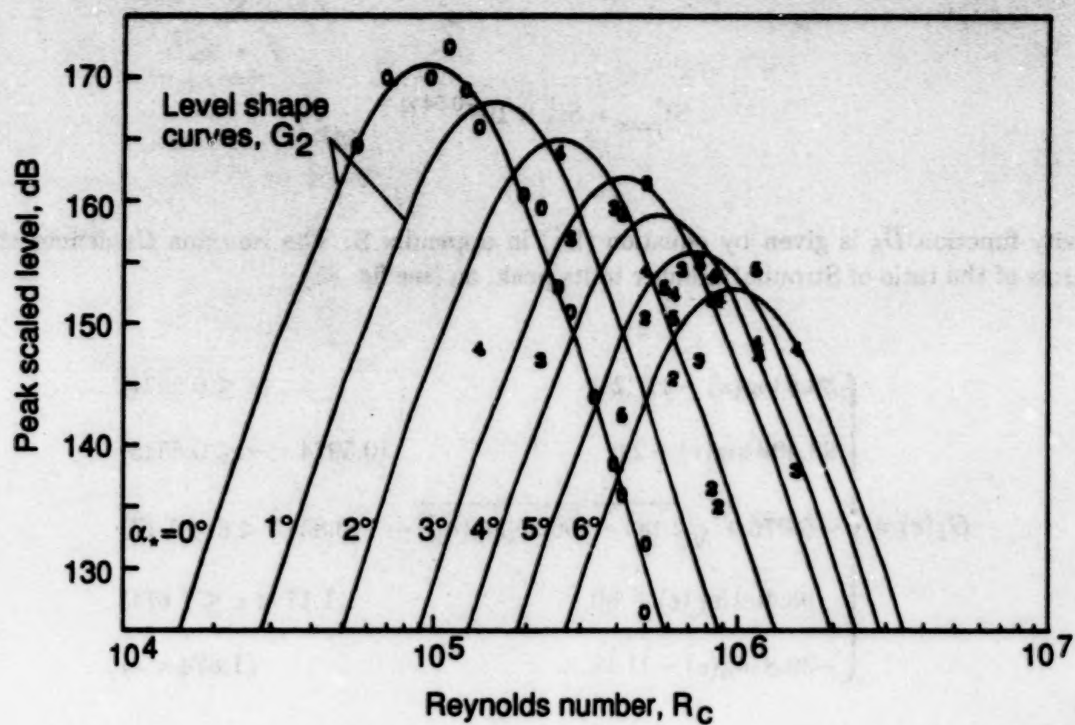


Figure 88. Peak scaled levels for LBL-VS noise versus Reynolds number. Data symbols are values of α_s rounded off to nearest degree.

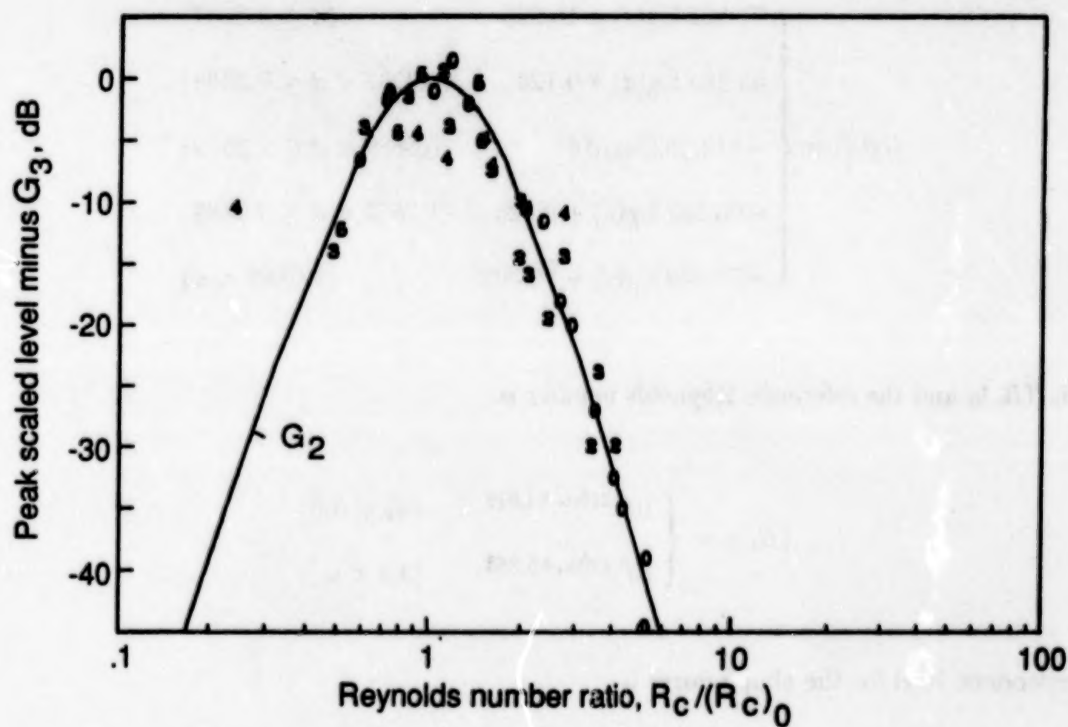


Figure 89. Normalization of LBL-VS noise peak scaled levels by functions G_2 , equations (58) and (59), and G_3 , equation (60). Data from figure 88. Data symbols are values of α_s rounded off to nearest degree.

and

$$St'_{\text{peak}} = St'_1 \times 10^{-0.04\alpha_s} \quad (56)$$

The directivity function \bar{D}_h is given by equation (B1) in appendix B. The function G_1 defines the spectral shape, in terms of the ratio of Strouhal number to its peak, as (see fig. 85)

$$G_1(e) = \begin{cases} 39.8 \log(e) - 11.12 & (e \leq 0.5974) \\ 98.409 \log(e) + 2.0 & (0.5974 < e \leq 0.8545) \\ -5.076 + \sqrt{2.484 - 506.25[\log(e)]^2} & (0.8545 < e \leq 1.17) \\ -98.409 \log(e) + 2.0 & (1.17 < e \leq 1.674) \\ -39.8 \log(e) - 11.12 & (1.674 < e) \end{cases} \quad (57)$$

where $e = St'/St'_{\text{peak}}$. The peak scaled level shape curve G_2 depends on Reynolds number and angle and is (see figs. 88 and 89)

$$G_2(d) = \begin{cases} 77.852 \log(d) + 15.328 & (d \leq 0.3237) \\ 65.188 \log(d) + 9.125 & (0.3237 < d \leq 0.5689) \\ -114.052[\log(d)]^2 & (0.5689 < d \leq 1.7579) \\ -65.188 \log(d) + 9.125 & (1.7579 < d \leq 3.0889) \\ -77.852 \log(d) + 15.328 & (3.0889 < d) \end{cases} \quad (58)$$

where $d = R_c/(R_c)_0$ and the reference Reynolds number is

$$(R_c)_0 = \begin{cases} 10^{0.215\alpha_s + 4.978} & (\alpha_s \leq 3.0) \\ 10^{0.120\alpha_s + 5.263} & (3.0 < \alpha_s) \end{cases} \quad (59)$$

The angle-dependent level for the shape curve is

$$G_3(\alpha_s) = 171.04 - 3.03\alpha_s \quad (60)$$

5.2.3. Comparison With Data

The spectral predictions from the above equations are compared with the untripped BL airfoil noise data in figures 44 to 74. The great sensitivity of this mechanism to angle and velocity change can be clearly seen. In many respects the prediction agreement in shape, level, and actual occurrence of LBL-VS noise is good. Also as indicated in the last section, the combined contributions of LBL-VS, TBL-TE, and separation noise are important to the total predictions for this untripped BL airfoil data.

5.3. Tip Vortex Formation Noise

The prediction method proposed in this section for tip vortex formation noise is that developed by Brooks and Marcolini (ref. 18). The study isolated this high-frequency broadband self-noise by comparing aerodynamic and acoustic test results of both two-dimensional (2D) and three-dimensional (3D)

airfoil models shown in figures 2 and 3, respectively. The premise of the tip noise determination method was that 3D models produce both tip noise and TBL-TE noise, while the 2D models produce only the latter. The study produced a prediction method in general agreement with the physical model of the mechanism first proposed by George, Najjar, and Kim (ref. 17). The noise is associated with the turbulence in the locally separated flow region at the tip of a lifting blade, where the tip vortex is formed. The flow field is illustrated in figure 90 for an airfoil blade tip at an angle of attack α_{TIP} to the flow of velocity U . The flow over the blade tip consists of a vortex of strength Γ with a thick viscous core whose spanwise extent at the TE is ℓ . The recirculating flow within the core is highly turbulent. The mechanism of noise production is taken to be TE noise due to the passage of this turbulence over the edge and into the wake.

5.3.1. Calculation Procedures

The tip vortex formation noise spectrum in a 1/3-octave presentation is predicted by

$$SPL_{TIP} = 10 \log \left(\frac{M^2 M_{max}^3 \ell^2 \bar{D}_h}{r_e^2} \right) - 30.5(\log St'' + 0.3)^2 + 126 \quad (61)$$

The Strouhal number is

$$St'' = \frac{f \ell}{U_{max}} \quad (62)$$

The directivity function \bar{D}_h is given by equation (B1) in appendix B. The second term on the right side of equation (61), which gives the frequency dependence, is a parabolic fit about a peak Strouhal number of 0.5. The spanwise extent at the TE of the separation due to the tip vortex is, for the tested rounded tip,

$$\ell/c \approx 0.008 \alpha_{TIP} \quad (63)$$

where c is the chord length and α_{TIP} (see discussion below) is the angle of attack of the tip region to the oncoming flow. The maximum Mach number M_{max} of the flow within or about the separated flow region at the trailing edge is

$$M_{max}/M \approx (1 + 0.036 \alpha_{TIP}) \quad (64)$$

where M is the Mach number of the oncoming flow to the airfoil tip region. The velocity corresponding to M_{max} is

$$U_{max} = c_o M_{max} \quad (65)$$

Note that in the use of equations (63) and (64) to determine ℓ and M_{max} , α_{TIP} is correctly regarded as the actual angle of attack of the tip to the oncoming flow when the blade under consideration has a large aspect ratio (large span), is untwisted, and encounters uniform flow over its span. This is the reference case in reference 18. When the tip loading characteristics differ from those for the reference case, such as for some rotor and propeller blades, α_{TIP} must be redefined according to computed sectional loading. The redefined α'_{TIP} is

$$\alpha'_{TIP} = \left[\left(\frac{\partial L'/\partial y}{(\partial L'/\partial y)_{ref}} \right)_{y \rightarrow TIP} \right] \alpha_{TIP} \quad (66)$$

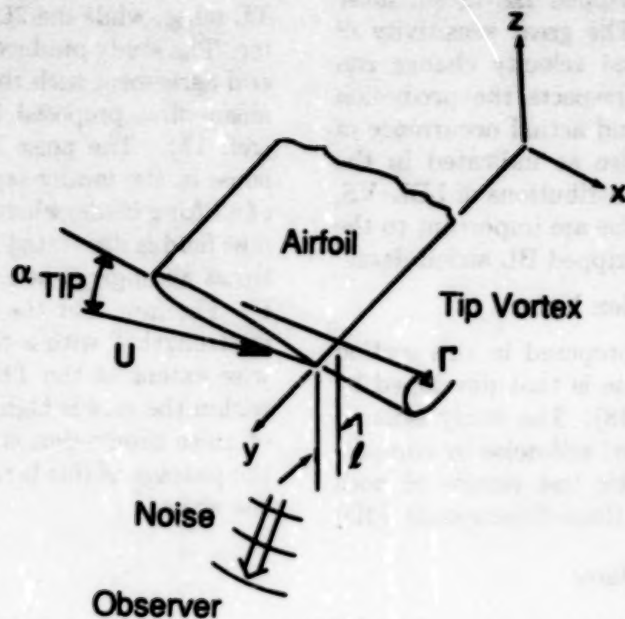


Figure 90. Formation of tip vortex.

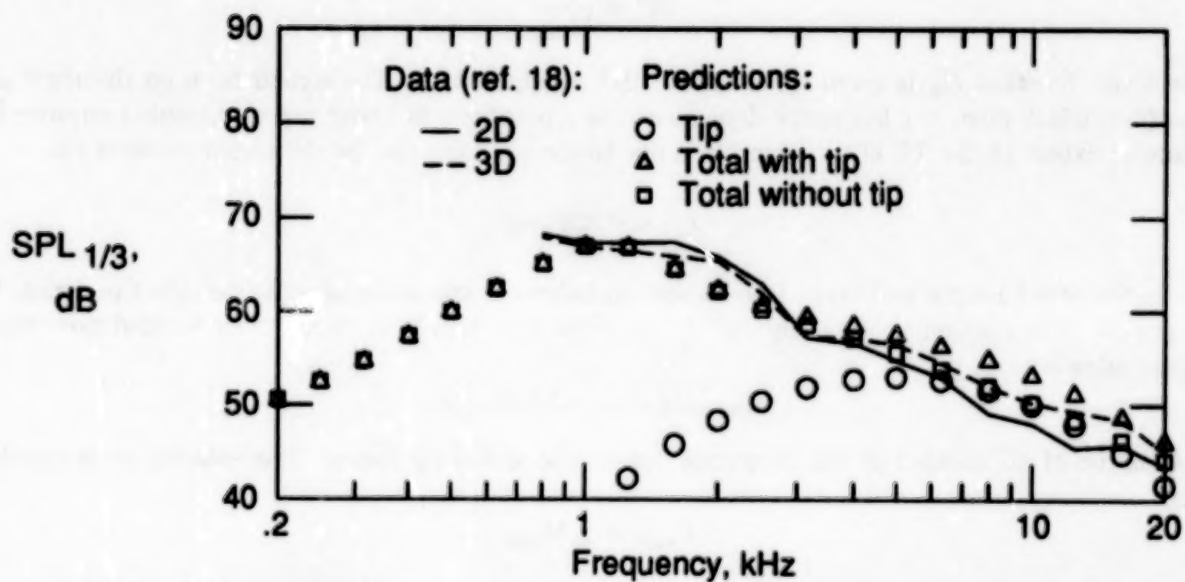


Figure 91. Noise spectra of a 3D 15.24-cm-chord airfoil with a span of 30.48 cm, and that of a 2D airfoil section where levels have been adjusted to match the same span. $U = 71.3$ m/s, $\alpha_t = 10.8^\circ$.

where α_{TIP} is the geometric angle and L' is the lift per unit span at the spanwise position y . The sectional lift slope $\partial L'/\partial y$ near the tip is taken to be proportional to the tip vortex strength Γ (of fig. 90). When tip loading is found to be high, the predicted tip noise levels increase. The use of α'_{TIP} rather than α_{TIP} in equations (63) and (64) generalizes the solution for arbitrary aspect ratios, blade twist, and spanwise flow variations. Reference 18 contains examples which provide guidance in the evaluation of equation (66) for aspect ratio, as well as tunnel testing effects.

The tip noise prediction equations are based on data from airfoils with rounded blade tips. Of interest is a flat (square-off or cut-off) tip geometry which reference 8 considered, along with rounded tips, in calculations employing limited tip flow measurements reported in the literature. The different tip geometries required a different definition of the separated flow region size ℓ . In applying the prediction equations of the present paper for flat tips, it does not appear appropriate to use the definition of reference 8. The constants in equation (61) reflect the definition of ℓ in equation (63). The measurements did not confirm the definition of ℓ for rounded tips proposed by reference 8. For consistency, the following definition for ℓ is proposed for flat tips for the present prediction equations:

$$\ell/c = \begin{cases} 0.0230 + 0.0169\alpha'_{TIP} & (0^\circ \leq \alpha'_{TIP} \leq 2^\circ) \\ 0.0378 + 0.0095\alpha'_{TIP} & (2^\circ < \alpha'_{TIP}) \end{cases} \quad (67)$$

This definition of ℓ approximately accounts for differences between the definition of reference 8 and that of equation (63) for rounded tips. There is at present no experimental confirmation of equation (67).

5.3.2. Comparison With Data

Noise data from reference 18 (fig. 7) are presented in figure 91 along with predictions of tip noise and the combined contributions of TBL-TE and separation noise. The rounded tip 3D model has a chord of 15.24 cm and a span of 30.5 cm. The corresponding 2D model has a span of 45.7 cm so its noise spectrum levels in the figure were adjusted downward by 1.8 dB (based on a $10 \log(L)$ dependency) to obtain that expected for a 30.5-cm span. The difference between the 2D and 3D spectra should be that due to tip noise. The predictions in figure 91 for TBL-TE and separation noise, which employed the angle $\alpha_s = 0.5(10.8^\circ)$ to account for the wind tunnel correction, should ideally match the 2D model spectrum. The tip noise prediction adds to the prediction to obtain a total which should match the 3D model spectrum. The tip noise prediction involved the use of equation (66) because of the finite extent of the span as well as open wind tunnel influences. Based on the lift distributions presented in reference 18, the tip angle becomes $\alpha'_{TIP} = 0.71(10.8^\circ)$. While a slight overprediction at higher frequencies is seen in figure 91 for this particular example, the differences between levels with and without tip noise are the same for both data and prediction. The comparison shows consistency and compatibility not only with the data but also between the self-noise prediction methods.

5.4. Trailing-Edge-Bluntness-Vortex-Shedding Noise

In this section, the experiment of reference 2 is briefly described, published and previously unpublished TE bluntness noise data from the study are presented, and a prediction method is developed.

5.4.1. Experiment

The Brooks-Hodgson experiment (ref. 2) employed an experimental arrangement similar to that reported in section 2 of the present paper with respect to hardware and acoustic measurement. However, in reference 2, the model airfoil tested was large with a 60.96-cm chord length. When BL tripping was used, 2.0-cm-wide strips of No. 40 grit were applied at 15 percent of the chord. Rather than the TE being sharp, the model TE thickness, or bluntness, was $h = 2.5$ mm. Figure 92 shows the TE region of the airfoil. The TE geometry was rounded at the two edges and flat between the rounded edge portions, which each comprised about one-third of the 2.5-mm thickness. The thickness h was varied, with edges of similar geometry, by alternately attaching extensions on the edge, as illustrated in figure 92(a). Also tested were sharp-edge ($h = 0$) plate extensions 15.24 and 30.48 cm long, as shown in figure 92(b). Another sharp-edge extension (not shown) was a 2.54-cm-long "flap" extension placed at 17.5° off the chord mean axis at the trailing edge. In addition, blunt plate extensions were tested which were 15.24 cm long with

$h = 2.5$ and 4.8 mm and 30.48 cm long with $h = 4.8$ mm. These extensions with rounded TE corners are shown in figure 92(c). Tape, 0.08 mm thick, was used to provide a smooth surface transition from the airfoil to the extensions.

Presented in figure 93, from reference 2, are power spectral noise data of the airfoil at four flow velocities. The airfoil is at zero angle of attack and the boundary layers are tripped. The microphone observer position is $r_e = 1.22$ m and $\Theta_e = 90^\circ$ with respect to the model trailing edge. For two speeds, the spectra are given for the four TE thicknesses of figure 92(a). The spectral results for the sharp, $h = 0$, TE cases should be all due to TBL-TE noise. The bluntness contributes additively at high frequencies to the spectrum levels. The values given for h/δ^* in figure 93 differ slightly from those specified in reference 2 because δ^* here is calculated from the BL thickness scaling equations of the present paper. Data are presented in reference 2 for the sharp geometries of figure 92(b), as well as the mentioned 17.5° sharp flap extension. These geometries give essentially the same spectra as the sharp extension of figure 92(a). This demonstrates that TBL-TE noise is rather invariant with regard to geometry changes in the edge region, as long as the TE is sharp and the boundary layers are substantially the same.

Trailing-edge bluntness noise spectra in a smoothed 1/3-octave format are presented in figure 94 for the edge geometries of figures 92(a) and 92(c). These spectra are the result of a spectral subtraction process between the total spectra and the corresponding sharp TE spectra and should thus represent the bluntness contribution only. With the exception of the eight spectra also represented in figure 93, the data have not been previously published. The indicated values of h/δ^* for the extensions are based on calculations of δ^* for the TE of the airfoil without the extensions. This is justified by indications that the boundary layers did not substantially change over the zero pressure gradient extension plates due to the influence of the upstream adverse pressure gradient (ref. 2). The spectrum for the airfoil with $h = 2.5$ mm and $h/\delta^* = 1.15$ in figure 94 is for naturally transitional boundary layers; all others are for tripped boundary layers.

5.4.2. Scaled Data

The spectra of figure 94, as well as limited frequency data of Blake (ref. 19), form the foundation of the scaling approach. As with the scaling approach for TBL-TE and LBL-VS noise, the level, frequency, and spectral shape are modeled as functions of flow and geometric parameters. For the level and frequency definition, we chose the peak of the

spectral humps as the reference. The peak value of Strouhal number, defined as

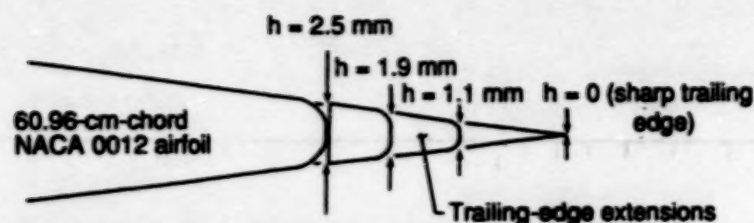
$$St_{peak}^w = \frac{f_{peak} h}{U} \quad (68)$$

is plotted versus the thickness ratio h/δ^* in figure 95. The Strouhal numbers increase with increases in thickness ratio. The Strouhal numbers for the plate extensions of figure 92(c) are uniformly higher, for the same thickness ratios, than for the edge extensions of figure 92(a). Also shown are two results obtained from Blake (ref. 19). Blake presents surface pressure data for a large array of plate edge geometries—all for very large values of h/δ^* (with the exception of the ref. 2 data reported and the one case shown in fig. 95 at $h/\delta^* = 5.19$). Blake, for most data, employed Strouhal relationships which depend on special wake stream thicknesses, and convection velocities not available without measurements. From Blake, however, it is obvious that different TE geometries have different frequency dependences, consistent with the result of figure 95 that Strouhal numbers for the flat plate extension and the airfoil TE geometries differ. The primary difference between the geometries is that the NACA 0012 airfoil has a beveled or sloping surface upstream of the trailing edge with a solid angle Ψ of 14° and the flat plate has $\Psi = 0^\circ$. The result shown from Blake in figure 95 at $h/\delta^* = 5.19$ is for a plate with $\Psi = 12.5^\circ$ and nonrounded TE corners. In figure 95, parallel curves are fitted to the data. The curves, designated with values of Ψ , are defined on the basis of a match point at $h/\delta^* = 20$ for $\Psi = 0^\circ$. From Blake's scaling for a thick flat plate (h/δ^* large) with nonrounded TE corners, one can determine that $f h/U = 0.21$ at $h/\delta^* = 20$. The curve for $\Psi = 14^\circ$ intercepts Blake's $\Psi = 12.5^\circ$ result, but this is deemed an acceptable deviation from the curve fit. For scaling purposes, values of St_{peak}^w for Ψ values other than 0° and 14° could be determined by linear interpolation as described in the calculation procedure section to follow.

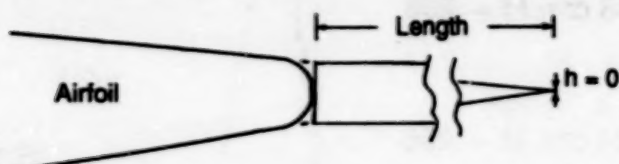
For amplitude scaling, the peak values of the 1/3-octave spectra of figure 94 were normalized as

$$\text{Scaled peak } SPL_{1/3} = \text{Peak } SPL_{1/3} - 10 \log \left(\frac{M^{5.5} h L}{r_e^2} \right) \quad (69)$$

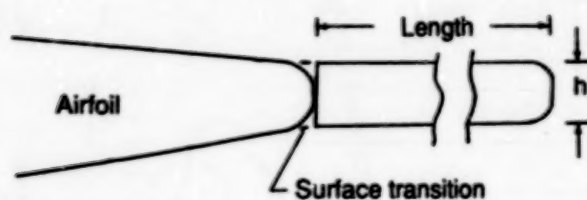
The 5.5 power for Mach number dependence was determined to give better overall scaling success than either a 5 or 6 power. Figure 96 shows the scaled levels plotted versus the thickness ratio h/δ^* . As in figure 95 for the Strouhal dependency, the scaled levels are uniformly higher for the plates than for the



(a) TE Extensions, Which are Alternately Attached



(b) Sharp Edge Plates



(c) Blunt Edge Plates

Figure 92. Illustration of trailing-edge extensions and plates. Smooth surface transition is provided for all geometries.

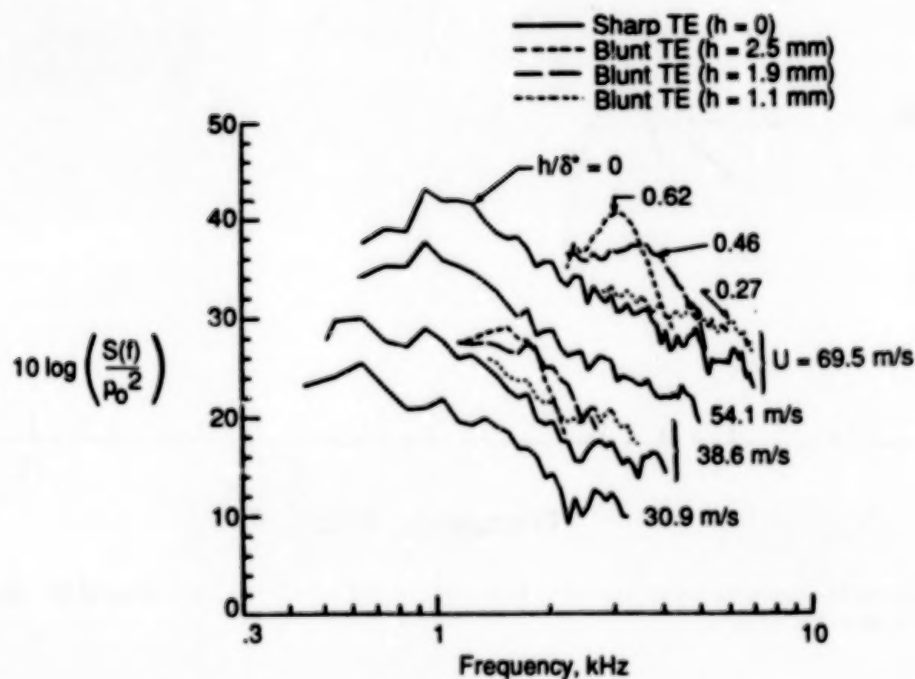


Figure 93. Spectral density for TE noise for 60.96-cm-chord airfoil with various degrees of TE bluntness. Tripped BL; $\alpha_l = 0^\circ$; $\theta_e = 90^\circ$. Level referenced to 1-Hz bandwidth. Data from reference 2.

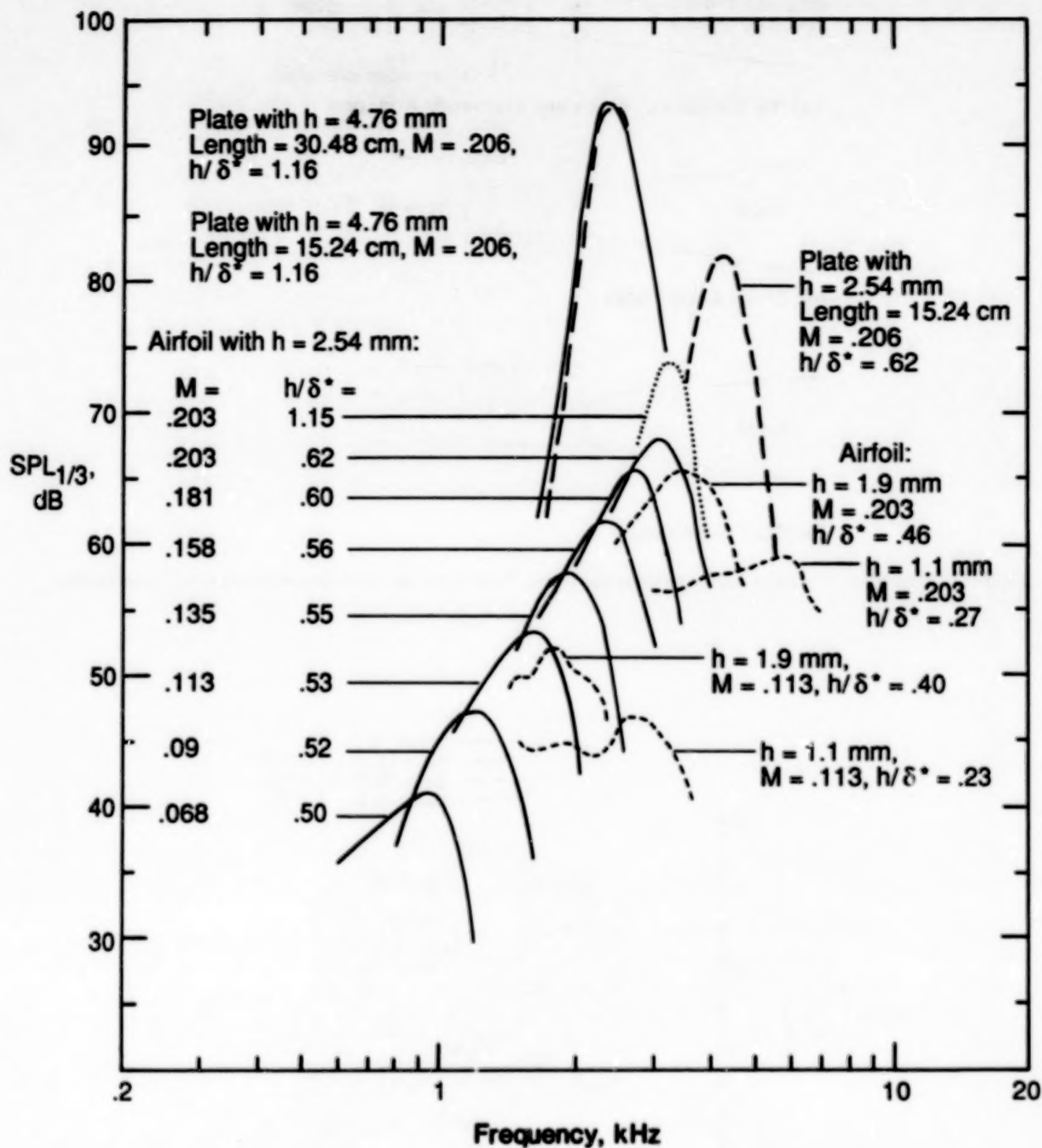


Figure 94. TE-bluntness-vortex-shedding noise, extracted from data of figure 93, data for untripped BL, and data with plate extensions (fig. 92(c)) attached.

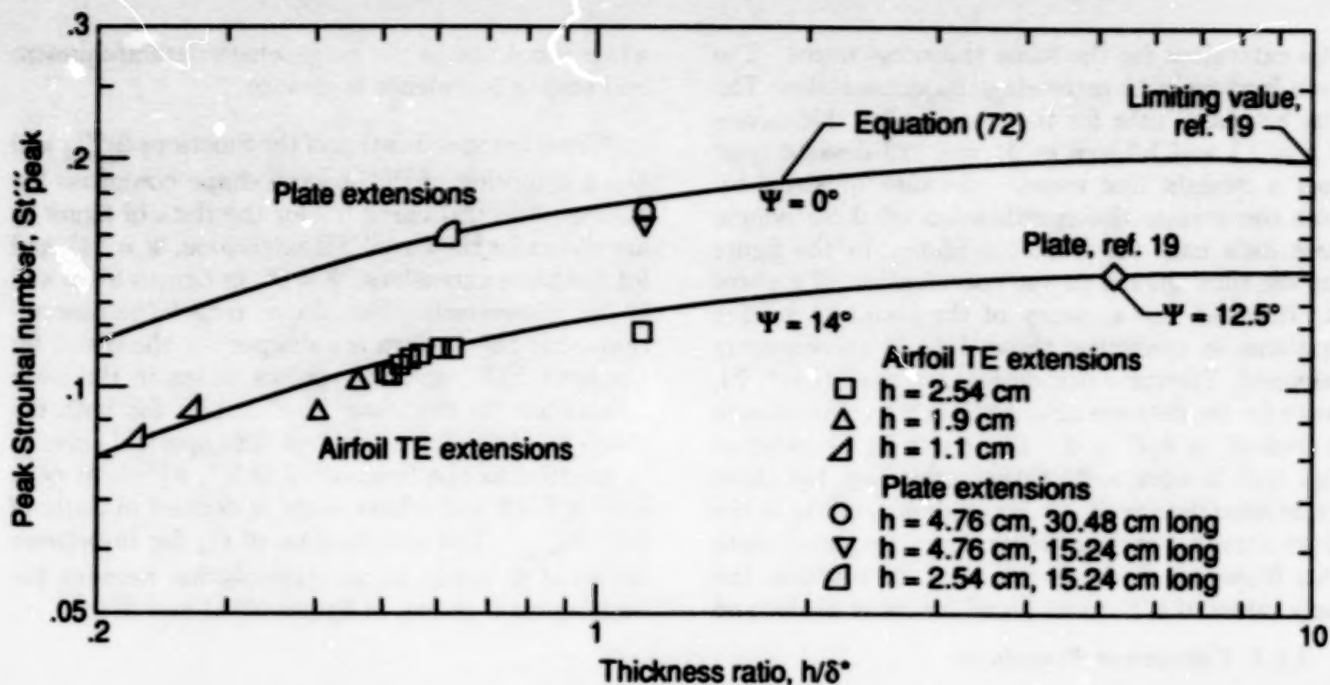


Figure 95. Peak Strouhal number for bluntness noise versus thickness ratio h/δ^* determined from figure 94 and Blake (ref. 19).

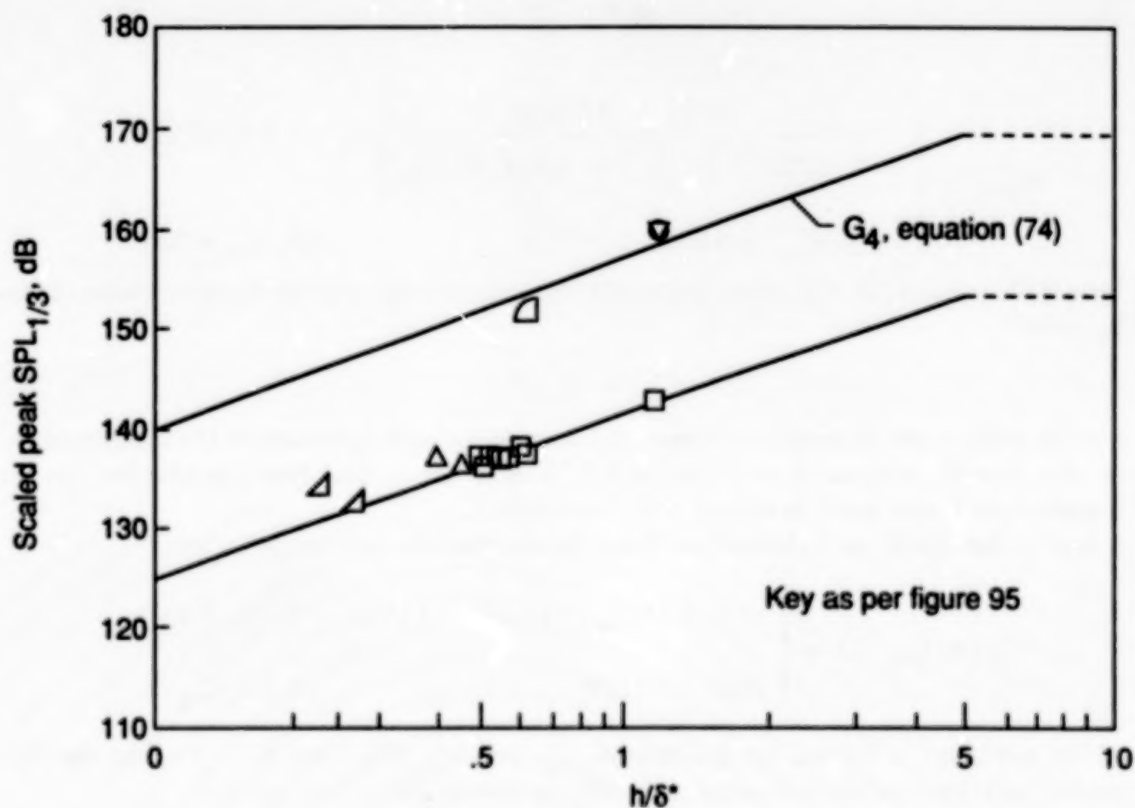


Figure 96. Peak scaled levels for bluntness noise versus thickness ratio h/δ^* determined from figure 94.

edge extensions for the same thickness ratios. The levels increase with increasing thickness ratios. The edge extension data for the two smaller thicknesses of $h = 1.1$ and 1.9 mm at $M = 0.113$ deviate most from a straight line trend. Because of signal-to-noise concerns in the specification of these points, these data have the least confidence in the figure and are thus ignored in the specification of a curve fit. However, the accuracy of the resultant scaling equations in predicting these data is subsequently examined. The curve fits, designated as $G_4(h/\delta^*, \Psi)$, shown for the data are straight lines which are chosen to level off at $h/\delta^* = 5$. The curve fit behavior at high h/δ^* is admittedly rather arbitrary, but there are no noise data available for guidance, unlike in the above Strouhal scaling where some frequency data from Blake are used. Fortunately, in practice, the likely values of h/δ^* to be found for rotor blades and

wings should be in the range where data are present and scaling confidence is greatest.

Given the specification of the functions St_{peak}''' and G_4 , a definition of the spectral shape completes the scaling. Spectral curve fits for the data of figure 94 are shown for the airfoil TE extensions, $\Psi = 14^\circ$, and for the plate extensions, $\Psi = 0^\circ$, in figures 97(a) and 97(b), respectively. The shapes reflect the observations that the spectra are sharper for the plates for the same h/δ^* , and the spectra widen in the lower frequencies for decreased h/δ^* values for both the plates and the edge extensions. The spectral curve fit is specified as the function $G_5(h/\delta^*, \Psi)$ whose peak level is 0 dB and whose shape is defined in terms of St'''/St_{peak}''' . The specification of G_5 for in-between values of Ψ would be an interpolation between the limiting cases shown in figures 97(a) and 97(b).

5.4.3. Calculation Procedures

The TE bluntness noise spectrum in a 1/3-octave presentation is predicted by

$$SPL_{BLUNT} = 10 \log \left(\frac{h M^{5.5} L \bar{D}_h}{r_e^2} \right) + G_4 \left(\frac{h}{\delta_{avg}^*}, \Psi \right) + G_5 \left(\frac{h}{\delta_{avg}^*}, \Psi, \frac{St'''}{St_{peak}'''} \right) \quad (70)$$

The directivity function \bar{D}_h is given by equation (B1) in appendix B. The Strouhal definitions are (see fig. 95)

$$St''' = \frac{f h}{U} \quad (71)$$

and

$$St_{peak}''' = \begin{cases} \frac{0.212 - 0.0045\Psi}{1 + 0.235 (h/\delta_{avg}^*)^{-1} - 0.0132 (h/\delta_{avg}^*)^{-2}} & (0.2 \leq h/\delta_{avg}^*) \\ 0.1(h/\delta_{avg}^*) + 0.095 - 0.00243\Psi & (h/\delta_{avg}^* < 0.2) \end{cases} \quad (72)$$

The h/δ_{avg}^* term is the ratio of TE thickness (degree of bluntness) h to the average boundary-layer displacement thickness δ_{avg}^* , where

$$\delta_{avg}^* = \frac{\delta_p^* + \delta_s^*}{2} \quad (73)$$

The angle Ψ is the solid angle, in degrees, between the sloping surfaces upstream of the trailing edge. For an edge on a flat plate $\Psi = 0^\circ$, whereas $\Psi = 14^\circ$ for an NACA 0012 airfoil. The determination for this parameter for other TE geometries is discussed in section 6 and appendix C.

The peak level of the spectrum is determined from the function G_4 (see fig. 96) where

$$G_4 \left(\frac{h}{\delta_{avg}^*}, \Psi \right) = \begin{cases} 17.5 \log \left(\frac{h}{\delta_{avg}^*} \right) + 157.5 - 1.114\Psi & (h/\delta_{avg}^* \leq 5) \\ 169.7 - 1.114\Psi & (5 < h/\delta_{avg}^*) \end{cases} \quad (74)$$

The shape of the spectrum is defined by the function G_5 (see figs. 97(a) and 97(b)) where the calculation procedure involves an interpolation between the spectra for $\Psi = 0^\circ$ and 14° as follows:

$$G_5 \left(\frac{h}{\delta_{avg}^*}, \Psi, \frac{St'''}{St_{peak}'''} \right) = (G_5)_{\Psi=0^\circ} + 0.0714\Psi [(G_5)_{\Psi=14^\circ} - (G_5)_{\Psi=0^\circ}] \quad (75)$$

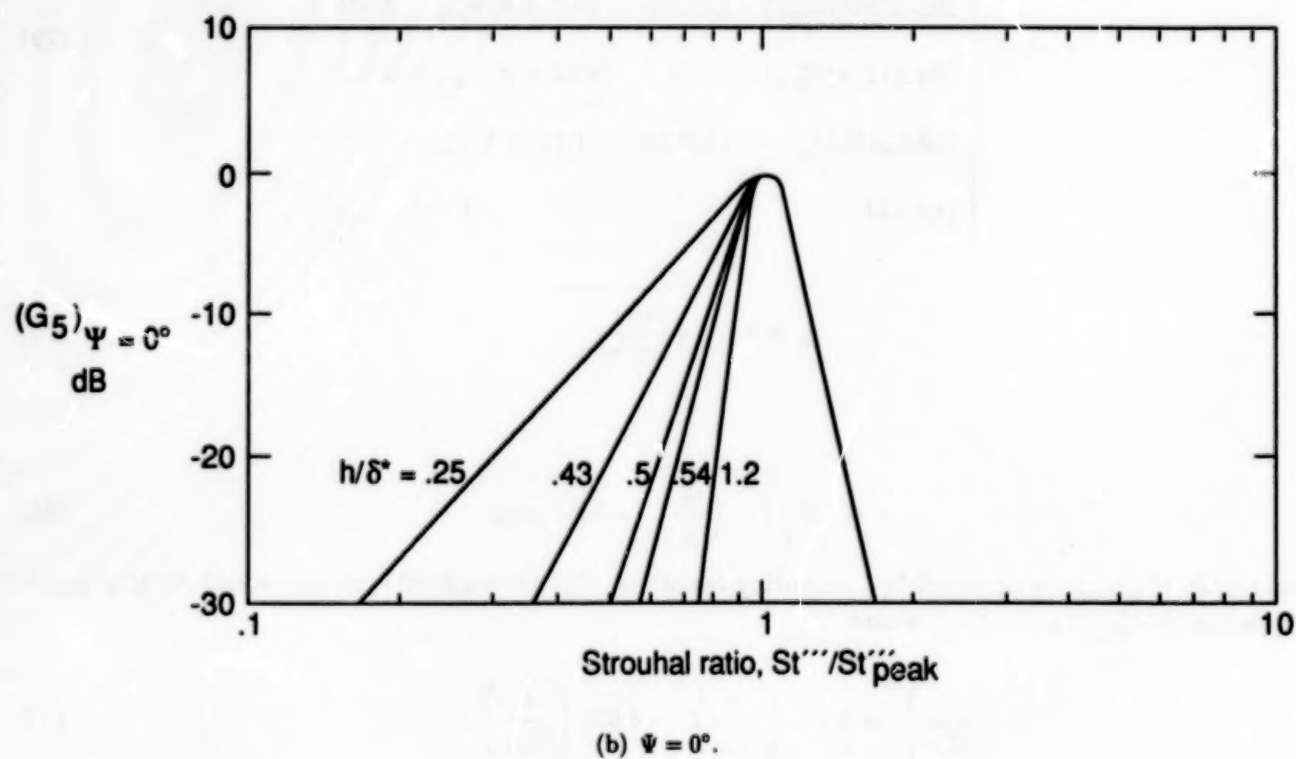
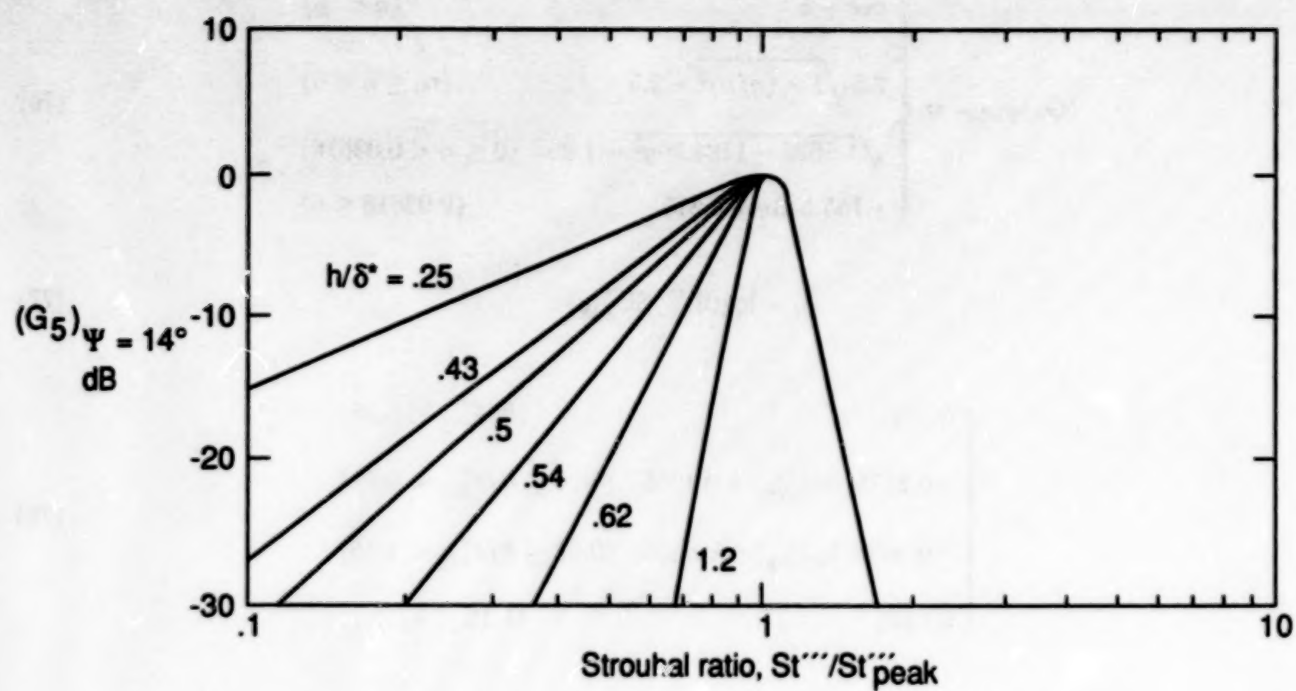


Figure 97. Spectral shape functions for TE bluntiness noise.

where

$$(G_5)_{\Psi=14^\circ} = \begin{cases} m\eta + k & (\eta < \eta_0) \\ 2.5\sqrt{1 - (\eta/\mu)^2} - 2.5 & (\eta_0 \leq \eta < 0) \\ \sqrt{1.5625 - 1194.99\eta^2} - 1.25 & (0 \leq \eta < 0.03616) \\ -155.543\eta + 4.375 & (0.03616 \leq \eta) \end{cases} \quad (76)$$

$$\eta = \log(St'''/St'''_{\text{peak}}) \quad (77)$$

$$\mu = \begin{cases} 0.1221 & (h/\delta_{\text{avg}}^* < 0.25) \\ -0.2175(h/\delta_{\text{avg}}^*) + 0.1755 & (0.25 \leq h/\delta_{\text{avg}}^* < 0.62) \\ -0.0308(h/\delta_{\text{avg}}^*) + 0.0596 & (0.62 \leq h/\delta_{\text{avg}}^* < 1.15) \\ 0.0242 & (1.15 \leq h/\delta_{\text{avg}}^*) \end{cases} \quad (78)$$

$$m = \begin{cases} 0 & (h/\delta_{\text{avg}}^* \leq 0.02) \\ 68.724(h/\delta_{\text{avg}}^*) - 1.35 & (0.02 < h/\delta_{\text{avg}}^* \leq 0.5) \\ 308.475(h/\delta_{\text{avg}}^*) - 121.23 & (0.5 < h/\delta_{\text{avg}}^* \leq 0.62) \\ 224.811(h/\delta_{\text{avg}}^*) - 69.35 & (0.62 < h/\delta_{\text{avg}}^* \leq 1.15) \\ 1583.28(h/\delta_{\text{avg}}^*) - 1631.59 & (1.15 < h/\delta_{\text{avg}}^* < 1.2) \\ 268.344 & (1.2 < h/\delta_{\text{avg}}^*) \end{cases} \quad (79)$$

$$\eta_0 = -\sqrt{\frac{m^2\mu^4}{6.25 + m^2\mu^2}} \quad (80)$$

and

$$k = 2.5\sqrt{1 - \left(\frac{\eta_0}{\mu}\right)^2} - 2.5 - m\eta_0 \quad (81)$$

The spectrum $(G_5)_{\Psi=0^\circ}$ is obtained by computing equations (76) through (81), as one would for $(G_5)_{\Psi=14^\circ}$, but replacing $(h/\delta_{\text{avg}}^*)$ by $(h/\delta_{\text{avg}}^*)'$ where

$$\left(\frac{h}{\delta_{\text{avg}}^*}\right)' = 6.724\left(\frac{h}{\delta_{\text{avg}}^*}\right)^2 - 4.019\left(\frac{h}{\delta_{\text{avg}}^*}\right) + 1.107 \quad (82)$$

5.4.4. Comparison With Data

Noise spectra for the airfoil with different TE thicknesses (geometry of fig. 92(a)) are presented for the flow Mach numbers of $M = 0.21$ and 0.12 in figures 98 and 99, respectively. The data were obtained by digitizing the spectra of figure 93 and converting these to 1/3-octave levels. The prediction curves shown are those of TBL-TE and bluntness noise sources. For the sharp TE of figures 98(a)

and 99(a), there is no bluntness contribution. Overprediction is seen for the TBL-TE noise at the lowest frequencies and some underprediction is apparent in the higher frequencies for the highest flow speed. For the nonzero TE thicknesses the bluntness noise contributes to the total spectra at high frequencies and renders good comparisons with the data. Good agreement is found even for the aforementioned smaller thickness cases at low Mach number (figs. 99(c) and 99(d)).

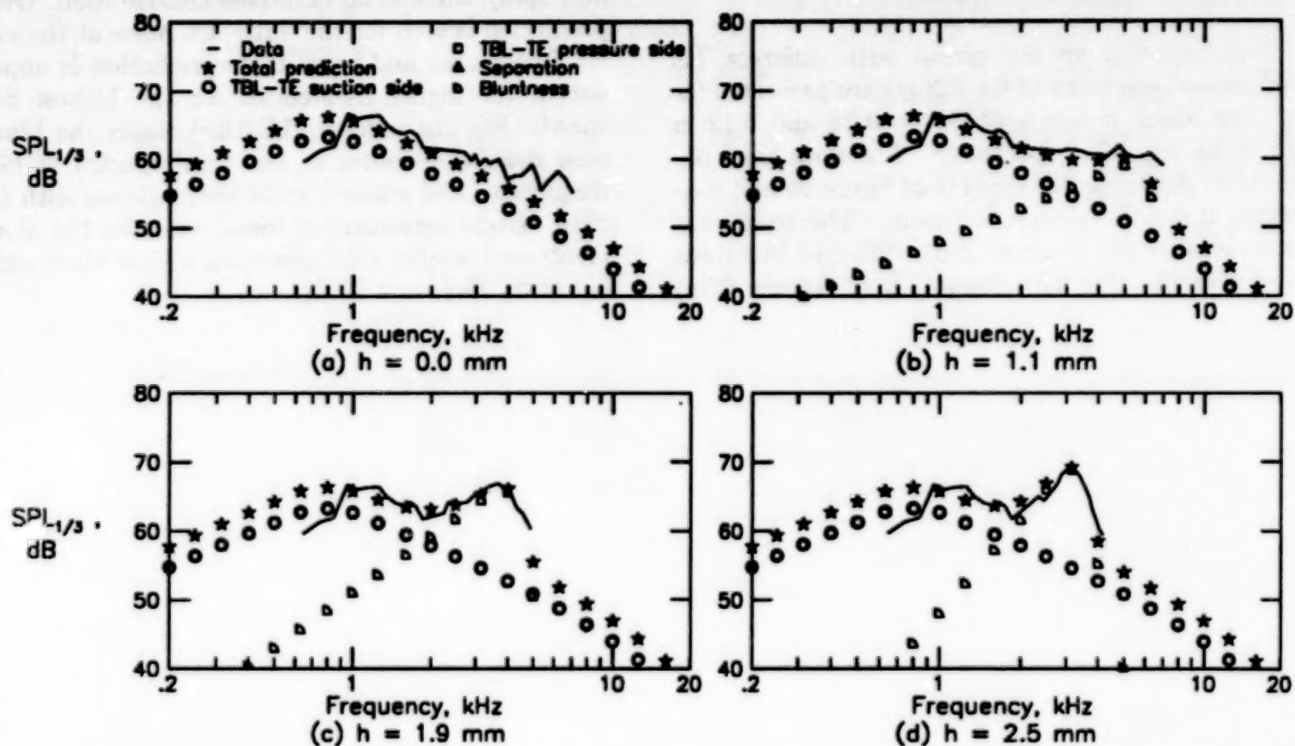


Figure 98. One-third-octave presentation of spectra of figure 93 at $U = 69.5$ m/s with predictions for various degrees of bluntness.

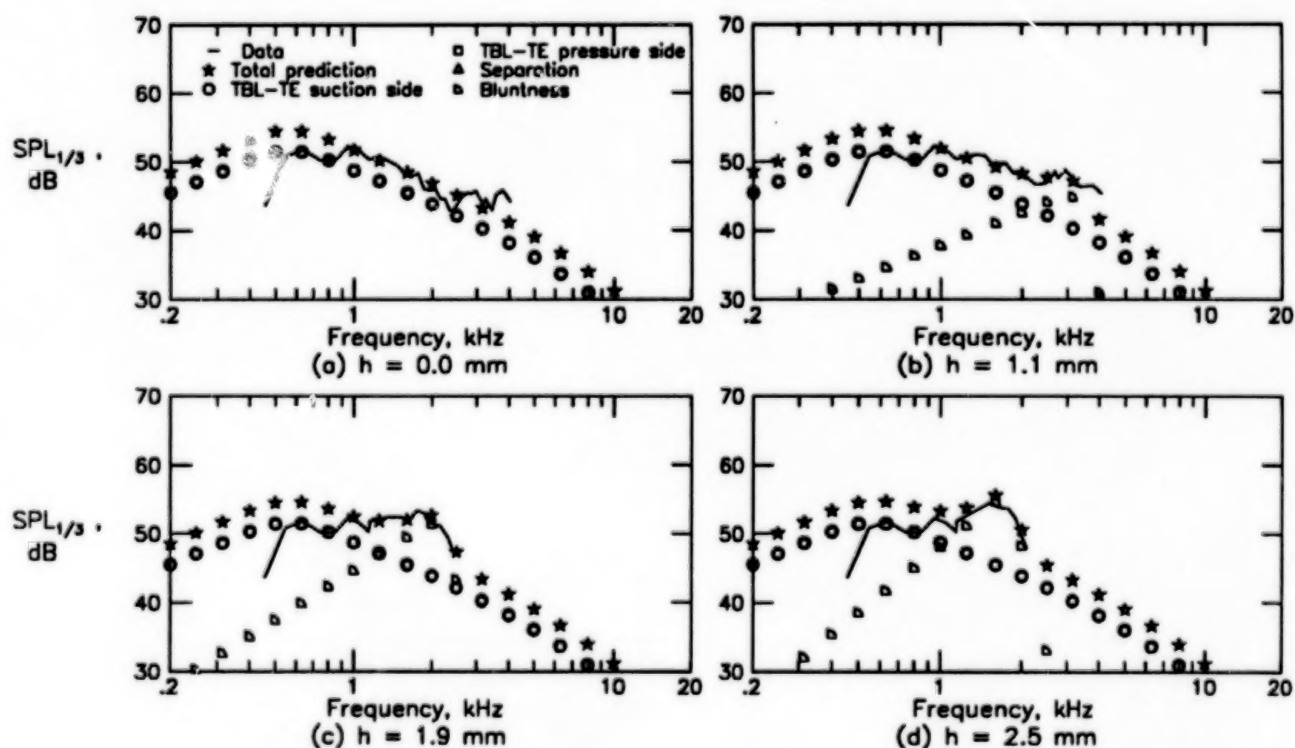


Figure 99. One-third-octave presentation of spectra of figure 93 at $U = 38.6$ m/s with predictions for various degrees of bluntness.

6. Comparison of Predictions With Published Results

The scaling law predictions are compared in this section with data from self-noise studies of airfoil sections performed at the United Technologies Research Center (UTRC).

6.1. Study of Schlinker and Amiet

Schlinker and Amiet (ref. 3) conducted tests in the UTRC Acoustic Research Tunnel to study TBL-TE noise from a cambered helicopter blade section. The cross section of the 40.6-cm-chord and 53.3-cm-span model is shown in figure 100. As in the present NASA Langley studies, the model was mounted on sidewalls and spanned the width of the open tunnel jet, so that the flow across the model was two-dimensional. The nozzle providing the flow had a rectangular exit of dimensions of 29 cm \times 53.3 cm. To isolate the TBL-TE noise from facility background noise, a directional microphone system was used. The experimental configuration, illustrating the shear layer refraction effect on the TE noise received by the directional microphone, is shown in figure 101. The Mach numbers tested ranged from 0.1 to 0.5 and the tunnel angle of attack α_t varied from -0.4° (zero lift for this cambered airfoil) to 12° .

6.1.1. Boundary-Layer Definition

Because only TBL-TE noise measurements were desired, the boundary layers were tripped by applying thin serrated aluminum tape at the blade locations indicated in figure 100. The tape thickness was on the order of the BL displacement thickness at the points of application, providing minimum surface protrusion to avoid unnaturally large TBL thicknesses downstream. This "light" trip is in contrast to the present study where the trips were "heavy" for reasons discussed.

Hot-wire measurements were made in the boundary-layer/near-wake region at the TE of the model. In figure 102, measured BL thicknesses are plotted versus Mach number for various tunnel angles of attack α_t . These data are from figure 17 of reference 3. At zero lift, $\alpha_t = -0.4^\circ$, in figure 102(a), the BL thicknesses δ_0 on the pressure and suction sides are approximately the same. This should be expected since they developed under approximately the same adverse pressure gradient. Included in figure 102(a) are corresponding values of BL displacement thicknesses, which were calculated by the present authors from velocity profiles presented in reference 3 (δ^* was not a quantity of interest in ref. 3). In figures 102(b) and 102(c), δ/c values are shown for $\alpha_t = 7.6^\circ$ and 12° , respectively. Comparing figures 102(a), 102(b),

and 102(c), one can see that as angle of attack increases, δ_s increases and δ_p decreases.

These measurements are compared with the thickness scaling equations of the present paper. First, equations (2) and (3) are used to calculate the BL thickness ratio δ_0/c and displacement thickness ratio δ_0^*/c . To make the calculations agree with the data of figure 102(a), all calculated values of δ_0/c and δ_0^*/c were multiplied by a factor 0.6. This factor is taken to be the adjustment in equations (2) and (3) needed to make them appropriate for the "light" trip of reference 3. Next, the corrected angles of attack are determined by (1) adding 0.4° to α_t so that the tunnel angle is referenced to the zero-lift case and (2) using equation (1), with $c = 40.6$ cm and $H = 79$ cm, to obtain $\alpha_s = 0^\circ, 3.9^\circ$, and 6.1° for $\alpha_t = -0.4^\circ, 7.6^\circ$, and 12° , respectively. These values of α_s are now used in equations (8) and (11) to obtain δ_p/δ_0 and δ_s/δ_0 , respectively. The resultant values of δ_s/c and δ_p/c are compared with the data in figures 102(b) and 102(c).

6.1.2. Trailing-Edge Noise Measurements and Predictions

Trailing-edge noise spectra in a 1/3-octave presentation are given in figure 103 for the airfoil at $\alpha_t = -0.4^\circ$ with Mach number ranging from $M = 0.1$ to 0.5. The data were obtained by the directional microphone system at differing orientations to the airfoil. Shear layer corrections and directional microphone gain adjustments were made so that the data shown represent the noise radiated from a unit length of $L = 0.3048$ m of the TE span, at an observer distance of $r_e = 3$ m, and an observer angle Θ_e which is specified in the figure. Figures 104 and 105 contain spectra for the airfoil at $\alpha_t = 7.6^\circ$ and 12° , respectively.

The TBL-TE and separation noise spectra were predicted using the calculation procedures of the present paper. The values of α_s , δ_s^* , and δ_p^* used were calculated as described in the previous section. Because of the BL trips and the 2D flow, no LBL-VS or tip noise calculations were made. In performing the calculations for TE bluntness noise, one has to assign values of the TE thickness h and the TE flow angle parameter Ψ . The thickness was indicated in reference 3 to be $h = 0.38$ mm but the shape of this small TE region was not given. A value of $\Psi = 17^\circ$ has been used in the prediction because it gives reasonable prediction-data comparisons.

In figures 103 to 105, the predictions are compared with the measurements. As in the presentation of figures 11 to 74, the individual noise contributions are shown, along with the total summed spectra. The prediction-data comparisons are good, especially

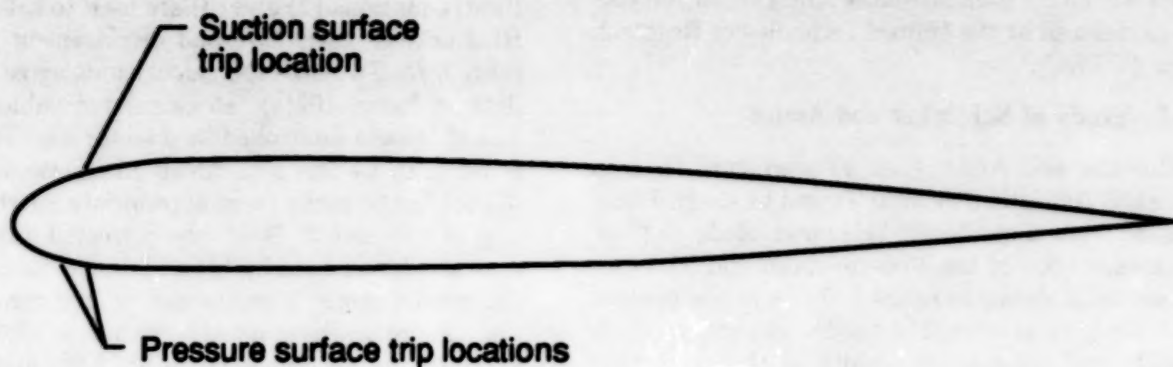


Figure 100. Cross section of Sikorsky rotor blade (ref. 3). Span is 53.3 cm and chord length is 40.6 cm.

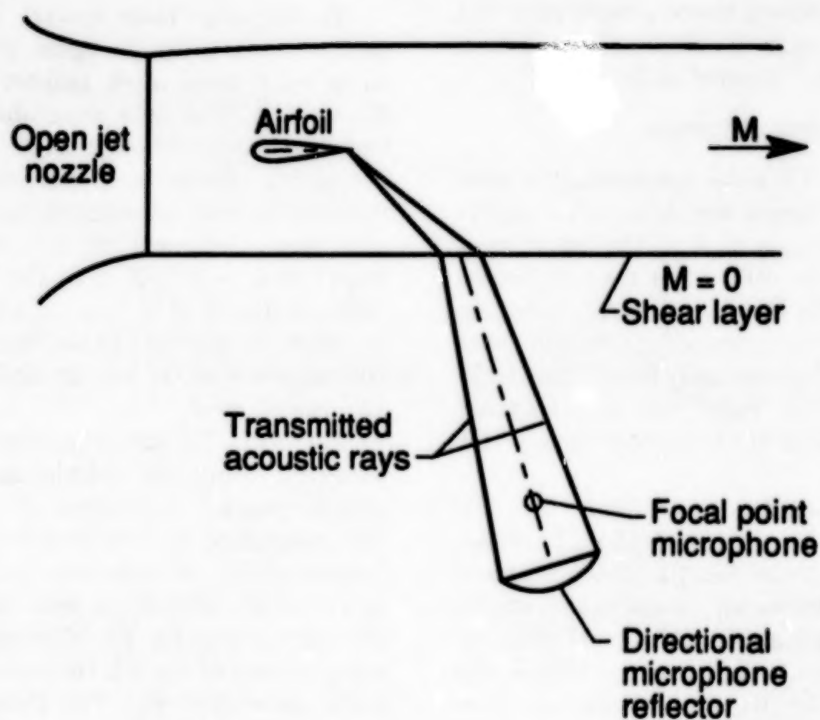


Figure 101. UTRC experimental configuration of reference 3, showing the effect of tunnel flow and shear layer refraction on the directional microphone alignment.

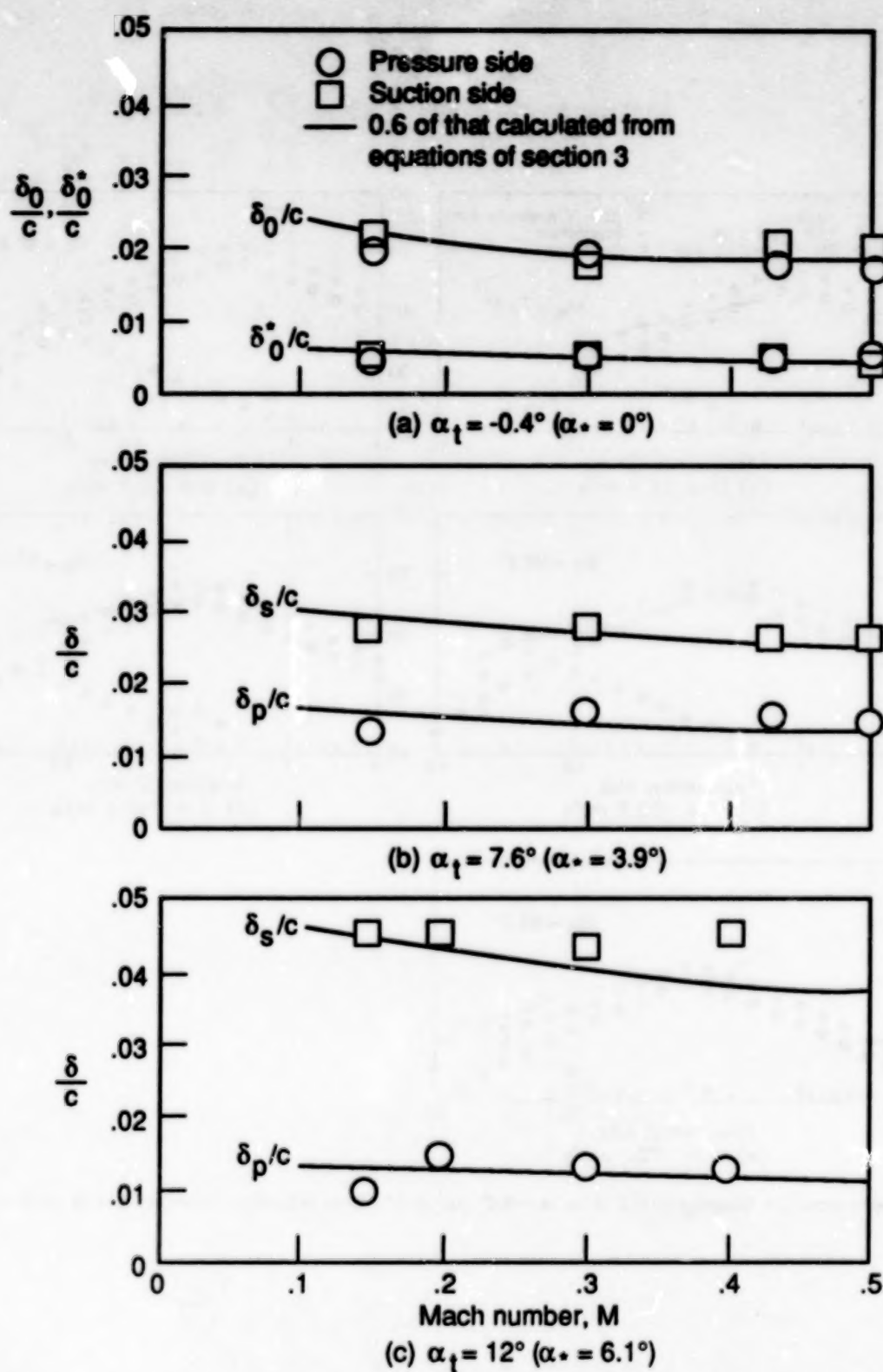


Figure 102. Measured boundary-layer thickness at the TE of the Sikorsky airfoil (ref. 3). Comparison is made with scaling equation results of present paper, multiplied by 0.6 to account for light trip condition.

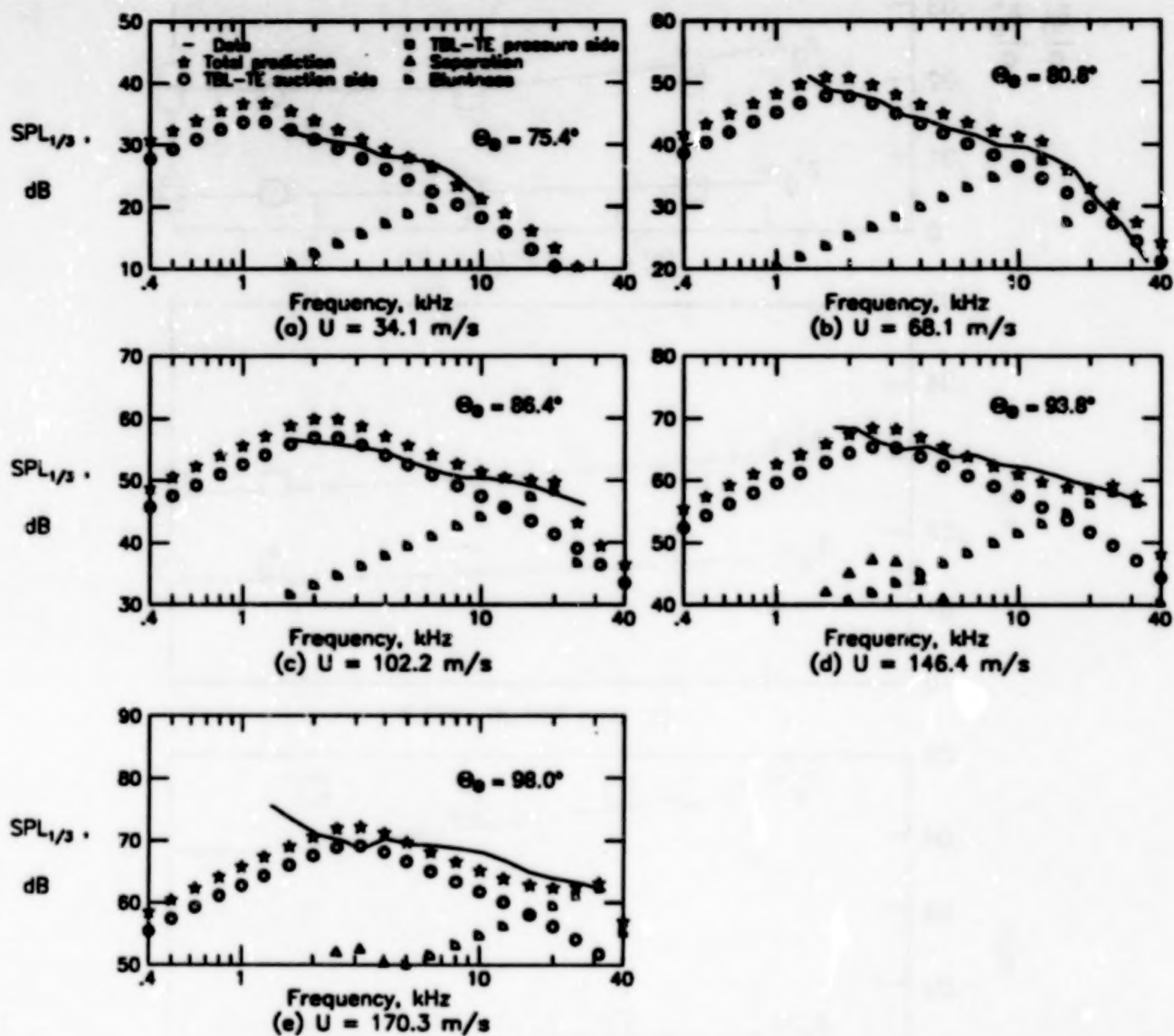


Figure 103. Noise spectra for Sikorsky airfoil at $\alpha_i = -0.4^\circ$ ($\alpha_s = 0^\circ$) from reference 3 compared with prediction of present paper.

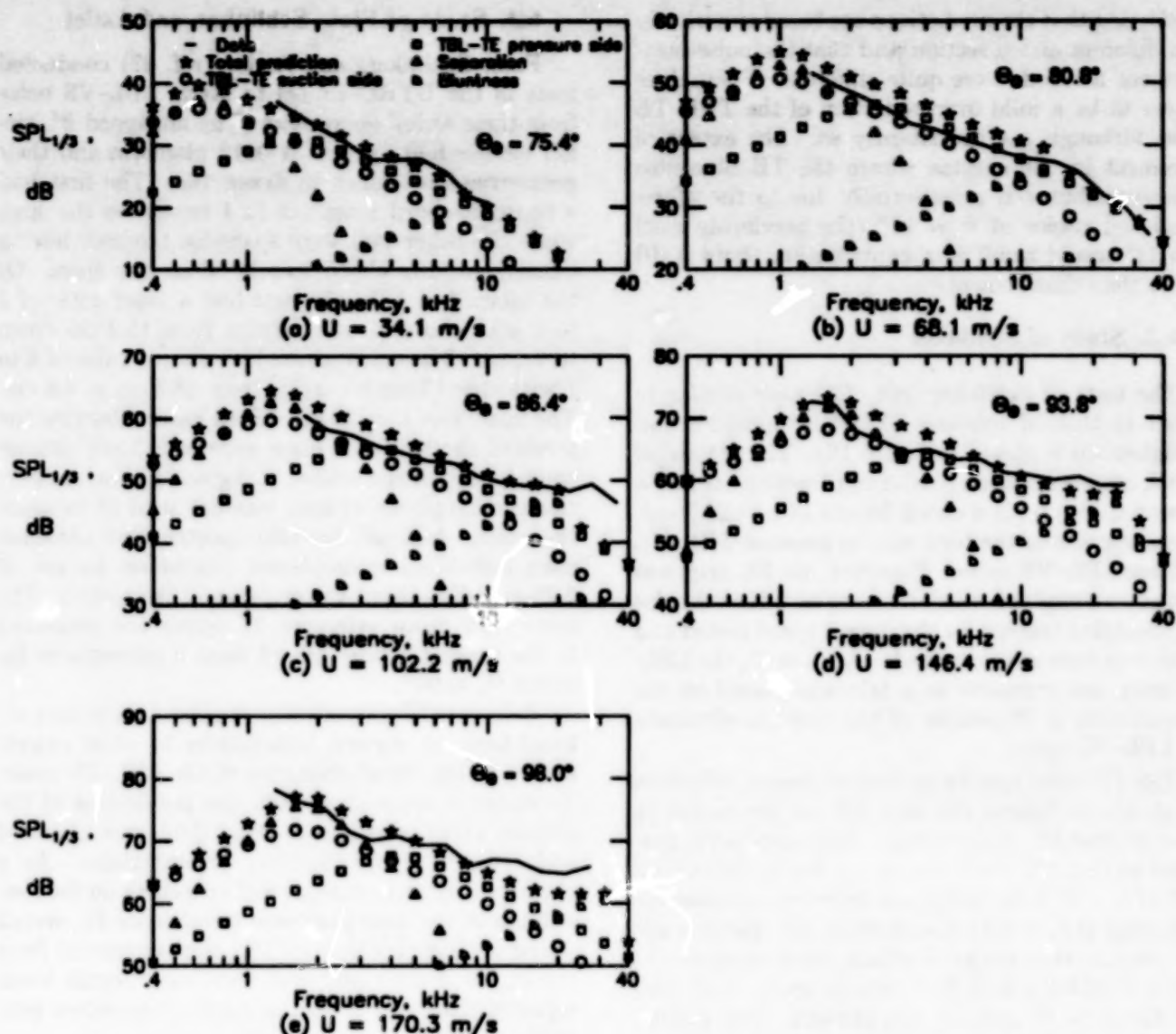


Figure 104. Noise spectra for Sikorsky airfoil at $\alpha_t = 7.6^\circ$ ($\alpha_s = 3.9^\circ$) from reference 3 compared with prediction of present paper.

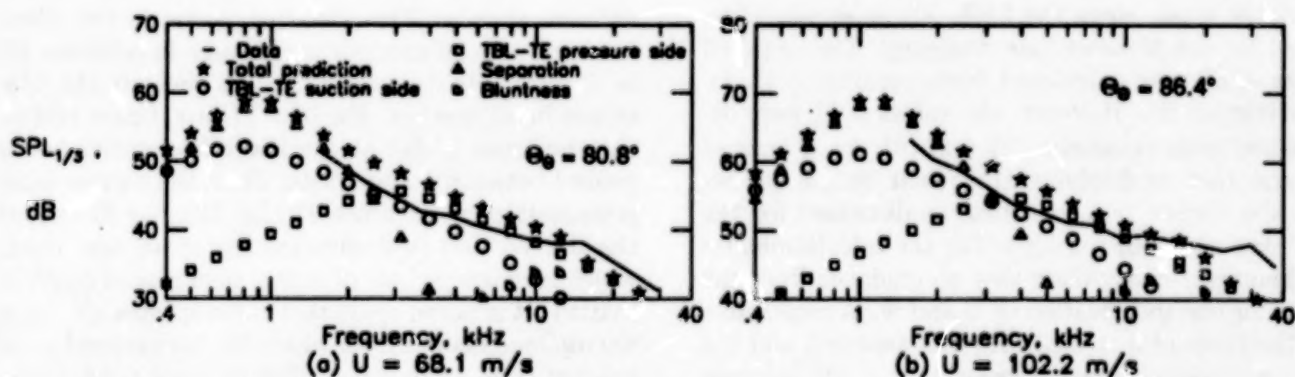


Figure 105. Noise spectra for Sikorsky airfoil at $\alpha_t = 12^\circ$ ($\alpha_s = 8.1^\circ$) from reference 3 compared with prediction of present paper.

considering that the predictions are based empirically on a different airfoil section and that the noise measurement methods were quite different. There does appear to be a mild overprediction of the TBL-TE noise, although not consistently so. The extent of agreement in the spectra where the TE bluntness noise contributes is substantially due to the aforementioned choice of $\Psi = 17^\circ$ (the previously used $\Psi = 14^\circ$ would result in a contribution about 3 dB higher than that shown).

6.2. Study of Schlinker

The tests of Schlinker (ref. 26) were similar in design to that of reference 3, whose measurement configuration is shown in figure 101. The 2D airfoil model, however, was an NACA 0012 section (as in the present study) with a chord length of $c = 22.9$ cm. Again, the aim of the tests was to measure TBL-TE and not LBL-VS noise. However, no BL trip was used at zero angle of attack because no LBL-VS noise was identified (except for the lowest speed tested and those data were not presented). At $\alpha_t = 6^\circ$, the LBL-VS noise was pervasive so a trip was placed on the pressure side at 30 percent of the chord to eliminate the LBL-VS noise.

The TE noise spectra at various tunnel velocities are shown in figures 106 and 107 for the airfoil at $\alpha_t = 0^\circ$ and 6° , respectively. The data were processed so that the levels shown are for the full airfoil span of $L = 53.3$ cm and an omnidirectional observer positioned at $r_e = 2.81$ m and $\Theta_e = 90^\circ$. For this airfoil, the corrected angles of attack, using equation (1) with $c = 22.9$ cm and $H = 79$ cm, are $\alpha_s = 0^\circ$ and 3.9° for $\alpha_t = 0^\circ$ and 6° , respectively. The predictions shown in figure 106 for zero angle of attack are for TBL-TE, LBL-VS, and TE bluntness noise. The values of δ_0 and δ_0^* used in the predictions were obtained from equations (5) and (6), for an untripped BL airfoil. The predictions shown in figure 107 for $\alpha_t = 6^\circ$ are for only TBL-TE, separation, and TE bluntness noise, since the LBL-VS noise was eliminated by the pressure side tripping. The required values of δ_s^* were calculated from equation (14), for an untripped BL. However, the values of δ_p^* were determined from equations (3) and (9), for a tripped BL and then multiplying the result by 0.6 (to reflect the "light" trip condition as discussed for the Schlinker and Amiet study). For the calculations for TE bluntness noise, there was no guidance from the paper for the specification of h and Ψ . A reasonable TE thickness of $h = 0.63$ mm was assumed and the TE flow angle parameter was set at $\Psi = 23^\circ$, because it gave good agreement for the high frequencies in figures 106 and 107. The overall agreement between the total predictions and the data appears good.

6.3. Study of Fink, Schlinker, and Amiet

Fink, Schlinker, and Amiet (ref. 27) conducted tests in the UTRC tunnel to study LBL-VS noise from three airfoil geometries. The untripped BL airfoil models had an NACA 0012 planform and their geometries are shown in figure 108. The first had a constant-chord length of 11.4 cm across the span while the other two were spanwise tapered, having linearly varying chord lengths along the span. Of the tapered airfoils, the first had a taper ratio of 2 to 1 with chord length varying from 15.2 cm down to 7.6 cm. The other airfoil had a taper ratio of 4 to 1 with chord length varying from 18.3 cm to 4.6 cm. The span was $L = 79$ cm for all cases. Because the levels of the LBL-VS noise were sufficiently intense compared with the tunnel background noise, a directional microphone system was not used to measure the noise. Instead, far-field spectra were obtained with individual microphones placed on an arc of 2.25-m radius about the midspan of the models. The noise data from reference 27 which are presented in the present report are all from a microphone for which $\Theta_e \approx 90^\circ$.

Reference 27 presented most noise data in narrow-band form at various bandwidths to allow examination of the tonal character of the LBL-VS noise. To compare these data with the predictions of the present paper, the narrow-band data were digitized and converted to 1/3-octave presentations. As a check on this procedure, as well as a check on the consistency of the data presented in reference 27, overall sound pressure levels (OASPL) were computed from the digitized data and compared with overall levels reported from direct measurement. The values generally agreed to within 1.0 dB.

For the constant-chord airfoil at $\alpha_t = 4^\circ$, 1/3-octave spectra are shown in figure 109 for various tunnel velocities between $U = 37$ m/s and 116 m/s. The number of spectral bands, as well as the frequency range, presented for the spectra varies for the different speeds. This variation is due to the different narrow-band analysis ranges used in reference 27, as all available data were used to generate the 1/3-octave band spectra. For $U = 37$ m/s, figure 109(a), the spectrum is flat at the lower frequencies but is peaked between 1 and 3 kHz. From the narrow-band presentation of reference 27 (fig. 22), one finds that the flat portion is dominated by broadband noise, which is characteristic of tunnel background contamination. It is noted again that these spectra are single microphone results from which the background noise has not been subtracted. The spectral peak region is due to the presence of three quasi-tones, representing the LBL-VS noise portion. At $U = 52, 64,$

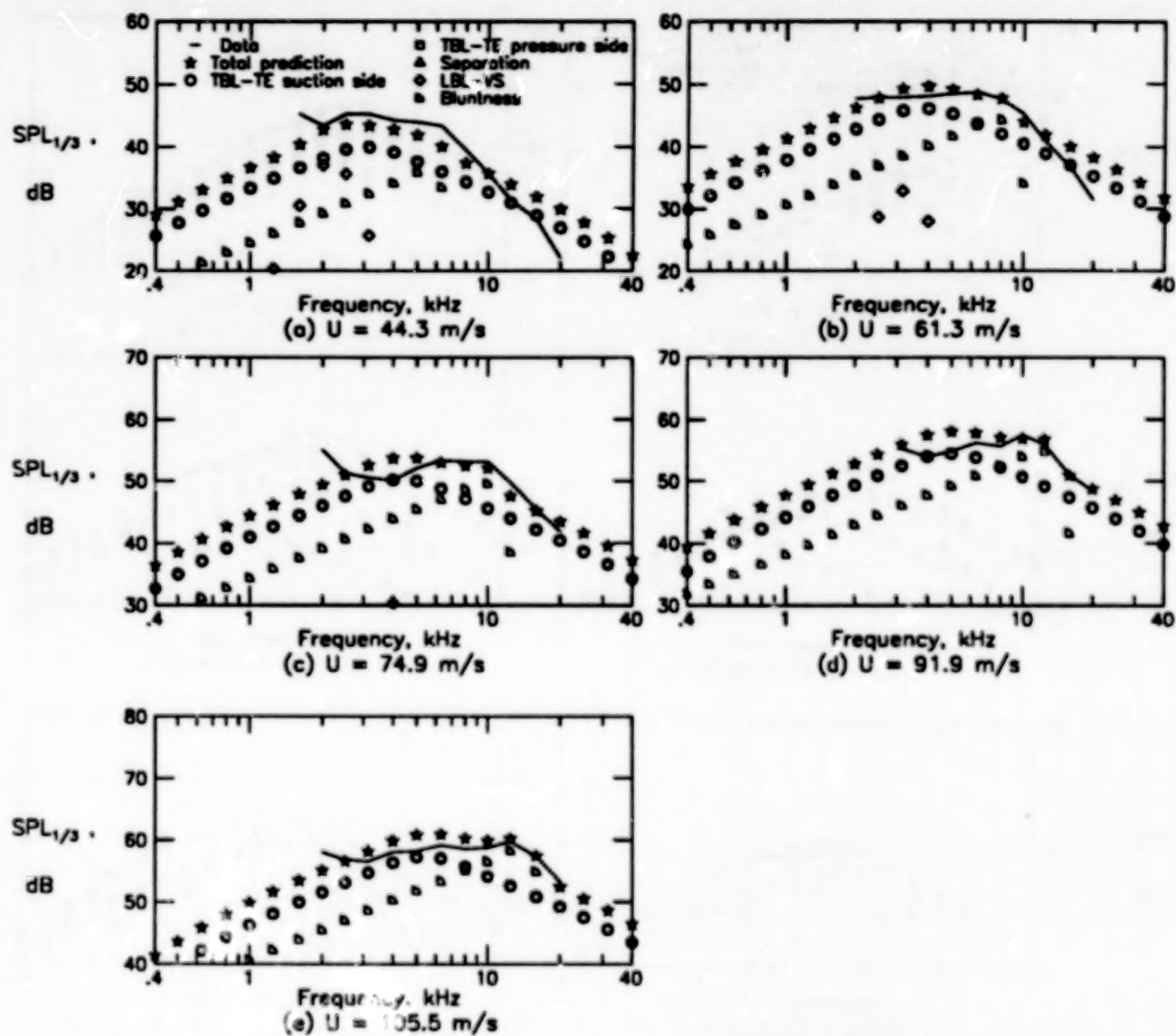


Figure 106. Noise spectra for NACA 0012 airfoil at $\alpha_t = 0^\circ$ ($\alpha_s = 0^\circ$) from reference 26 compared with prediction of present paper.

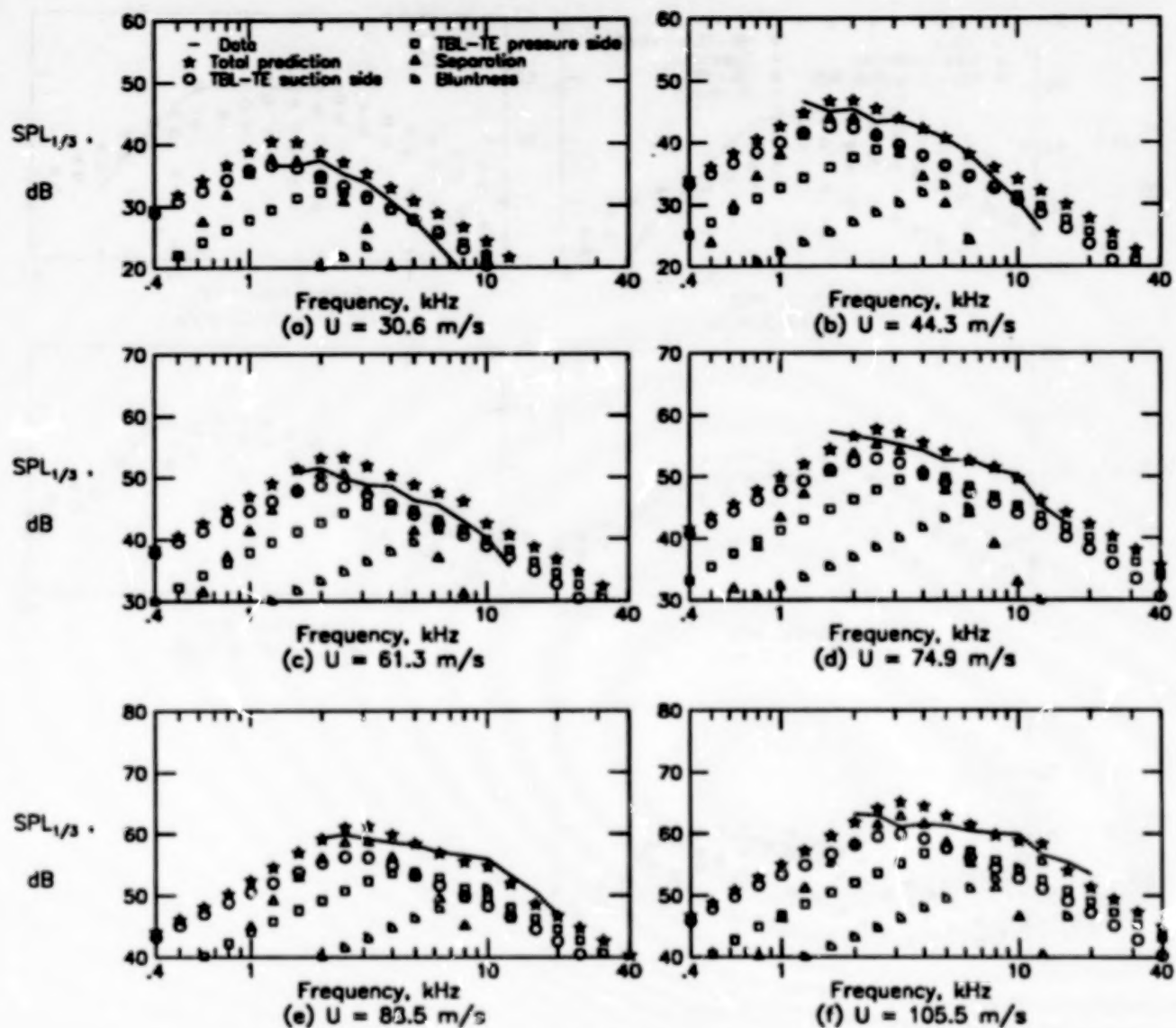


Figure 107. Noise spectra for NACA 0012 airfoil at $\alpha_t = 6^\circ$ ($\alpha_s = 3.9^\circ$) from reference 26 compared with prediction of present paper.

NACA 0012 airfoils
11.4-cm constant chord

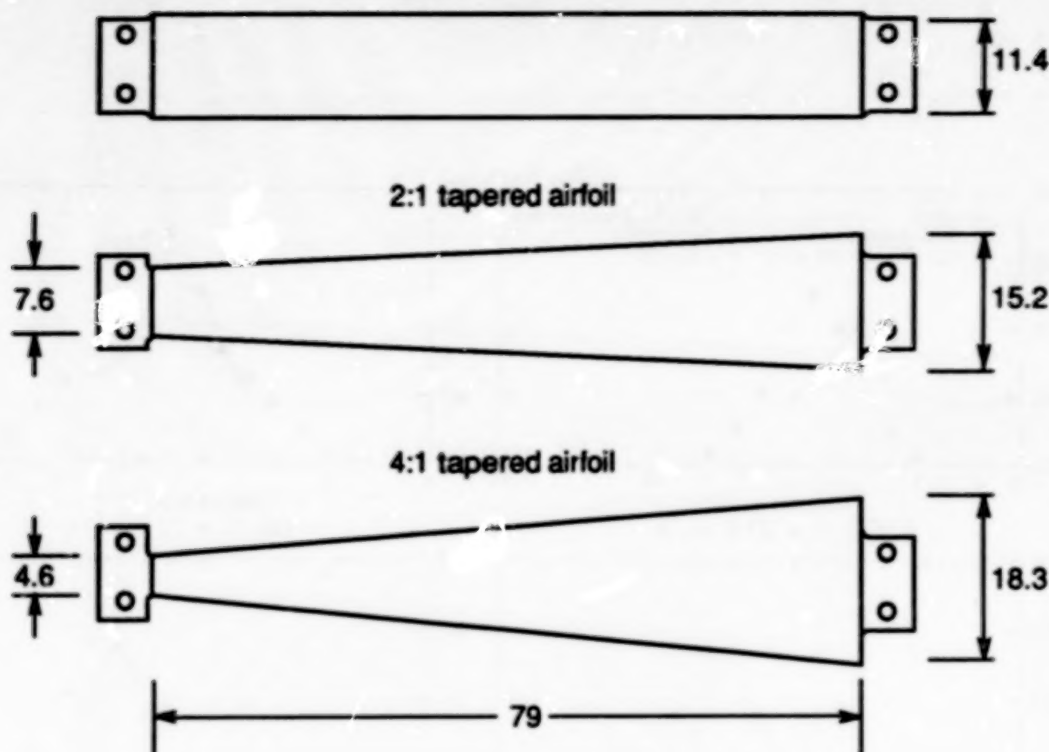


Figure 108. Airfoil models of reference 27. All dimensions are in centimeters.

and 79 m/s, in figures 109(b), 109(c), and 109(d), the spectra are very peaked because of the dominating contributions from large numbers (10 to 15) of LBL-VS quasi-tones. At $U = 98$ and 116 m/s, in figures 109(e) and 109(f), the spectra are less peaked because of a somewhat decreased number of quasi-tones which become submerged within broadband background noise (which itself increases with speed).

The strong velocity dependence of the noise is seen clearly in figure 110 (from fig. 25 of ref. 27) where the OASPL is plotted as a function of velocity. The overall levels were directly measured, for the noise between 200 Hz and 20 kHz, rather than determined by integrating measured spectra. The levels rise and then stabilize with increases in velocity. The resumed increase in levels at the highest speeds (approximately 109 m/s) is where the background noise appears to become dominant.

Compared with the data in figures 109 and 110 are noise predictions of LBL-VS, TBL-TE, and separation noise. No consideration was given to bluntness noise because of the lack of information about the TE geometry as well as the fact that LBL-VS noise dominates the predictions where comparative data are available. For the BL thickness determina-

tions, the equations of section 3 for untripped boundary layers were used. The corrected angles of attack were calculated from equation (1), with $c = 11.4$ cm and $H = 53$ cm, which rendered $\alpha_s = 0^\circ$ and 1.9° for $\alpha_t = 0^\circ$ and 4° , respectively. These were employed with the prediction equations for an observer at $r_e = 2.25$ m, $\Theta_e = 90^\circ$, and $\Phi_e = 90^\circ$. The predictions in figure 109 give good comparisons, except that the peak frequencies are lower than predicted. The previously described background noise contributions explain the differences for the lowest and highest speeds. For the predictions of OASPL in figure 110, the spectra for LBL-VS, TBL-TE, and separation noise were summed. Predictions are presented for not only $\alpha_t = 4^\circ$ but also $\alpha_t = 0^\circ$, 2° , and 6° . This is done to show the great sensitivity of the predictions to airfoil angle of attack. It is seen that the data would most agree with predictions for about $\alpha_t \approx 5^\circ$ rather than $\alpha_t = 4^\circ$. This could be interpreted to mean that the agreement is on the order of possible experimental bias error in angle definition.

The tapered-chord airfoils were used in reference 27 to provide a continuous variation in expected vortex tone frequency to compare with an analogous rotating constant-chord blade. The tone variation